Alloys-by-Design: Application to Polycrystalline Nickel Superalloys for High Pressure Turbine Discs



David Crudden

St Anne's College

University of Oxford

A thesis submitted for the degree of

Doctor of Philosophy

Trinity Term 2014

Alloys By Design: Application to Polycrystalline Nickel Superalloys for High Pressure Turbine Discs

David Crudden, St Anne's College

Submitted for the degree of Doctor of Philosophy, Trinity Term 2014

Abstract

The nickel-based superalloys have been a key enabler to the development of modern gas turbine engines. Since their introduction the chemical complexity of these alloys has increased significantly, with current generation nickel-based superalloys usually containing over 10 different elements. It is this combination of alloying additions that is responsible for the superior high temperature properties these alloys exhibit. Traditionally, alloy design has invoked considerable use of trial-and-error based approaches involving costly and exhaustive processing backed up by empirical property testing. In this work a computational materials design approach is developed. This method links physically-faithful composition-dependent models with thermodynamic calculations to understand material behaviour. By doing this it is possible to consider large compositional design spaces and isolate alloys expected to have optimal performance for specific applications. The scope of this research has been to apply the computational model to the design of a polycrystalline nickel-based superalloy for turbine disc applications in next generation jet engines. The design trade-offs encountered when developing the new alloy are highlighted. Alloy compositions which are predicted to be optimal for turbine disc applications are isolated. These alloys have been manufactured using a scaled down version of the commercial production method. The newly manufactured alloys have been characterised using microstructural evaluation, mechanical testing and corrosion testing. The experimental results have been compared with modelling predictions in order to determine the capability of the computational approach.

Preface

Research in this thesis has been published as follows:

- D.J. Crudden, B. Raeisinia, N. Warnken, R.C. Reed. Analysis of the chemistry of nickel based turbine disk superalloys using an alloys-by-design modelling approach. *Metallurgical and Materials Transactions A*, 44:24182430, 2013.
- D.J. Crudden, N. Warnken, A. Mottura, R.C. Reed. Modelling of the influence of alloy composition on flow stress in high strength nickel based superalloys. *Acta Materialia*, 75:356–370, 2014.
- D.J. Crudden, B. Raeisinia, M.C. Hardy, and R.C. Reed. A nickel based alloy composition. *Patent application number GB 1400352.9, 2014.*

Acknowledgements

I would like to thank my supervisor Professor Roger Reed for his support, advice and patience. He has been an excellent mentor and friend throughout the extent of my research, I will be eternally grateful for everything has taught me. I am also extremely grateful to my industrial supervisor Dr Mark Hardy of Rolls-Royce plc. His knowledge and advice have been essential in making this work possible. I would also like to acknowledge the generous financial support provided by Rolls-Royce plc. and the Engineering and Physical Sciences Research Council (EPSRC).

I would like to thank the many collaborators and friends I have gained during the course of my doctoral degree. Dr Babak Raeisinia provided me with academic guidance throughout my research and helped keep my spirits up during the toughest times, Dr Alessandro Mottura for conducting DFT simulations, Dr. Nils Warnken for contributions to the CALPHAD modelling, Dr John-Christophe Gebelin for his excellent technical support necessary for much of the computer simulations used in this work, Dr Matthew Lunt for his help with electron microscopy, Dr Paul Bagot and Professor Michael Moody for conducting atom probe tomography experiments, Dr Atsushi Sato for his advice and guidance on oxidation experiments. I would also like to thank the excellent technical staff at the University of Oxford.

I would like to extend my gratitude to my friends, Enrique Alabort, Paraskevas Kontis, Yilun Gong and Zailing Zhu who are part of with Professor Reed's research group. Their friendship and support has been of great importance to me.

I would like to thank my parents Gerard and Ethna Crudden and brothers Philip, Gerard and Anthony Crudden who have inspired me to work hard and supported me in everything I have done.

Most importantly, I would like to give my sincerest thanks to my wife Clare, she has supported me – and suffered with me – during the most trying times. Without her love this work would not have been possible.

Contents

List of Figures **x**

List of Tables **xvi**

1 Introduction **1**

1.1 The Development of Structural Alloys 1

1.2 Gas Turbine Engines 3

1.2.1 Material Requirements for Turbine Discs 5

1.3 Structure of Thesis 7

2 Literature Review **9**

2.1 The Physical Metallurgy of Nickel-Based Superalloys 9

2.1.1 The γ phase 11

2.1.2 The γ' Phase 12

2.1.3 Grain Boundary Phases 14

2.1.4 TCP Phases 15

2.2 Processing Superalloys for Turbine Disc Applications 15

2.2.1 Heat Treatment 18

2.2.1.1 Solution Heat Treatment 19

2.2.1.2 Aging Heat Treatment 20

2.3 The Mechanical Properties of Turbine Disc Alloys 20

2.3.1 Tensile Strength 21

2.3.1.1 Strengthening from the γ matrix 21

2.3.1.2 Precipitation Strengthening 22

2.3.2 Creep Resistance in Turbine Disc Alloys 24

2.4 Developing Oxidation Resistance in Nickel-Based Superalloys 25

2.4.1 The Thermodynamic Basis for Imparting Oxidation Resistance . 25
2.4.2 Oxidation of Ni-Cr and Ni-Cr-Al 27
2.4.3 The Oxidation Characteristics of High-Strength Polycrystalline Superalloys 32

3 Designing a Turbine Disc Chemistry Using the Alloys By Design Approach 37
3.1 Introduction 37
3.2 Modelling Methodology 41
3.2.1 Estimation of Phase Equilibria 41
3.2.2 Estimation of Yield Strength 43
3.2.3 Estimation of Oxidation Resistance 46
3.2.4 Estimation of Creep Resistance 47
3.2.5 Estimation of Density 48
3.3 Results 48
3.4 Discussion 52
3.4.1 Mechanical Behaviour Considerations in Design of Alloys 53
3.4.2 Lifing Considerations in Design of Alloys 58
3.4.3 Example: Management and Optimisation of Alloy Chemistries . 61
3.5 Summary and Conclusions 63

4 Modelling of the flow stress of Nickel-Based Supealloys 66
4.1 Introduction 66
4.2 Background 68
4.3 Modelling Approach 76
4.3.1 Calculation of the APB energy using the CALPHAD Approach . 77
4.3.2 DFT approach 82
4.3.3 Modelling the Yield Strength for Alloy Design Purposes 83
4.4 Results 83
4.4.1 Comparing the Enthalpy of Mixing from CALPHAD and DFT Calculations 84
4.4.2 APB Energies in Ni-Al-X Alloys 87
4.4.3 Application of CALPHAD method to multi-component alloys . . 90
4.5 Discussion 92

4.5.1 Comparison of CALPHAD and DFT Calculation for APB Energies 93
4.5.2 Improving APB modelling using DFT calculations 94
4.5.3 Relevance to alloy design 96
4.6 Conclusions 100

5 Experimental Characterisation of Newly Designed Turbine Disc Alloys 102
5.1 Introduction 102
5.2 Optimising Alloy Chemistry 103
5.3 Experimental Procedures 106
5.3.1 Material Preparation 106
5.3.2 Microstructural Analysis 109
5.3.3 Atom Probe Tomography 110
5.3.4 Oxidation Testing 110
5.3.5 Mechanical Testing 112
5.4 Results 113
5.4.1 Microstructural Analysis 113
5.4.2 Mechanical Properties 121
5.4.3 Oxidation Resistance 123
5.5 Discussion 128
5.5.1 Mechanical Properties 128
5.5.2 Oxidation Resistance 130
5.5.3 Considering the design for future alloys 131
5.6 Conclusions 133

6 Conclusions and Future Work 135
6.1 Conclusions 135
6.2 Future Work 138
6.2.1 Strength Optimisation and Modelling 138
6.2.2 Grain Boundary Engineering 140
6.2.3 Oxidation Modelling 141
6.2.4 Dwell Fatigue 143
6.2.5 Increasing the Scope of the Alloys-by-Design software 143

Bibliography **145**

7 Appendix **164**

7.1 Appendix A - Patent for ABD Alloys 165

List of Figures

1.1 Time-line illustrating the development of structural alloys for a number of metallic systems. 2
1.2 A cross sectional view of jet engine illustrating the areas in which different structural alloys are used (image courtesy of Rolls-Royce), the temperature at different points in the engine is included. 4
1.3 Performance diagram illustrating the how the specific fuel consumption (defined as normalised fuel burn/thrust developed) against thrust, for various values of TET and OPR 5
1.4 Typical stress and temperature distribution in a turbine disc component (image courtesy of Rolls-Royce). 6

2.1 Categories of elements important to the constitution of nickel-based superalloys along with their relative positions on the periodic table. 11
2.2 The crystal structure of the γ' phase. 13
2.3 An illustration of the powder metallurgy process used in the production of turbine disc components 17
2.4 An overview of the precipitate strengthening mechanisms occurring in nickel-based superalloys. 23
2.5 The Ellingham diagram, showing the standard free energy of formation for a selection of oxides. 27
2.6 Composition dependance for parabolic rate constant for the oxidation of Ni-Cr alloys between 800°C and 1200°C. 28
2.7 An illustration of the transient oxidation and steady state oxidation for, (a) Cr rich alloy e.g. Ni-(20-40)Cr, (b) Cr lean alloys e.g. Ni-5Cr. 29

2.8 Diagram showing the compositional limits for three different oxidation mechanisms occurring in Ni-Cr-Al alloys in 0.1 atm of oxygen at 1000°C. There are three distinct regions *(I)* an external scale of NiO is formed, sub-scale chromium and/or aluminium oxides are formed, *(II)* an external scale of Cr_2O_3 is formed with sub-scale Al_2O_3, *(III)* only an external scale of Al_2O_3 is formed. Solid data-points correspond to areas where only one mechanism was observed, open data-points correspond to areas where both mechanisms were observed. The red data-points show the position of a number of different turbine disc alloy compositions. 30

2.9 Microstructure of an oxide representative of, (a) group I alloy, (b) group II alloy, (c) group III alloy. 31

2.10 Typical cross section for a turbine disc alloy after oxidation damage. Example shows RR1000 after exposure in air at 800°C for 2000h. 33

2.11 Mass gain after 20 hours of oxidation in air for Ni-20Cr alloys containing varied amounts of Ti. 34

2.12 Mean diffusion distance for Al ions in Al_2O_3, Ti ions in TiO_2 and Cr ions in Cr_2O_3 as a function of time. The diffusion co-efficient of these ions at 800°C, shown in the parentheses in the figure, were evaluated by extrapolation of the Arrhenius relationship of diffusion coefficients measure at high temperatures. 36

3.1 Timeline of the chemistry of select patented nickel-based disc alloys binned into 5-year classes. The points represent the mean of the concentrations of the alloying elements in each class and the whiskers point to the maximum and minimum of the concentrations deduced from the patents. The so-called 'preferred' compositions are noted for each element. The numbers listed in parentheses on the Nb plot are the number of patents examined for each case. For example, 19 disc alloy patents were examined which were published between the years 1985 and 1990. . 39

3.2 Comparison of the calculated and measured γ' solvus temperatures for a number of different nickel-based superalloys, select commercial alloys are delineated. 43

3.3 Performance of the neural network compared with data contained in the (a) training set and (b) testing set. 46
3.4 Limits of the composition design space used in the present study (Table 3.3). The extent of the patented compositional space for nickel-based disc alloys (Figure 3.1) is also delineated. 49
3.5 Predicted (a) yield strength and (b) creep merit index as a function of γ' volume fraction at 650 °C. 50
3.6 Predicted (a) density and (b) γ' solvus temperature as a function of γ' volume fraction at 650 °C. 51
3.7 Predicted σ volume fraction as a function of (a) γ' volume fraction and (b) chromium activity at 650 °C. 52
3.8 Contour plots showing the effect of different alloying elements and γ' volume fraction on (a) yield strength in MPa, (b) density in g/cm^3, (c) creep merit index in m^{-2}s $\times 10^{-19}$, and (d) activity of chromium. 54
3.9 Oxidation data for Ni-Cr binary alloys at 900 °C in 0.1atm of O_2 59
3.10 Contour plots showing the variation of σ volume fraction with (a)nickel content and γ' volume fraction and (b) molybdenum, tungsten, and chromium content of the alloy. 61
3.11 A case study showing how the Alloys-by-Design method can be used to optimise alloy properties at a given volume fraction of γ'. 62

4.1 Illustration showing the formation of an APB on the {111} plane, in the γ' phase. 69
4.2 The APB energies on the {111} plane for $L1_2$ alloys plotted against the disorder-order transition temperature. Full circles represent TEM measurement and open circles represent atomistic calculations. The straight lines are APB energies determined from the nearest neighbour interaction with ordering energies derived from T_c using $w = 0.82$ and $w = 1.5$. 70
4.3 Review of literature values for variation of APB energy in binary Ni_3Al with Al content: full circles Cockayne corrected values, open circles image simulations. 72
4.4 Computer estimates of APB energies in $Ni_3(Al, X)$ using DFT methods, Chandran and Sondhi, Vasmi and Karthikenyan. 76

4.5 Flow chart outline the process for modelling the APB energy in Ni-based superalloys. 80
4.6 A comparison of enthalpy of mixing calculated using CALPHAD and DFT for the $L1_2$ phase when (a) Ti, (b) Ta, (c) Nb, (d) W, (e) Mo and (f) Cr are substituted for Al atoms. Changes in energy have been normalised to the value for Ni_3Al to allow for comparison between methods. 85
4.7 A comparison of enthalpy of mixing calculated using CALPHAD and DFT for the f.c.c. phase when (a) Ti, (b) Ta, (c) Nb, (d) W, (e) Mo and (f) Cr are substituted for Al atoms. Changes in energy have been normalised to the value for Ni_3Al to allow for comparison between methods. 86
4.8 The change in APB energy on the {111} plane when (a) Ti, (b) Ta, (c) Nb, (d) W, (e) Mo and (f) Cr are substituted for Al in the γ' phase. . . 89
4.9 A comparison of measured yield strength values with calculated precipitate strengthening using the APB energy determined with the CALPHAD approach. 90
4.10 A contour plot showing how γ' volume fraction and APB energy affect precipitate strength. Clusters delineating specific levels of titanium in the alloy have been plotted. 92
4.11 A comparison of measured yield strength values with calculated precipitate strengthening using the APB energy determined with the DFT approach. 96
4.12 Contour plots showing the precipitate strengthening for the alloy design space calculated using APB energy determined from DFT calculations: (a) effect of γ' volume fraction and APB energy effect precipitate strength, clusters delineating specific levels of AL in the alloy have been plotted, (b) composition-property map showing the effect of Al content and (Ti+Ta+Nb)/Al ratio on precipitate strengthening. 98
4.13 A composition-property map showing the effect of Al content and (Ti+Ta+Nb)/Al ratio on γ' solvus temperature. 99
4.14 Alloys have been grouped based on their Ti/Al (at%) ratio. The fraction of η in the alloys has been displayed as a distribution. Open circles represent the median value for each distribution. 100

5.1 Final forgings of alloys ABD D1-D3 measuring approximately 110mm in diameter. 107
5.2 Measurement of γ' solvus temperature for alloys D1 - D3 using DSC. . . 108
5.3 Heat treatment process applied to alloys ABD D1-D3. 109
5.4 Geometry of RLH10259 test specimen used for tensile and creep testing. 112
5.5 The microstructure of alloy D3 after aging heat treatment, observed using optical microscopy. 113
5.6 SEM secondary electron images showing the γ' morphology after heat treatment for alloy, (a) D1, (b) D2, (c) D3. 115
5.7 Precipitate size distribution for secondary γ' determined for alloys D1-D3 using ImageJ analysis. 116
5.8 Reconstruction of atom probe data for alloy D2. 119
5.9 Plots of $C^n - C^\gamma$ vs. $C^{\gamma'} - C^\gamma$, constructed using the phase compositions measured using APT for alloy (a) D1, (b) D2, (c) D3. 120
5.10 The temperature dependent yield strength for alloys D1-D3 determined, (a) experimentally, (b) using neural network predictions. 122
5.11 Larson-Miller plot for alloys D1-D3, RR1000 is included for comparison. 123
5.12 Oxidation rate for newly developed turbine disc alloys after 100 hours exposure in air at 800°C. A comparison is made with RR1000. 124
5.13 The parabolic oxidation rate for alloys D1-D3 and a number of commercial turbine disc alloys compare with, (a) calculated activity of chromium in the alloy, (b) chromium content in at%. 125
5.14 Backscattered electron images showing the oxidation damage after 100 hours of exposure in air at 800°C for alloy (a) D1, (b) D2, (c) D3. . . . 126
5.15 EPMA maps showing the distribution of alloying elements after 100 hours of exposure in air at 800°C for alloy (a) D1, (b) D2, (c) D3. . . . 127
5.16 The parabolic oxidation rate for alloys D1-D3 and a number of commercial turbine disc alloys compared with, (a) titanium content in at.%, (b) Cr/Ti ratio in at.% 131
5.17 Yield Strength for RR1000 and alloys D1-D3 calculated using the DFT model described in chapter 4. Calculations conducted at 650 °C, contours for yield strength have been normalised to the modelled yield strength of RR1000. 132

6.1 Contours for predicted yield strength (MPa) as a function of γ' volume fraction and APB energy. Red points indicate the calculated strength of alloys developed using the ABD method. Modelling predictions for a number of commercially available turbine disc materials are also included for reference. 139
6.2 Yield strength as a function of temperature for the alloys D1-D6. The results are compared with the design requirement shown in red. 140
6.3 Correlation observed between Cr/Ti ratio and oxidation resistance for a number of turbine disc alloys. Oxidation studies were conducted at 800°C in air for 100 hours. The ABD alloys are highlighted in red. . . . 142

List of Tables

2.1 Typical compositions of turbine disc alloys in wt.%. 10

3.1 Range of input and output values included in the neural network database (compositional ranges are in wt%). The minima are zero unless otherwise stated 45
3.2 Various constants used in this work. 48
3.3 Limits of the composition design space used in the present study 49
3.4 Range of alloy properties predicted at approximately 50% volume fraction of γ' 63

4.1 APB energies measured using weak beam TEM methods (in mJ/m^2). TEM measurements have been corrected using: Cockayne correction methods (c), Image simulations (s). 73
4.2 A summary of APB energies calculated for Ni_3Al (in mJ/m^2). 74
4.3 First principle calculations for interchange energies considering up to 4th nearest neighbour interactions, given in k (1.38×10^{-23} JK^{-1}) units. . . 78
4.4 The ordering energy calculated using the TTNi7 database compared with: ab-initio calculations, experimentally measured values. 81
4.5 Limits of the composition design space used in the present study. 91
4.6 Coefficients for APB energy change determined from DFT work. 95

5.1 Chemistries (wt.%) for RR1000 and the new polycrystalline alloys designed using the ABD method. 104
5.2 Modelling predictions for the properties of RR1000 and newly designed alloys. Calculations conducted at 650°C. 106

5.3 Chemistry (at.%) of polycrystalline alloys studied in oxidation experiment. The levels of minor alloying elements C, B and Zr have not been included. 111
5.4 Conditions used for tensile and creep testing. 112
5.5 Measured volume fraction of γ' compared with CALPHAD predictions. 114
5.6 Phase compositions and partitioning coefficients determined using CALPHAD compared with APT measurements. 118
5.7 Creep rupture life in hours for alloys D1-D3 for a number of creep conditions. 123

6.1 The composition in wt.% of alloys developed using the ABD software, RR1000 is included for reference. 138

1

Introduction

1.1 The Development of Structural Alloys

Metallic alloys – often used to produce structural components – are suitable for engineering applications because of their ability to withstand significant mechanical and thermal loads. The development of structural alloys has been driven by the emergence of new technologies. For example, the development of aluminium alloys was driven by the introduction of aircraft. The properties of the alloys used – e.g. tensile strength, density or corrosion resistance – may often be the limiting factor in the overall performance of an engineered device. This is particularly true in areas such as transportation or energy production, where the requirement to maximise efficiency and reduce harmful emissions is of global significance. The introduction of new alloys can play an important role in the development of cleaner more efficient transport or energy technology. However, historically the approaches used for the discovery of improved metallic alloys have been slow and costly.

Figure 1.1 provides an overview of the development time-line for the main classes of

structural alloys. What is striking is that much of the material commonly used today was developed almost 100 years ago. For example, Ti-6-4 or Inconel 718 are still extensively used in gas turbine engines. Much of the advancement in these alloys preceded our understanding of the physics responsible for their behaviour. The development of such alloys has been reliant on trial-and-error based approaches backed up by empirical property testing. However, given the chemical complexity of many structural alloys – sometimes containing up to 10 different alloying elements – it is improbable that optimal compositions could be discovered using such empirically-based design.

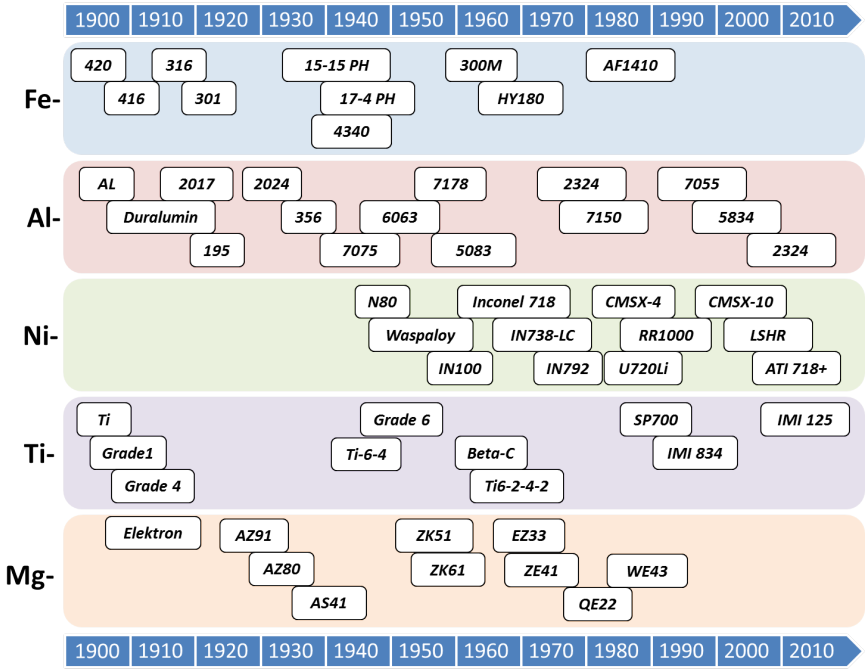


Figure 1.1: Time-line illustrating the development of structural alloys for a number of metallic systems.

Our understanding of the mechanisms which determine the performance of metallic alloys has progressed over the past century. This knowledge has led to the formulation of models – across a variety of length scales – that can accurately predict how a material will behave. Furthermore, the development of low cost, high powered computational

facilities has made it economical to conduct high volumes of complex calculations. In this thesis a computational modelling approach that uses composition-property relationships to optimise alloy chemistry is presented. Computer-based modelling and analysis tools can allow us to explore all possibilities, facilitating expedited identification of alloys designed for improved performance. This method, christened 'Alloys-by-Design' (ABD) by Reed et al. [1], represents a complete paradigm shift in comparison to traditional empirical alloy development. The approach has been developed with the motivation to accelerate alloy development at a significantly reduced cost. Previously, Reed et al. [1] focused on the optimisation of a single crystal nickel-based superalloys for turbine blade applications. Instead, in this research the model has been developed for the design of a polycrystalline nickel-based superalloy for turbine disc applications.

As this research is focused on the development of alloys for gas turbine engines a brief overview of the operation is given. This is reviewed to develop the rationale for the design specification of a new turbine disc alloy.

1.2 Gas Turbine Engines

An illustration of the typical architecture for a gas turbine engine is presented in Figure 1.2. More specifically, this is the arrangement for a turbofan jet engine used for civil aircraft applications. The engine is comprised of four main sections: fan, compressor, combustor and turbine. The fan is used to draw air into the engine, much of this air by-passes the engine to produce thrust. Some of the air drawn in by the fan is passed to the core of the engine where it is compressed. This pressurised air is mixed with fuel in the combustor and ignited in order to produce a hot, highly pressured gas stream. The turbine system extracts energy from the gas stream to produce mechanical work which drives the fan and compressor. The hot gas is discharged from the engine after

the turbine stage also providing additional thrust.

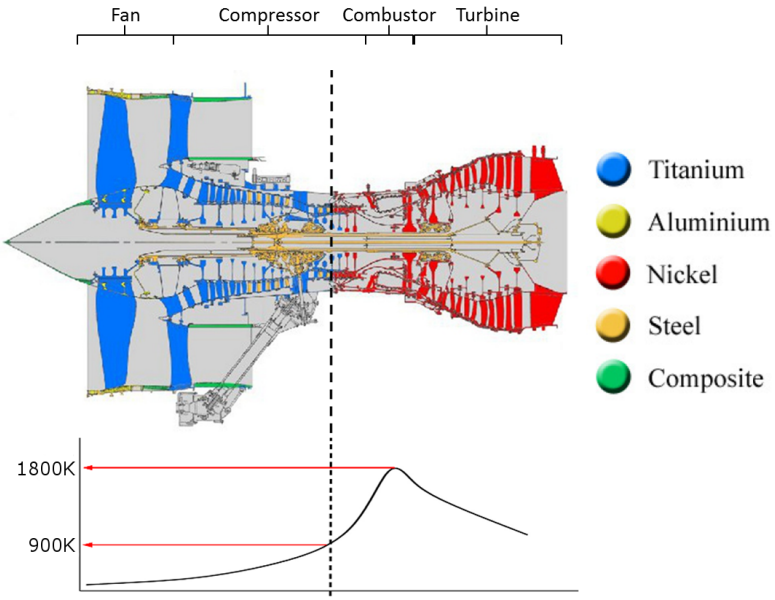


Figure 1.2: A cross sectional view of jet engine illustrating the areas in which different structural alloys are used (image courtesy of Rolls-Royce), the temperature at different points in the engine is included.

For a gas turbine engine to perform efficiently combustion must occur at significantly high temperatures, sometimes in excess of 1800K. Figure 1.2 shows how temperature varies with respect to position in the engine; the materials used for different components are also indicated. At the front end of the engine – where temperatures are below 900K – titanium alloys are used extensively. These alloys have a high specific strength making them attractive as they help reduce the weight of the engine. However, as the engine temperature continues to increase the strength and corrosion resistance of the titanium alloys becomes insufficient. For high temperature applications – in the region above 900K – components are predominantly manufactured from nickel-based superalloys. The introduction of nickel-based superalloys as a high temperature material has been critical to the success of gas turbine technology.

The development of next generation gas turbine engines is focused on improving ef-

ficiency, reducing the emission of harmful gases, increasing reliability and extended service life. Figure 1.3 [2] shows that engine efficiency – in this case measure by specific fuel consumption – is improved by increasing the overall pressure ratio (OPR) and and turbine entry temperature (TET). Given the strong effect of TET this is often increased for newly developed engines, since the introduction of gas turbine engine the TET has risen by approximately 700K [2]. The result of increased TET is that components within the turbine section must withstand higher operating temperatures. The maximum operating temperature of materials used to construct the turbine is a limitation to TET, therefore, the overall efficiency of the engine. Hence, the search for structural materials with increased temperature capabilities is of great significance to engine manufacturers.

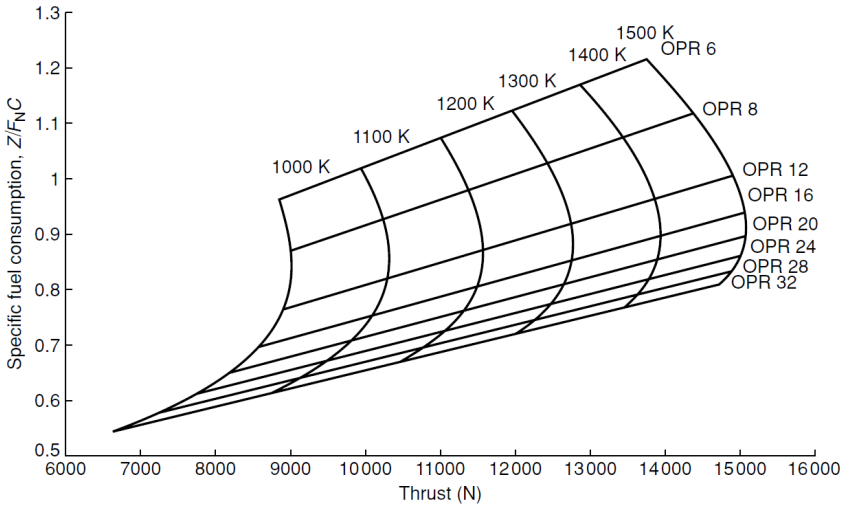


Figure 1.3: Performance diagram illustrating the how the specific fuel consumption (defined as normalised fuel burn/thrust developed) against thrust, for various values of TET and OPR [2].

1.2.1 Material Requirements for Turbine Discs

The turbine disc rotates at several thousand revolutions per minute. This high rotational speed combined with the significant mass of the component results in the gen-

eration of large centripetal stresses. In combination with the centripetal stress there is also a wide distribution in temperature across the component. Figure 1.4 shows the stress and temperature distribution for a turbine disc component. Typically, the stress and temperature ranges between 500 - 1200 MPa and 300 – 800°C, respectively.

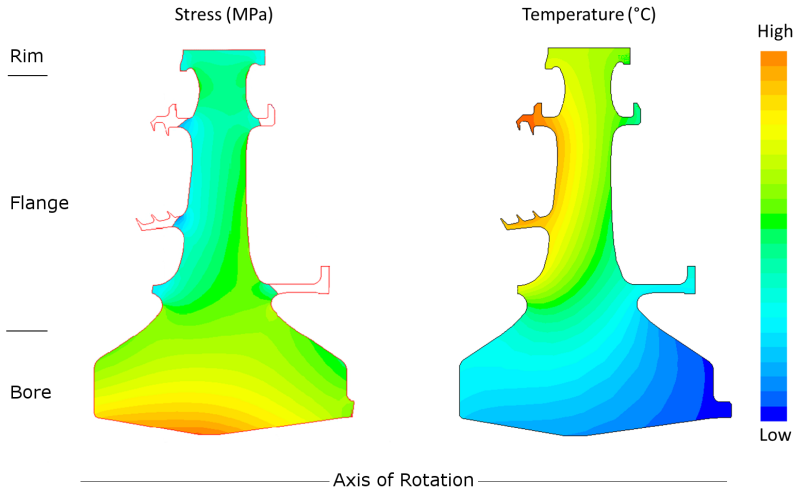


Figure 1.4: Typical stress and temperature distribution in a turbine disc component (image courtesy of Rolls-Royce).

There are three distinct sections on the disc – the bore, flange and rim – these are identified in Figure 1.4. At the bore of the disc there are high stresses at relatively low temperatures. In this area high tensile strength is essential so that the disc is resistant to burst which would result in a catastrophic failure of the engine. The bore region must also be resistant to crack propagation under low and high cycle fatigue conditions. Conversely, the stresses at the rim are much lower but the temperature is much greater. At these high temperatures and intermediate loads it is important that the material is resistance to dwell fatigue cycles and creep deformation. Oxidation and hot corrosion damage is also becoming a life limiting factor at the rim as the TET continues to increase.

As the entire disc must be produced from the same material, a significant materials

engineering challenge exists. For a structural material to be considered for turbine disc applications good tensile strength is essential; this must be combined with resistance to creep, fatigue and corrosion damage. The material must also be amenable to conventional manufacturing techniques, i.e. forging and machining operations.

1.3 Structure of Thesis

Chapter 2 begins with an overview of the physical metallurgy of the nickel-based superalloys. The rationale for the extensive range of alloying additions is considered. The processes required to manufacture a turbine disc are outlined. The strengthening and corrosion mechanisms for nickel-based superalloys are reviewed in detail, as understanding the composition dependence of these properties has been the main focus of this research work.

In Chapter 3 a critique of the composition of nickel-base superalloys used for turbine discs is made using the ABD [1] model. A large number of alloy chemistries within the Ni-Cr-Co-Al-Ti-Mo-W-Ta(-Zr-C-B) compositional design space are evaluated using the computational approach. The examined compositions are assessed based on their yield strength, creep behaviour, resistance to oxidation, susceptibility to formation of σ phase, γ' volume fraction, γ' solvus temperature, and density. Trade-off diagrams are developed for the different alloy properties to highlight the limitations and challenges encountered when designing new nickel-based alloys for turbine disc application. The results of this analysis are used to construct composition-property maps that allow for an informed, rather than inspired, approach when designing nickel-based superalloys.

In Chapter 4 a physics based model is proposed for the variation of the yield strength of nickel-based superalloys as a function of chemical composition. Consistent with hardening theory, alloy strength is assumed to be proportional to the product of the

anti-phase boundary (APB) energy and the square root of the fraction of the strengthening γ' phase. A relationship is established between the APB energy estimated using a CALPHAD database and predictions from density functional theory (DFT). Quantitative estimates for the role played by Ti, Ta, Nb, Cr, W and Mo suggest that these have a profound effect on the APB energy. A procedure is proposed to enable the strength to be estimated from an initial input of the chemical composition alone. Predictions are made for new multi-component alloys. Insight is provided into how compositions may be isolated to optimise the strength of polycrystalline nickel-based superalloys.

In Chapter 5 prototype alloys isolated using the ABD approach are studied using a series of experimental tests. Focus is placed on microstructural evaluation, tensile testing, creep deformation behaviour and oxidation resistance. The experimental results are compared with predictions made using the ABD approach. By comparing the outcome of experimental tests with modelling predictions, it is possible to understand the accuracy of the sub-models contained within the ABD model. Conclusions are drawn on how the ABD model can be improved. Suggestions are also made on how the chemistry of the new turbine disc alloy can be modified to improve the properties of the material.

Finally, in Chapter 6 the key outcomes from this research are outline. Suggestions for the future work necessary for the continued improvement of ABD model are presented.

2

Literature Review

2.1 The Physical Metallurgy of Nickel-Based Superalloys

For nickel-based superalloys the relationship between composition and microstructure plays a critical role in determining their behaviour [3]. Table 2.1 lists the compositions for a number of polycrystalline nickel-based superalloys used for turbine disc applications. Throughout their development the improvements in high temperature properties of these alloys can be attributed to increasing chemical complexity and levels of alloying, with current alloys comprised from ten or more elements. If a comparison is made between an early and current generation turbine disc alloy, for example comparing Nimonic90A (∼1945) [4] and LSHR (∼2002) [5], it is clear that the number of elements and levels of alloying has doubled.

Table 2.1: Typical compositions of turbine disc alloys in wt.%.

	Cr	Co	Mo	W	Ta	Nb	Al	Ti	Fe	Hf	C	B	Zr
Astroloy	15	17	5.3	-	-	-	4	3.5	-	-	0.06	0.03	-
EP741NP	8.2	15.8	3.9	5.3	-	2.56	5.02	1.45	-	0.24	0.04	0.015	0.01
IN100	12.3	18.3	3.30	-	-	-	4.9	4.30	0.1	-	0.06	0.02	0.02.00
Inconel 706	16	-	-	-	-	2.9	0.2	1.8	40	-	0.03	-	-
Inconel 718	19	-	3	-	-	5.1	0.5	0.9	18.5	-	0.04	-	-
LSHR	13	21	2.7	4.3	1.6	1.5	3.5	3.5	-	-	0.03	0.03	0.05
ME3	13	20	3.7	2	2.4	0.9	3.4	3.6	-	-	0.04	0.03	0.05
MERL 76	12.4	18.6	3.3	-	-	1.4	0.2	4.3	-	0.35	0.05	0.03	0.06
N18	11.5	15.7	6.5	0.6	-	-	4.35	4.35	-	0.45	0.03	0.15	0.15
N19	13.3	12.2	4.6	3		1.5	2.9	3.6		0.25	0.015	0.01	0.05
Nimonic 90	19.5	18	-	-	-	-	1.4	2.4	1.5	-	0.06	-	-
Nimonic 105	14.5	20	5	-	-	-	-	1.2	4.5	-	-	0.2	-
Nimonic PE.16	17.5	2	3.8	-	-	-	1.3	1.3	45	-	0.08	0.005	0.04
Rene 95	14	8	3.5	3.5	-	3.5	3.5	2.5	-	-	0.15	0.01	0.05
Rene88DT	15.8	13.1	4	3.9	-	0.7	2	3.7	-	-	0.05	0.016	0.045
RR1000	15	18.5	5	-	2	-	3	3.6	-	0.5	0.027	0.015	0.06
U720Li	16	15	3	1.25	-	-	2.5	5	-	-	0.025	0.018	0.03
Unitemp AF2-1DA	12	10	3	6	1.5	-	4.6	3	1	-	0.35	0.014	0.1

Despite the chemical complexity of the turbine disc alloys some general design rules still apply when determining alloy chemistry [2]. For most nickel-based superalloys a two phase microstructure is observed; consisting of a gamma (γ) matrix phase and gamma-prime (γ') precipitate phase. For the polycrystalline alloys small amounts of carbide and boride phases are required to strengthen the grain boundaries. The levels of alloying must be carefully controlled to ensure precipitation of undesirable phases – for example, topologically close packed (TCP) phases – does not occur. Figure 2.1 provides an overview of the elements typically used in nickel-based superalloys, indicating the phase to which they partition [6]. More detailed consideration of each of these phases is presented in subsequent sections.

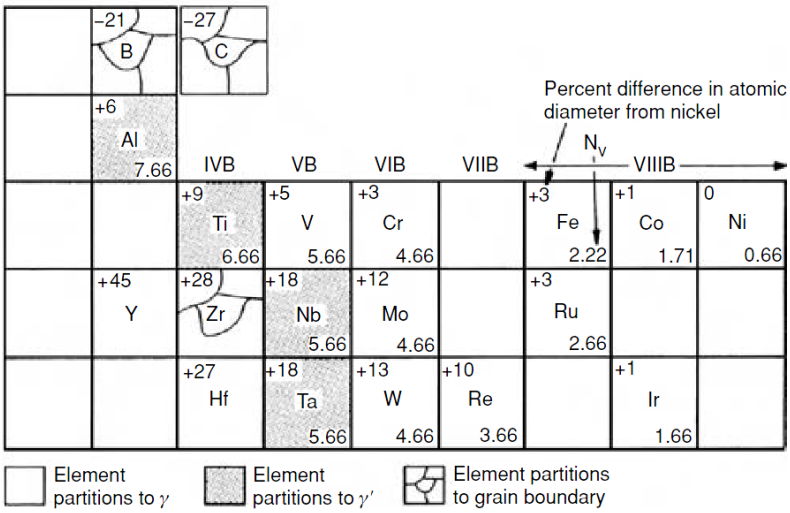


Figure 2.1: Categories of elements important to the constitution of nickel based superalloys along with their relative positions in the periodic table [6].

2.1.1 The γ phase

The austenitic γ phase is the matrix phase in which other phases reside. Elements from groups V, VI and VII of the periodic table strongly partition to γ [6]. Chromium (Cr), iron (Fe), molybdenum (Mo), tungsten (W) and cobalt (Co) are the most commonly used elements in the case of turbine disc alloys [7]. For turbine blade alloys the use of rhenium (Re) and ruthenium (Ru) is also prevalent [8]. Turbine discs rely on high levels of Cr to promote the formation of a protective oxide scale. Studies of the Ni-Cr system by Giggins and Pettit have shown that a minimum of 20 wt.% chromium is required for sufficient oxidation resistance [9]. Significant amounts of Co are often added as it has been found to improve the processing properties by lowering the γ' solvus temperature [10]. A low γ' solvus temperature is necessary to reduce the likelihood of cracking in turbine disc forgings during heat treatment [11]. Additions of Co are also beneficial for creep resistance as it lowering stacking fault energy in the γ phase [12].

Additions of Mo, W and Re are added to provide solid solution strengthening [13].

These solid solution strengthening elements also have a low diffusivity in nickel (Ni), this low mobility has been associated with improved creep resistance [2]. Despite the benefits of a highly alloyed γ phase caution is required, the elements which partition to γ phase promote the formation of deleterious phases [14]. For example Cr additions have been shown to promote the formation of σ phase [15, 16]. This explains why the level of chromium for most of the alloys in Table 2.1 is well below the minimum level of 20 wt.% suggested by Giggins and Pettit [9].

2.1.2 The γ' Phase

Precipitation of the ordered γ' phase, Ni_3Al, with the primitive cubic $L1_2$ crystal structure provides significant strengthening to nickel-based superalloys [3]. Figure 2.2 shows the crystal structure for the γ' phase, Ni atoms are located on the cube faces and aluminium (Al) atoms positionsed at the cube corners. Strengthening from this phase arises from the difference in Burgers vector for the γ and γ' phase, meaning dislocations in the γ phase cannot easily shear the γ' precipitates. Current generations of disc alloys typically contain 40-60% volume fraction of γ' to provide sufficient strengthening [7]. In the case of single crystal alloys used for turbine blades 65-75% volume fraction of γ' may be required for adequate creep resistance [8].

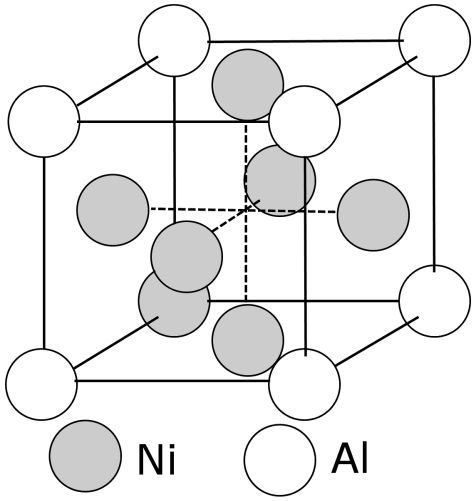


Figure 2.2: The crystal structure of the γ' phase.

Elements from group III, IV and V partition strongly to the γ' phase; for turbine discs titanium (Ti), tantalum (Ta) and niobium (Nb) are commonly used. These elements have been observed to occupy Al sites [17]. It has been found that these elements increase the anti-phase boundary (APB) energy of the γ' phase [18–23]. This is beneficial as hardening theory suggests that increased APB energy will promote higher tensile strength [24], this has been consider in more detail in Chapter 4.

The γ' and γ phases for a binary Ni-Al alloy are coherent due to their similar lattice parameter, 0.357 and 0.3517nm, respectively [2]. However, in multi-component alloys the composition of the γ and γ' phase will change the degree of mismatch resulting in changes of the γ' morphology. The lattice misfit between the two phases , δ, can be calculated using,

$$\delta = 2\left[\frac{a_{\gamma'} - a_{\gamma}}{a_{\gamma'} + a_{\gamma}}\right] \tag{2.1}$$

where a_{γ} and $a_{\gamma'}$ represent the lattice parameter for the γ and γ' phase, respectively. The composition of each phase can be used to calculate the lattice parameter using

Vegard's Law [25]. For very low levels of misfit, small spherical precipitates are observed and the rate at which precipitates coarsen is slow; eventually they will develop cuboidal precipitates during subsequent aging [26]. If the misfit is significantly large the growth of irregular octodendritic clover leaf shape precipitates is observed [26].

2.1.3 Grain Boundary Phases

Carbon (C), boron (B), hafnium (Hf) and zirconium (Zr) strongly segregate to γ grain boundaries. These elements act as grain boundary strengtheners improving resistance to creep and fatigue crack propagation [27]. Hence, much greater additions of these elements is seen in polycrystalline superalloys in comparison to directionally solidified or single crystal superalloys [2]. It is expected that these elements and their associated phases may improve grain boundary cohesion [28] reduce grain boundary sliding [29] and act as getters for deleterious 'tramp' elements [2].

Carbon additions promote the formation of carbide phases for example MC, M_6C, $M_{23}C_6$, M_7C_3, where M denotes a metal atom, typically Cr, Mo, Ti, Ta or Hf. Blocky MC type carbides can often precipitate at high temperatures above the γ' solvus temperature suppressing the growth of γ grains during heat treatment. Long term exposures of the MC phase at intermediate temperature – for example 760°C – results in a transformation to $M_{23}C_6$ according to the following reaction [6],

$$MC + \gamma \rightarrow M_{23}C_6 + \gamma' \tag{2.2}$$

The formation of the $M_{23}C_6$ carbide is generally beneficial, however, excessive amounts of the phase may result in the formation continuous films along the grain boundary. These continuous films can lead to brittle fracture in the alloy. Sufficient quantities of B in the alloy will lead to the formation of M_3B_2 borides. It is also believed that

B increases grain boundary cohesion [28]. The role of Zr and Hf appears to be as an getter for tramp elements, such as sulphur or phosphorous, introduced during the melt process [2].

2.1.4 TCP Phases

During processing or after long term service exposure, it is possible that phases deleterious to the mechanical performance of nickel-based superalloys may form. Some of the most common phases include sigma (σ), mu (μ), eta (η) and laves [3]. The need to include significant quantities of Mo, W, Co and Cr for increased creep and oxidation resistance may increase the propensity to the precipitation of these topologically close packed (TCP) phases. These phases have complex crystal structures with a limited number of slip planes; moreover they degrade the mechanical properties because of their brittle behaviour [2]. Also, as the TCP phases contain large quantities of refractory elements they can reduce solid solution strengthening in the γ phase of the alloy. The TCP phases generally precipitate in the vicinity of the grain boundaries as there is increased concentration of refractory elements in this region [30]. Hence, the precipitation of these phases can negatively impact upon creep and fatigue resistance in turbine disc alloys.

2.2 Processing Superalloys for Turbine Disc Applications

Turbine discs are normally manufactured using cast and wrought (C&W) or powder metallurgy (PM) methods. The process selected is dictated by the chemistry of the alloy [2]. Alloys which are not heavily alloyed and contain low fractions of γ', for example Waspaloy, are normally produced using the C&W process. Heavily alloyed materials which contain a greater fraction of γ', for example RR1000, usually require PM meth-

ods. When highly alloyed materials are processed using C&W methods substantial segregation is observed, this is not the case with the PM process. The alloys developed as part of this research require PM processing, therefore, only this production method is reviewed.

Figure 2.3 provides an overview of the processes required for the manufacture of a turbine disc using PM processing [31]. A master melt is produced using vacuum induction melting (VIM). This master melt is passed to the atomiser where the molten metal is directed into a stream of high pressure inert gas. The rapid solidification of the molten metal results in the formation of fine metallic particles with diameters between 30-300 μm. The powder is subsequently screened to remove oversized particles. The screened powder is collected in mild steel cans which are degassed and sealed. The canned powder is subjected to hot isostatic pressing (HIP) at a temperature just below the γ' solvus, this consolidates the powder. In some instances the canned powder is extruded as an alternative or supplement to the HIP process. Once the powder has been compacted the steel can is removed and the final billet is used to produce a turbine disc forging. The forging process is usually conducted in a specialised isothermal forging press.

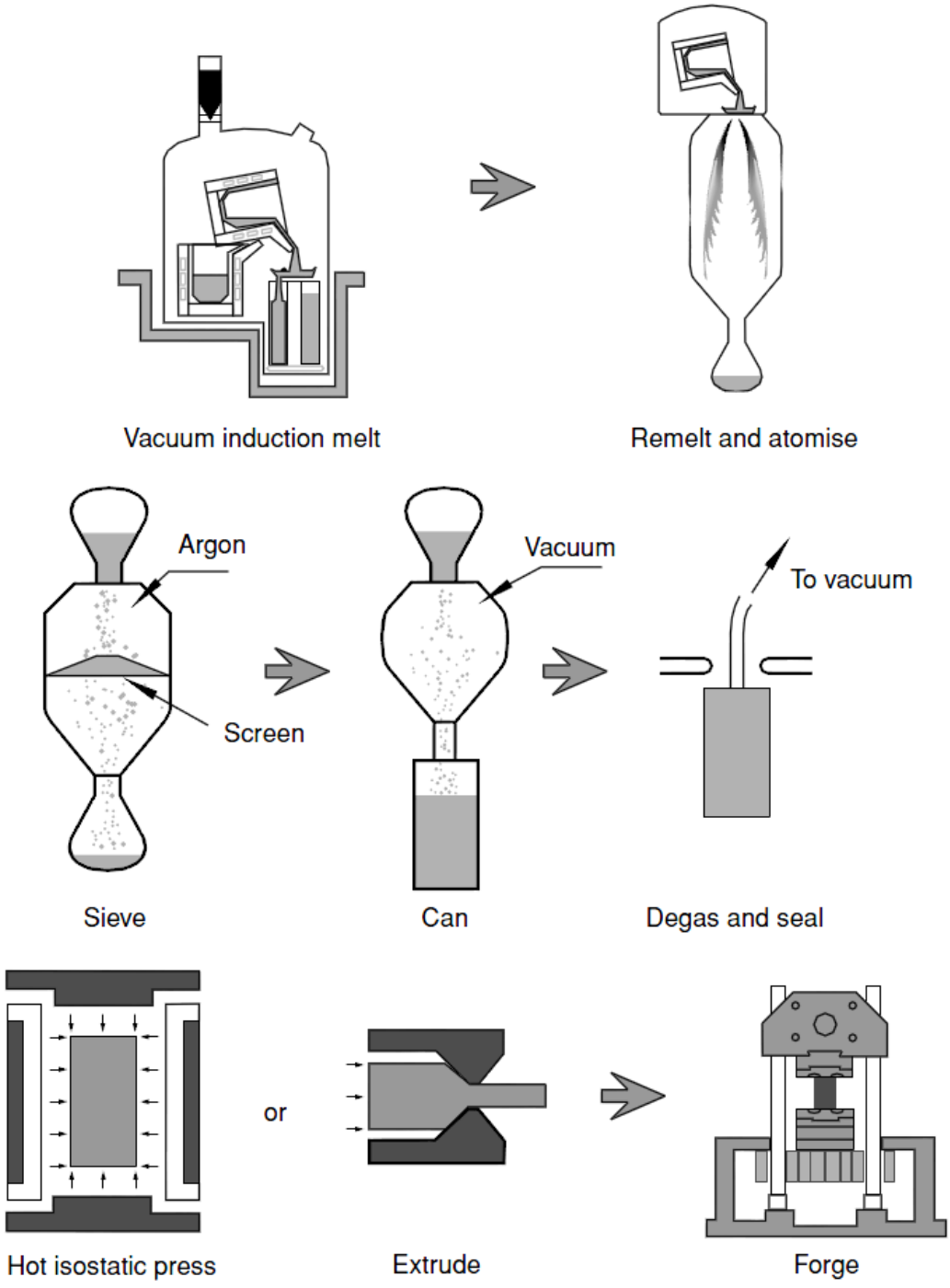


Figure 2.3: An illustration of the powder metallurgy process used in the production of turbine disc components. Adapted from [31].

Producing turbine discs using PM has significantly higher costs than the C&W route but there are advantages gained from the process. Due to the nature of the powder consolidation process the starting billet has a very fine grain size. The use of isothermal forging at slow deformation rates provides better control over grain size in comparison to C&W processing. Furthermore, the loss of expensive material is reduced as it is possible to produced near net shape compacts during the HIP process. Net shape manufacture can also reduce the time and complexity of component machining which has associated cost benefits. The main drawback of the process is the high degree of process control is required. Significant risks arise from the possibility of defects in the material. Some of the potential hazards include voids or prior particle boundaries remaining after consolidation and incorporation of ceramic inclusions into the material during the melt process. Ceramic inclusions typically originate from the crucible or nozzle used during the atomisation process.

2.2.1 Heat Treatment

The heat treatment of nickel-based superalloys plays a critical role in attaining an optimal balance of mechanical properties. Using thermal processing to modify the grain size as well as precipitate size and distribution can dramatically affect the mechanical properties for example creep resistance, tensile strength and fatigue life [2]. In general, it is seen that as grain size is increased tensile strength and fatigue life reduce whereas resistance to dwell crack growth and creep deformation is improved [32]. Normally, the heat treatment of turbine discs is a two step process, *(i)* solution heat treatment, *(ii)* aging heat treatment.

2.2.1.1 Solution Heat Treatment

The as forged turbine disc material has a fine grain size. The forging will have large intergranular primary γ' of diameter greater than 1 μm, there will also be intragranular secondary and tertiary γ' precipitates with diameters of approximately 50-350 nm and <50 nm, respectively. For the solution heat-treatment the alloy will be given either a sub-solvus or super-solvus heat treatment.

The sub-solvus heat treatment is conducted at temperatures near the γ' solvus, placing most of the γ' into solution. Some primary γ' will remain on the grain boundaries inhibiting grain growth through the Zenner pinning mechanism. A super-solvus heat treatment is conducted above the γ' solvus temperature, this will place all γ' into solution resulting in grain growth. The cooling rate at the end of the solution heat treatment will influence the final precipitate size distribution. Fast cooling rates are beneficial for mechanical properties as they promote a fine γ' distribution. However, as the disc component is significantly large, rapid cooling generates high stresses due to thermal gradients, this may result in quench cracking. For turbine disc components cooling rates range from approximately 0.5-1.5°C/s to reduce the possibility of quench cracking.

Previous generations of disc alloy have mainly relied upon the sub-solvus heat treatment, as the resultant fine grain microstructure provides substantial tensile strength. For new generations of turbine disc, the increasing operation temperature has made resistance to creep deformation and dwell crack growth is of greater concern. Therefore, a super-solvus heat treatment is preferred as increased grain size – often referred to as coarse grain – is beneficial for creep and fatigue resistance. The challenge for future alloy design is to select alloy chemistries where adequate tensile properties can be realised in the coarse grain microstructure, this is considered further in Chapter 4.

2.2.1.2 Aging Heat Treatment

After the solution heat treatment an aging heat treatment is conducted to complete the precipitation of the γ' phase. The aging process is typically conducted approximately 50°C above the operating temperature of the component to minimise coarsening of the precipitate during service. The time and temperature of the aging heat treatment is dictated by precipitation kinetics for the given alloy chemistry. The aim of the heat treatment is to develop the intragranular precipitates to the size which they are most resistant to precipitate shearing. There is an inverse relationship between precipitate size and mechanical strength i.e. as precipitate diameter increases resistance to shear decreases. Jackson and Reed showed clearly the strong effect that aging heat treatment can have on mechanical strength [33], with different aging times changing the yield strength and ultimate tensile strength of Udimet 720Li by 200MPa.

2.3 The Mechanical Properties of Turbine Disc Alloys

A range of complex trade-offs exist for the mechanical properties of turbine disc alloys [32]. These trade-offs may be managed by either modifying the alloy chemistry or the processing route [2]. The alloy chemistry may be modified so the microstructure is optimal for high strengthening, this is achieved by ensuring a sufficient fraction of γ' and grain boundary phases are present. Furthermore, the role of chemistry on the strength of individual phases must be considered. For example, reasonable levels of alloying are required in the γ phase to promote solution strengthening [13] and creep resistance [2]. The processing route must be optimised to control grain size, grain boundary character and γ' size and distribution, this can significantly influence mechanical properties [33]. The alloy chemistry and processing route are not independent of each-other. An advantage of the ABD method is that both mechanical properties and processing concerns

are considered. The following section reviews the strengthening mechanisms in turbine disc alloys, particular attention is given to tensile strength and creep resistance.

2.3.1 Tensile Strength

Tensile strength in turbine disc alloys is developed from a combination of different factors including, grain size hardening, strengthening from the γ matrix and precipitate hardening. Grain size hardening is limited in the newest generation of turbine discs as a coarse grain microstructure is necessary for improved creep and fatigue resistance. Strengthening is mainly from the γ matrix and γ' precipitate phase, this has been shown clearly by Kozar et al. [34] who presented a strength model for IN100 which could consider the effect of microstructural variations. Therefore, it is important to optimise the phase fractions and composition of the γ and γ' phases for sufficient strengthening in newly designed turbine disc alloys.

2.3.1.1 Strengthening from the γ matrix

Additions of Cr, Mo, W, and Co strengthen the γ matrix in turbine disc alloys. This strengthening may be explained by a number of different mechanisms [6]. Elements with a different atomic diameter than that of nickel can generate internal strains in the matrix. The strain fields created may inhibit dislocation motion within the matrix phase producing a strengthening effect. Solute additions may also lower the stacking fault energy (SFE) in the γ matrix, cobalt has been found to lower the SFE [12]. The stacking fault sequence in the γ matrix is $ABCABCABC...$. The addition or removal of a plane form this sequence is known as either an intrinsic or extrinsic stacking fault, respectively. In the fcc matrix the dominant slip system is the $a/2 < 1\bar{1}0 > \{111\}$. Observations using electron microscopy have confirmed that that these dislocations are dissociated into two shockley partial dislocations such that [2],

$$a/2 < 1\bar{1}0 > \{111\} \rightarrow a/6 < 211 > \{\bar{1}11\} + a/6 < 12\bar{1} > \{\bar{1}11\}$$

Lowering the stacking fault energy increases the distance between partial dislocations, making the movement of the dislocations more difficult as they must constrict to allow the patrials to cross slip. Optimising the levels of the elements which partition to the γ phase is critical, although they promote strength they also lead to microstructural instability [14].

2.3.1.2 Precipitation Strengthening

The majority of strengthening in turbine disc alloys comes from the coherent γ' phase Ni_3Al. The precipitates resist cutting as dislocations in γ have a Burgers vector of $a/2[1\bar{1}0]$ on the $\{111\}$ plane, but this is not a full dislocation in the γ' phase. Two dislocations with Burgers vector $a/2 < 1\bar{1}0 >$, or superlattice partial dislocations, are required to generate a full dislocation within the precipitate. In practice, a superlattice partial dislocation can enter the γ' precipitates forming a planar fault called an anti-phase boundary (APB). The order imposed by the $L1_2$ crystal structure is locally overcome by forcing undesirable first neighbour bonds, a trailing superlattice partial dislocation is then able to restore the ordered $L1_2$ structure.

Precipitate shearing will occur when the shear stress is large enough to force the leading partial dislocation to cut the γ' particle. Once this occurs an APB is formed. As the leading dislocation permeates through the γ' particle the surface area of the APB fault continues to grow increasing the attractive force on the trailing dislocation. Depending on the radius and volume fraction of γ' the superpartials may be either 'weakly' or 'strongly' coupled [2]. Shearing by weakly coupled dislocations will occur when an alloy is in an under-aged condition, meaning that there is a low volume fraction of γ' precipitates with a small radii, typically less than 30nm. The dislocations are said

to be weakly coupled as the separation between superpartials is much greater than the precipitate radius. This large separation between dislocations occurs because the leading dislocation may travel a relatively large distance before the APB grows to the point where it provides the attractive force necessary to pull the trailing dislocation though the faulted precipitate restoring order. When the volume fraction of γ' is high and the radii of precipitates is large – typical of an over-aged material – the dislocation pairs will be strongly coupled. This coupling occurs because the APB grows to the point where the attractive force on the trailing dislocation is sufficient enough to pull it through the precipitate after the leading dislocation has travelled a short distance through the γ' particle. Figure 2.4 provides an overview of the precipitate shearing mechanisms occurring; typically Orowan shearing is not observed in turbine disc alloys [34].

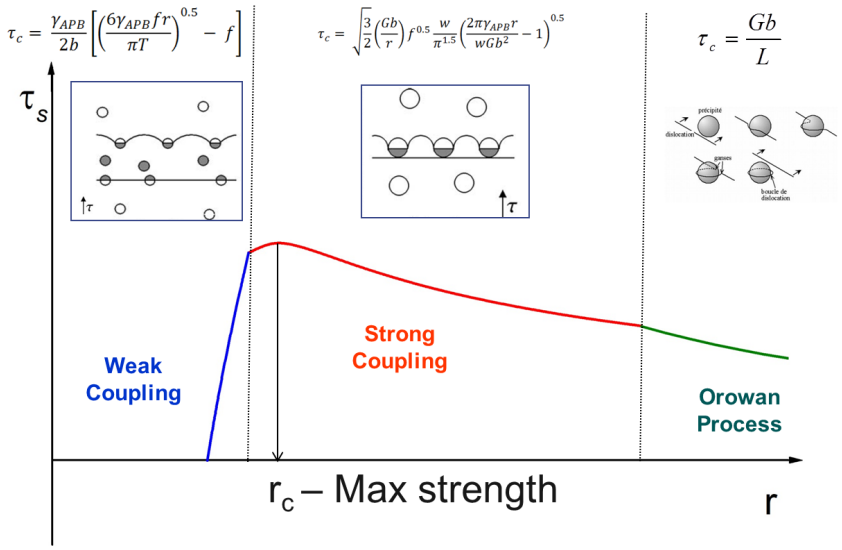


Figure 2.4: An overview of the precipitate strengthening mechanisms occurring in nickel-based superalloys.

The maximum precipitate strength occurs at the point where dislocation shearing transitions from the weakly to strongly coupled dislocation pairs. Reppich has confirmed

this through experimental testing [35,36]. At the critical radius it is possible to approximate the maximum strength of the precipitate to $1/2\gamma_{\mathrm{APB}}f^{1/2}/b$ [24], where γ_{APB} is the anti-phase boundary energy f is the volume fraction of γ' and b is the Burger's vector. From this approximation it is evident that strengthening in nickel-based superalloys is strongly dependant on the volume fraction the precipitate phase as well as the fault energy in the phase. In Chapter 4 this idea is extend to build a composition-property based model for flow stress in nickel-based superalloys. The influence of chemistry on fault energy and fraction of precipitate phase is considered.

2.3.2 Creep Resistance in Turbine Disc Alloys

As the turbine entry temperatures continue to rise the operational temperature for the turbine discs – especially in the rim section – continues to rise to the point where creep deformation is becoming significantly life limiting. It is therefore important to understand the factors which control creep deformation in these polycrystalline nickel based superalloys.

Changing the grain size as well as modifying the precipitation of carbide and boride phases at grain boundaries can help improve the creep resistance of the polycrystalline alloys. Increasing the grain size can improve the creep properties by reducing diffusion of vacancies at grain boundaries. The reduction in grain boundary area will also reduce the points of failure. Carbides located at the grain boundaries can inhibit grain boundary sliding, this can reduce the creep-strain rate. Caution is require when selecting the levels of grain boundary strengthening elements (C, B, Zr, Hf), if the grain boundary regions become heavily decorated with precipitates creep rupture life can be significantly reduced.

Changes to the the alloy chemistry and intergranular microstructure may also inhibit creep. Increasing the γ' volume fraction – through the addition of more γ' forming

elements – reduces the particle spacing. Furthermore, the increased number of particles reduces creep rate as dislocation may have to climb around obstacles as they are confined to the γ matrix. Additions of elements which partition to the γ phase is also important. Strengthening the matrix phase and reducing the stacking fault energy have been shown to improve creep resistance. The addition of slow diffusing elements, mainly W and Mo for turbine discs, has been found to be beneficial. The effect of slow diffusing elements on creep resistance is reviewed in greater detail in chapter 3

2.4 Developing Oxidation Resistance in Nickel-Based Superalloys

The increased operating temperatures for components within the hot section of gas turbines has made corrosion a more prevalent damage mechanism. Therefore, next generation nickel-based superalloys require increased corrosion resistance combined with improved mechanical properties. Engineering alloys form protective scales using Cr, Al or Si. These oxide scales provide an effective barrier from the environment because: they are thermodynamically stable at high temperatures, they do not react further to form volatile species, oxygen and metal ions diffuse slowly through the oxide and the protective scale has good adherence properties [37]. This section focuses on the effect of different alloying elements on the oxidation resistance of chromia forming turbine disc alloys. It highlights that elements added for the purposes of providing mechanical strength can significantly hinder the resistance of an alloy to oxidation.

2.4.1 The Thermodynamic Basis for Imparting Oxidation Resistance

The oxidation of a pure metal is described by the following reaction,

$$\frac{2\mathrm{x}}{\mathrm{y}}\mathrm{M(s)} + \mathrm{O_2(g)} \rightarrow \frac{2}{\mathrm{y}}\mathrm{M_xO_y(s)} \tag{2.3}$$

In order for this oxidation reaction to occur the change in Gibbs free energy (ΔG_f) must be less than zero. The Gibbs free energy of formation for the oxide $\mathrm{M_xO_Y}$ with 1 mole of $\mathrm{O_2}$ can be written as,

$$\Delta G_f = \Delta G_0 + RT \ln \left(\frac{a_{\mathrm{M_xO_Y}}^{2/\mathrm{y}}}{a_{\mathrm{M}}^{2\mathrm{x}/\mathrm{y}} P_{\mathrm{O_2}}} \right) \tag{2.4}$$

where, G_0 is the standard free energy of formation, R is the gas constant, T is temperature, $a_{\mathrm{M_xO_Y}}^{2/\mathrm{y}}$ is the activity of the oxide, $a_{\mathrm{M}}^{2\mathrm{x}/\mathrm{y}}$ is the activity of the metal and $P_{\mathrm{O_2}}$ is the partial pressure of oxygen. The activity of the oxide is taken to be unity. For equilibrium conditions, when $\Delta G_f = 0$, Equation 2.4 can be written as $\Delta G_0 = RT \ln P_{\mathrm{O_2}}$. From this it is possible to calculate the partial pressure required for oxide formation. The values for ΔG_0 can be found using the Ellingham diagram.

Figure 2.5 shows the Ellingham diagram where ΔG^0 for an oxide with 1 mole of $\mathrm{O_2}$ is plotted against temperature. This allows for comparison of the relative stabilities of different oxides, the lower the position on the diagram the more stable the oxide. For multi-component systems – where various oxides may form – the diagram can be used to predict the order of oxide formation. Theoretically, it is expected that the most stable oxide will form first. However, in practice kinetic effects may mean the first/prodominant oxide formed is not consistent with the Ellingham diagram. Futher consideration to the kinetics of oxidation is presented in Chapter 3.

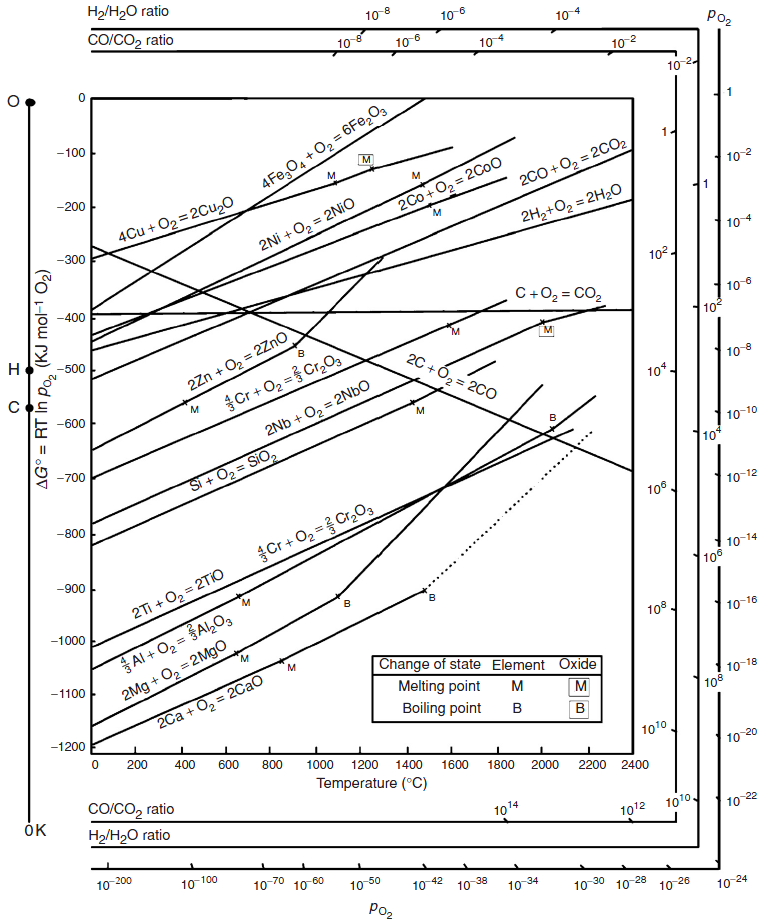


Figure 2.5: The Ellingham diagram, showing the standard free energy of formation for a selection of oxides, taken from [37].

2.4.2 Oxidation of Ni-Cr and Ni-Cr-Al

Typically, nickel-based alloys are designed to form either alumina (Al_2O_3) or chromia (Cr_2O_3) type protective scales. For turbine blade applications alumina scales are preferred as chromia will become volatile at temperatures beyond 1000°C forming gaseous CrO_3 [38]. Turbine discs operate below 1000°C, they are designed to produce a chromia protective scale as it has better adherence properties [39].

To improve the oxidation performance of nickel-based superalloys it is important to

understand the role of alloying in model alloy systems, for example Ni-Cr or Ni-Cr-Al alloys. The simplest comparison with turbine disc alloys is the Ni-Cr system, there have been numerous studies of these alloys over a range Cr levels and temperatures. Giggins and Pettit [9] studied the Ni-Cr system in great depth, their work showed that for alloys containing dilute levels of Cr – approximately less than 10 wt.% – resistance to oxidation is worse than that of pure Ni, Figure 2.6. It was concluded that at least 20 wt.% Cr is required to form a protective oxide scale. Preferably, additions of greater than 30 wt.% are necessary for the alloy to have oxidation resistance equivalent to that of pure Cr.

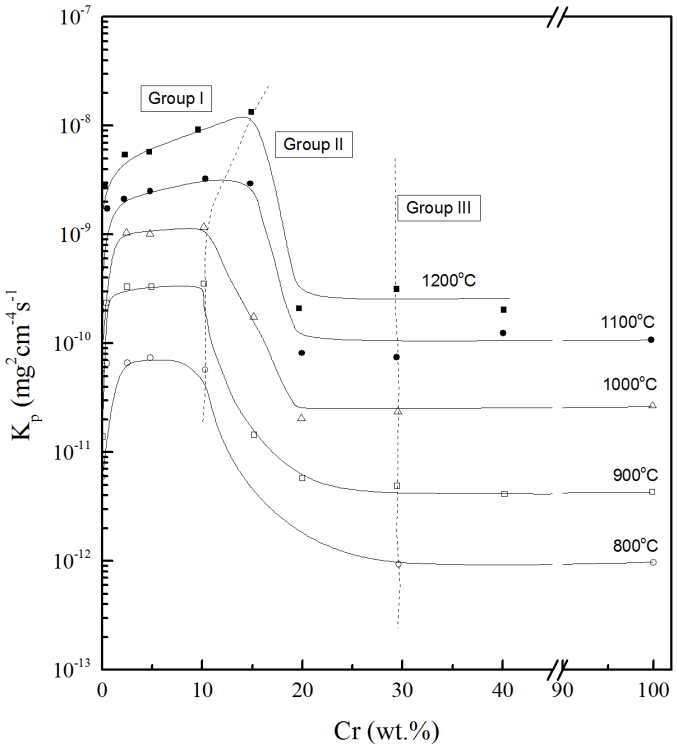


Figure 2.6: Composition dependance for parabolic rate constant for the oxidation of Ni-Cr alloys between 800°C and 1200°C [9].

Figure 2.7 [40] illustrates the the transient and steady state oxidation processes for Ni-Cr alloys which are lean or rich in Cr. For the alloy containing a high level of Cr, Figure

2.7a, the resultant steady state oxide scale consists of an external nickel oxide (NiO) scale with an internal protective Cr_2O_3 scale. At the interface between these scales the formation of a spinel phase ($NiCr_2O_4$) is observed. For dilute concentrations of Cr it is found that a thick external NiO scale is formed. The spinel phase may be distributed throughout the NiO scale, there is also formation of internal chromia oxides.

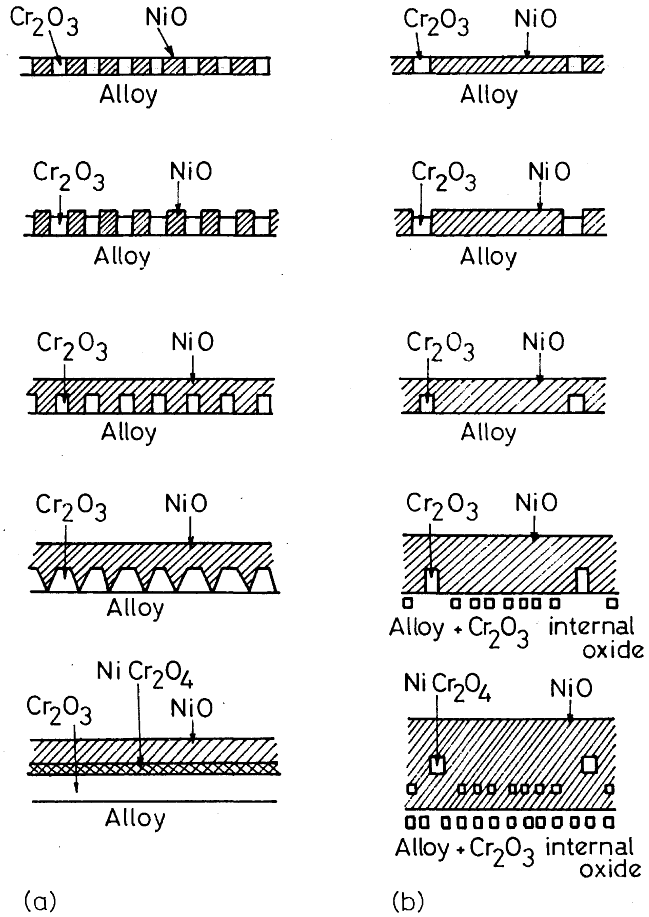


Figure 2.7: An illustration of the transient oxidation and steady state oxidation for a (a) Cr rich alloy e.g. Ni-(20-40)Cr, (b) a Cr lean alloys e.g. Ni-5Cr [40].

The oxidation of Ni-Cr-Al alloys provides a more accurate representation of the oxidation observed in commercial gas turbine engines as significant quantities of Al are added in order to promote the formation of the precipitate strengthening phase γ'. It

is shown by the Elligham diagram that Cr_2O_3 and Al_2O_3 are the most stable oxides which will form for more complex superalloys based upon the Ni-Cr-Al system. Giggins and Pettit [41] studied this system over a range of compositions, the results were used to construct an oxidation map for Ni-Al-Cr system, Figure 2.8, highlighting where different oxidation mechanisms will occur. Alloys could be divided into three different groups (I, II and III) based on their chemistry, each group represents a different oxidation mechanism.

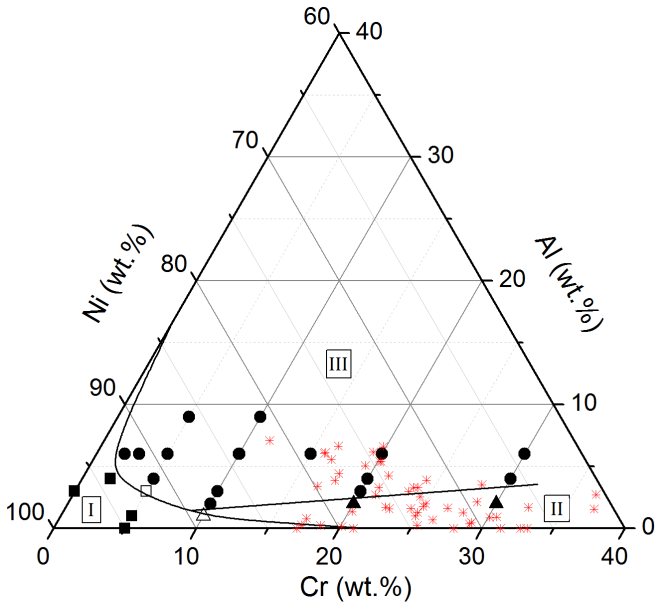
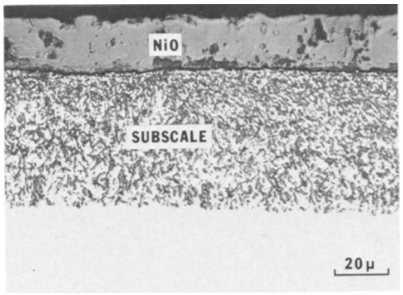


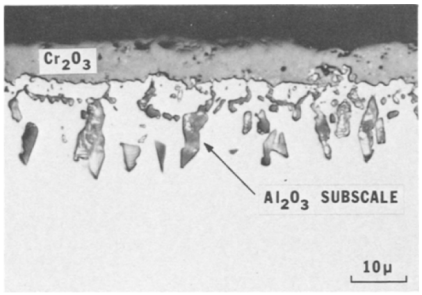
Figure 2.8: Diagram showing the compositional limits for three different oxidation mechanisms occurring in Ni-Cr-Al alloys in 0.1 atm of oxygen at 1000°C. There are three distinct regions *(I)* an external scale of NiO is formed, sub-scale chromium and/or aluminium oxides are formed, *(II)* an external scale of Cr_2O_3 is formed with sub-scale Al_2O_3, *(III)* only an external scale of Al_2O_3 is formed. Solid data-points correspond to areas where only one mechanism was observed, open data-points correspond to areas where both mechanisms were observed [41]. The red data-points show the position of a number of different turbine disc alloy compositions.

Alloys found in group I formed an external NiO scale with sub-scale chromium and/or aluminium oxides, a typical microstructure for a group I alloy is shown in Figure 2.9a. The alloys found in group II formed an external scale of Cr_2O_3 and sub-scale consisting of Al_2O_3, Figure 2.9b. The group III alloys formed an external scale of Al_2O_3, Figure

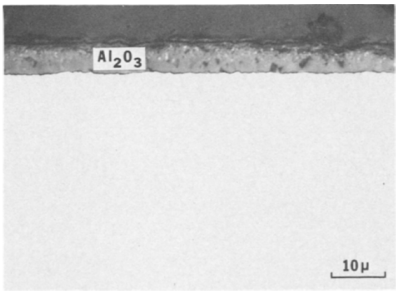
2.9c. The composition of a number of turbine disc alloys has been plotted on Figure 2.8, it is seen that the majority of the alloys lie in and around the group II region on the map. As the Group II alloys behave in a similar manner to alloys typically employed for turbine disc components discussion will be focused on alloys which behave in this manner.



(a)



(b)



(c)

Figure 2.9: Microstructure of an oxide representative of (a) group I alloy,(b) group II alloy,(c) group III alloy [41].

The Group II alloys in the Ni-Cr-Al system follow parabolic oxidation kinetics, with rate

constants similar to those of Ni-Cr alloys. For this group of alloys selective oxidation of Cr and Al leads to the formation of an external chromia scale with sub-scale alumina. The oxidation kinetics for alloys within this group is controlled by diffusion of Cr ions through the Al doped chromia scale. The high volume fraction of Cr_2O_3 reduces the flux of oxygen flux to the alloy, this lowers the oxygen activity inhibiting the formation of NiO. The reduced oxygen activity in the alloy may become so low that only the formation of internal Al_2O_3 oxides will occur, consistent with the Ellingham diagram. The growth of semi-continuous Al oxides slow the oxidation kinetics. From an alloy design perspective it would appear that additions of Al are beneficial for Cr_2O_3 forming turbine disc alloys. The 'third element effect' provided by Al slows the oxidation kinetics and promotes the formation of continuous Cr_2O_3 scales. Also additions of Al to Ni-Cr alloys reduces the Cr content required to form a continuous chromia scale. These improved oxidation characteristics are achieved alongside increased strengthening provided from Al which will promote the formation of the γ' precipitate phase. However, work by Wei and Stott [42] on Ni-28Cr and Ni-28Cr-1Al showed that although the oxidation kinetics are reduced, the levels of intergranular oxidation increases. These oxides develop in a dendritic manner along grain boundaries, this is problematic as oxide formation along grain boundaries may act as initiation site for failures during mechanical loading.

2.4.3 The Oxidation Characteristics of High-Strength Polycrystalline Superalloys

The oxidation mechanism occurring in chromia forming nickel-based superalloys is similar to that of the Group II alloys identified in the studies of Ni-Cr-Al by Giggins and Pettit [41]. An example of the oxide microstructure for RR1000 is presented in Figure 2.10 [43], as with the group II alloys there is a chromia scale with formation of what is

mainly sub-scale alumina.

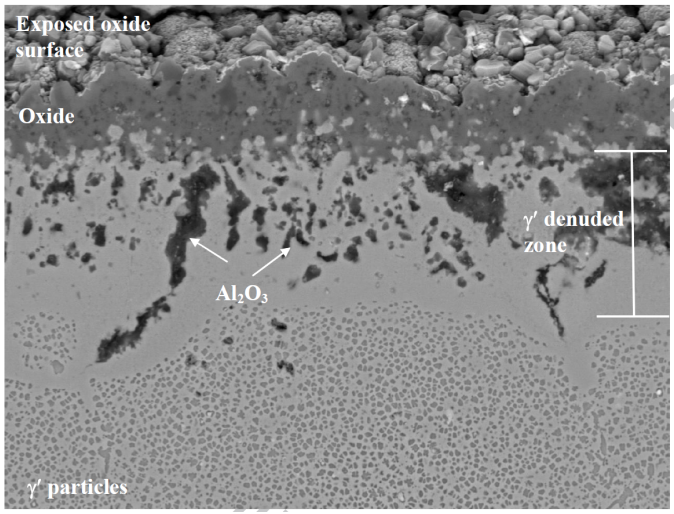


Figure 2.10: Typical cross section for a turbine disc alloy after oxidation damage. Example shows RR1000 after exposure in air at 800°C for 2000h, image taken from [43].

Based on the studies of the Ni-Cr and Ni-Cr-Al alloys it is expected that a suitably oxidation resistant alloy should contain a minimum of 20 wt.% Cr. However, the requirement for Al, Ti, Ta and Nb to form the precipitate strengthening phase, as well as Co, Mo and W for properties such as creep resistance usually limits the maximum Cr content well below 20 wt.%, see Table 2.1. The other alloying addition may also influence oxidation resistance. Hussain et al. [44] studied seven different chromia forming Ni-based superalloys with varied Cr contents. It was shown that although increasing Cr generally improved oxidation resistance, other alloying additions have a profound affect – both positive and negative – on the oxidation resistance. The Ellingham diagram confirms that there are a number of stable oxides that may form during oxidation of a multi-component superalloy. As the chromia forming alloys behave similar to Group II Ni-Cr-Al alloys the formation of significant amounts of NiO is not anticipated or desired. A more in-depth look at how Ti may influence the oxidation resistance of turbine disc alloys is considered in this section. Titanium has been found to be critical in

strengthening turbine disc alloys [45]. Hence, a trade-off between oxidation resistance and mechanical strength must be managed.

Nagai et al. [46] studied the deleterious effect of Ti on the oxidation of Ni-20Cr. Figure 2.11 clearly shows that additions of up to 3 wt.% Ti to a Ni-Cr alloys significantly accelerates the oxidation kinetics. The reduction of oxidation resistance was attributed to the substitution of Ti^{4+} for Cr^{3+} which affects the oxidation rate more than Ni^{2+}.

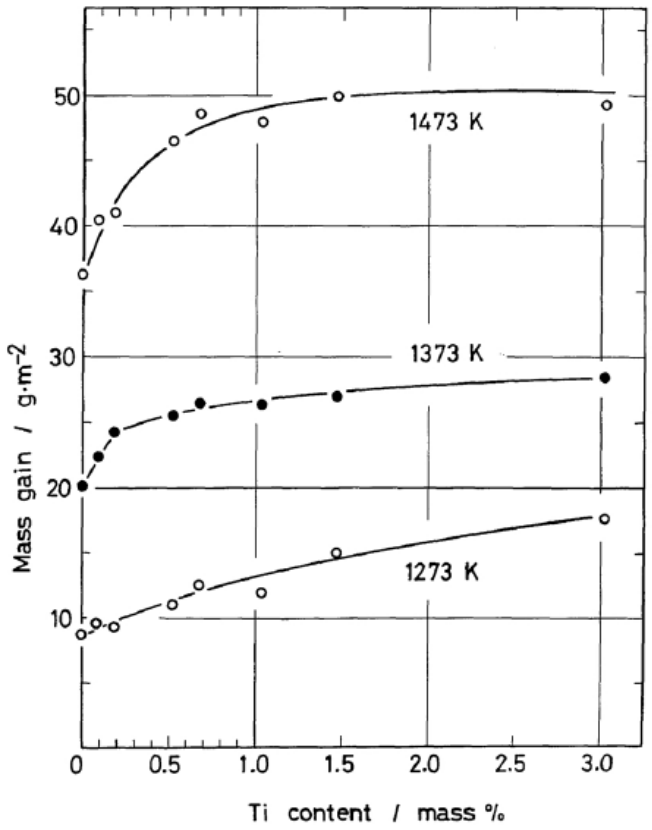


Figure 2.11: Mass gain after 20 hours of oxidation in air for Ni-20Cr alloys containing varied amounts of Ti [46].

The negative influence of Ti on oxidation nickel-based superalloys has also been reported for a number of different alloy compositions [43, 47–51]. Work by Chen et al. [47] to evaluate the oxidation of different alloys – Astroloy, Waspaloy, Udimet 720 – concluded

that the oxidation of these alloys could be considered as Group II Ni-Cr-Al alloys with the addition of Ti. Each study [43, 47, 48] reported that formation of TiO_2 occurs at both the oxide/gas and oxide/alloy interface. Buscail et al. [48] reported the deleterious role of Ti in the oxidation of Inconel 601 was due to increased cation vacancies resulting in faster chromium diffusion. This was described using the following,

$$\mathrm{TiO_{2(s)}} + \frac{3}{4}\mathrm{Cr^{x}_{Cr}} \rightarrow \mathrm{Ti^{\bullet}_{Cr}} + \frac{1}{3}\mathrm{V'''_{Cr}} + \frac{2}{3}\alpha - \mathrm{Cr_2O_{3(s)}} \tag{2.5}$$

where $Cr^{\mathrm{x}}_{\mathrm{Cr}}$ is a chromium ion in its normal state, $Ti^{\bullet}_{\mathrm{Cr}}$ is a TI^{4+} in in a Cr^{3+} site, V'''_{Cr} is a chromium vacancy site with three effective charges.

Abe et al. [51] provided a rationale for the wide distribution of Ti oxides in nickel-based superalloys in comparison to Al oxides which only form internally. This was based upon the diffusion co-efficient for different ions in their respective oxide. The mean diffusion distance – as a function of time – for Al ions in Al_2O_3 and Ti ions in TiO_2 was calculated and presented alongside Cr ions in Cr_2O_3, Figure 2.12. After 10^4 hours the mean diffusion distance for Al ions is 10 μm, implying Al ions are virtually immobile and their rate of growth is controlled by the inward diffusion of oxygen. On the other hand Cr and Ti ions are diffuse rapidly, approximately 1μm in 100 hours. Therefore, if the Ti ions had a similar diffusivity as Cr ions in Cr_2O_3 it would be possible for them to diffuse to the outer surface. This confirms reports in other studies where it is suggested that the oxidation kinetics are determined by the diffusion of Cr and Ti ions in turbine disc alloys [43, 47–51].

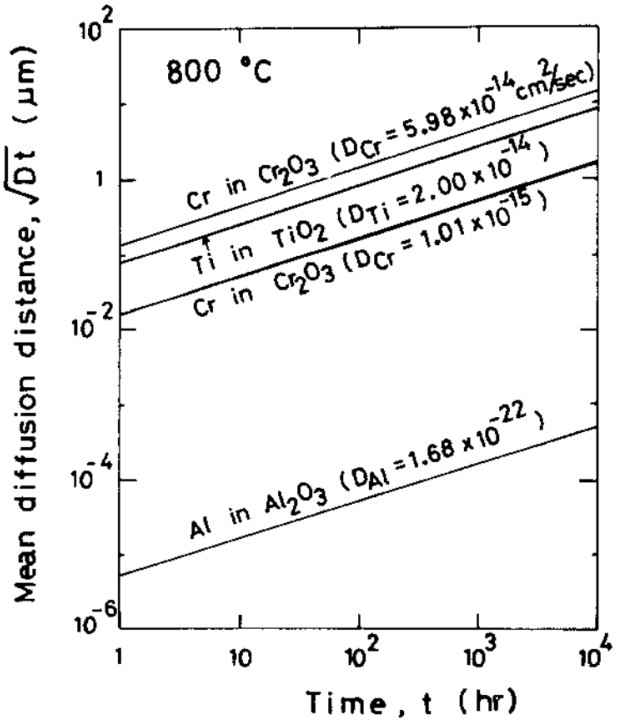


Figure 2.12: Mean diffusion distance for Al ions in Al_2O_3, Ti ions in TiO_2 and Cr ions in Cr_2O_3 as a function of time. The diffusion co-efficient of these ions at 800°C, shown in the parentheses in the figure, were evaluated by extrapolation of the Arrhenius relationship of diffusion coefficients measured at high temperatures [51].

3

Designing a Turbine Disc Chemistry Using the Alloys By Design Approach

3.1 Introduction

Nickel-based superalloys are remarkable for the range and number of alloying elements used in their constitution. Typical grades call for as many as ten alloying element additions. For example, (*i*) chromium and cobalt are added to promote resistance to oxidation and corrosion, (*ii*) aluminium, titanium, and tantalum to impart precipitation hardening, (*iii*) tungsten and rhenium to impart resistance to creep deformation, and (*iv*) zirconium and boron for grain boundary strengthening. At least in part, this situation arises because nickel displays a capacity to dissolve significant quantities of its neighbours from the d-block of transition metals. In this way, one can argue that superalloys – as a class of structural alloys – possess a degree of chemical complexity

which is rare and arguably unique. It has been pointed out recently [1] that this situation presents a challenge, since the many possible alloying elements means that the existing grades of nickel-based superalloys are unlikely to be optimised for their intended applications. Thus, alloy compositions superior to those currently available are likely to exist, thus waiting to be discovered or possibly be designed.

Traditionally, alloy design has invoked considerable use of trial-and-error based approaches involving costly and exhaustive processing backed up by empirical property testing. Consider, for example, the development of alloy N18 [52]. In this instance, alloys René 95, with its high strength, and Astroloy, with its superior resistance to crack propagation, were blended in various proportions with the aim of developing a more balanced alloy. In total over 50 different alloy chemistries were evaluated to reach the chemistry of alloy N18, which was subsequently selected for more comprehensive, scaled-up evaluation [53]. The prevalent use of empirical methods in design of nickel-based superalloys is also evident from Figure 3.1, on which the evolution of turbine disc alloy compositions patented over the past 50 years, binned into 5-year classes, is depicted. In this figure, each point represents the mean within each 5-year class and the whiskers point to the minimum and maximum in that class. It is clear that as time has progressed, no particular trend towards higher or lower levels of any of the alloying elements has occurred. This level of arbitrariness in the composition of the alloys, albeit in part, can be attributed to the reliance of alloy design methods on experience and empiricism.

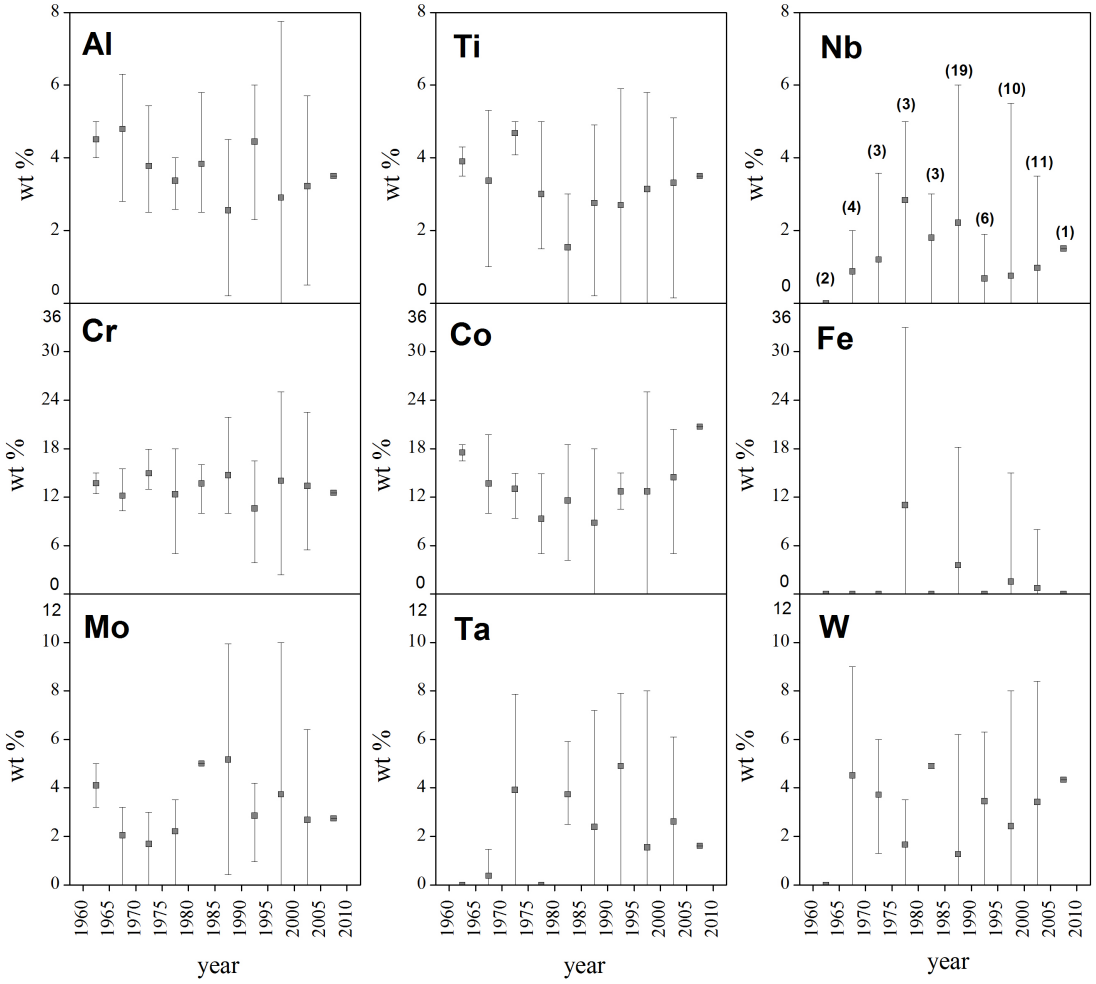


Figure 3.1: Timeline of the chemistry of select patented nickel-based disc alloys binned into 5-year classes. The points represent the mean of the concentrations of the alloying elements in each class and the whiskers point to the maximum and minimum of the concentrations deduced from the patents. The so-called 'preferred' compositions are noted for each element. The numbers listed in parentheses on the Nb plot are the number of patents examined for each case. For example, 19 disc alloy patents were examined which were published between the years 1985 and 1990.

Given the breadth of available alloy design space, one cannot hope to find new grades of superalloys by continuing the inefficient and costly past practices; it is crucial to take advantage of computer-based modelling and analysis tools that facilitate expedited identification of new grades of alloys and, ultimately, allow for a much closer integration of component design, manufacturing intent, and materials aspects at greater

cost-effectiveness. As materials models and modelling strategies mature, in conjunction with development of reliable thermodynamic and kinetic databases, the utility of the noted tools in design of superalloys is becoming all the more apparent; this is demonstrated by the works of Small and Saunders [54], Tancret et al. [55], Yokokawa et al. [56], and Reed et al. [1].

In this Chapter, computer-based modelling and analysis tools are applied for the 'virtual' characterisation and evaluation of composition design spaces for nickel-based superalloys. An aim is to demonstrate the manner by which such methods allow quantitative relationships between alloy constitution and properties to be developed, so that future alloy development efforts might be guided. Attention is focussed on the polycrystalline superalloys used for turbine discs, e.g. those utilised in gas turbines for jet propulsion and power generation. Their primary role is to provide fixturing for the turbine blades while maintaining their integrity under the demanding in-service conditions. We expand upon the Alloys-By-Design modelling framework [1], which was recently applied to single crystal superalloys; the present work complements this first effort. The Chapter is organised as follows: first, in Section 2, a brief overview of the Alloys-By-Design framework is provided. The different models, merit indices, and modelling strategies used in this framework are described. In Section 3, the results of the analysis are presented, demonstrating the various trade-offs that exist between different characteristics and properties of disc alloys. An assessment of the modelling approach, property trade-offs, and how the trade-offs may be managed are considered in Section 4. Finally, in Section 5 the concluding remarks are presented.

3.2 Modelling Methodology

The basic premise of the Alloys-By-Design approach, see [1], is the estimation of design-relevant properties across a very broad compositional space, so that alloy composition/property relationships can be identified. In principle, this allows the so-called inverse problem to be solved – the identification of an optimum alloy composition which best satisfies the given design constraints. Needed for success are property sub-models which are sensitive to alloy chemistry. The basic algorithm involves [1] (*i*) defining the compositional design space over which the optimisation is to be attempted, (*ii*) choosing suitable compositional intervals over which the calculations are made, (*iii*) calculation of composition and microstructure dependent merit indices for each trial alloy composition, and (*iv*) assessment of each trial composition against the design constraints, and elimination of unsuitable compositions and (*v*) the sorting/ranking of remaining compositions and identification of optimised compositions.

Superalloys used for turbine discs must display a combination of strength – both static and time-dependent – and resistance to environmental degradation. Microstructural stability is also important. The original formulation of the Alloys-By-Design approach [1] was aimed at single crystal superalloys for turbine blades. Although the working conditions for a turbine blade involves higher temperatures and lower stresses as compared to turbine discs, comparatively similar property requirements are demanded from the two, e.g. low density and high creep resistance. Therefore, many of the models presented in [1] are likely to be applicable and will be utilised here.

3.2.1 Estimation of Phase Equilibria

Both desirable and undesirable phases may form in nickel-based superalloys at various stages of their service life [2]. To determine the relative fraction of these phases for

the different chemistries investigated, use here is made of Thermo-Calc coupled with the TTNI7 database [57]. The equilibrium calculations are performed at 650 °C, a temperature representative of typical operating conditions for a turbine disc. Two equilibrium calculations are performed per alloy composition. First, an equilibrium calculation to identify the phases present when the alloy enters into service and second, an equilibrium calculation to identify the phases that form due to prolonged exposure to in-service temperature.

The state of the alloy when entering into service is simulated by assuming that only the γ (FCC-A1) and γ' phases are present. Thus, the mole fractions of these phases – taken to be approximately equal to their volume fraction – were calculated by imposing a two-phase equilibrium on the selected compositions. At this stage, no other phase was assumed to enter into the equilibrium. Note that the yield strength, creep resistance and oxidation resistance calculations described later were all performed based on this equilibrium. The state of the alloy after a long period in service – where the stability of the alloy and its susceptibility to formation of topologically close-packed (TCP) phases is of concern – was simulated by assuming a three-phase γ, γ', and σ equilibrium. Once again, the presence of all other phases is suppressed by rejecting them at the onset of the equilibrium calculations. It is well documented that the σ phase formation significantly deteriorates the performance of nickel-based superalloys [15]. Recent work of Seiser et al. [58] has demonstrated that formation of the σ phase correlates strongly with the formation of other TCP phases; accordingly, only σ was considered in this work.

Thermo-Calc was also used to assess the γ' solvus temperature for each alloy composition. Consideration of the γ' solvus temperature serves as a measure of the processibility of the alloys; work by Gayda et al. [11] has demonstrated that there is a correlation between the quench crack susceptibility and the γ' solvus temperature. In this work,

the solvus temperature is defined as the temperature at which the γ' volume fraction reaches zero. Figure 3.2 shows a comparison of γ' solvus temperatures taken from the literature [10, 59–65] and those calculated in this work.

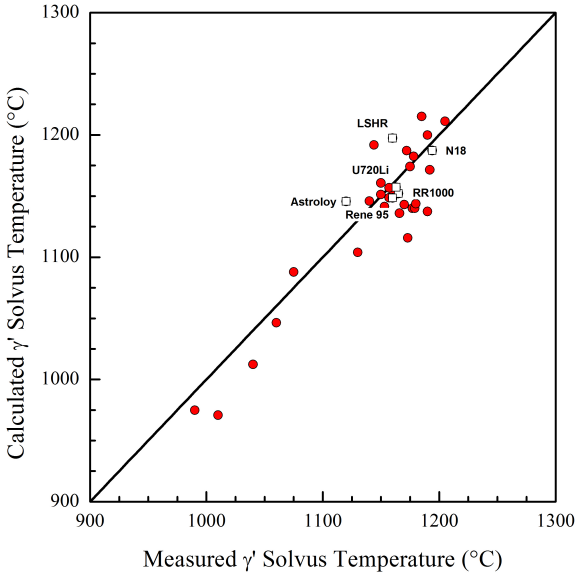


Figure 3.2: Comparison of the calculated and measured γ' solvus temperatures for a number of different nickel-based superalloys. Measured values are those reported in the literature [10, 59–65]. Select commercial alloys are delineated.

3.2.2 Estimation of Yield Strength

At the time of designing the new nickel-based turbine disc alloys a theory-based composition-dependent yield strength model was not available, development of such a model is detailed in Chapter 4. Therefore, a Bayesian Artificial Neural Network (ANN) following [66] is used to isolate the alloys in Chapter 3. The reader is referred to [66] for a detailed description of the formulism of this ANN model. In brief, the model architecture utilised in this study consists of one hidden layer comprised of 32 hidden neurons. The hidden layer connects the inputs of the model (i.e. alloy chemistry in wt%, volume fraction of γ', and temperature) to the model output (i.e. yield strength). A hyperbolic tangent function is used for the hidden neurons, due to its flexibility when fitting to

data [67].

To train and test the ANN model, the model made use of a database constructed from data contained within *i)* the literature [2, 53, 59, 62, 64, 68–77], *ii)* commercial nickel-based superalloy datasheets (from The Special Metals Corporation and Haynes International Inc.), and *iii)* industrial patents [61]. The database contained information on 56 commercial and 69 experimental/development alloy compositions. Considering the different temperatures taken into account for each of the 125 (= 56 + 69) compositions, a total of 428 unique cases were included in the database. Table 3.1 identifies each individual input for the neural network along with the corresponding maximum and minimum values within the training database. The model used a supervised training process, i.e. the database was divided in half at random, allowing for a training and a test data set. The final neural network considered 14 different alloying elements, the volume fraction of γ' in the alloy, and the test temperature as inputs. The γ' volume fraction is calculated using Thermo-Calc as described in Section 2.1. Inclusion of the γ' volume fraction as an input into the model follows [45] where it was suggested that inclusion of this microstructural feature may improve the accuracy of the neural network's predictions.

Table 3.1: Range of input and output values included in the neural network database (compositional ranges are in wt%). The minima are zero unless otherwise stated

Input	Range
Cr	31.50
Co	26.20
Mo	28.00
W	14.00
Ta	7.00
Nb	6.50
Al	5.00
Ti	6.20
Fe	45.00
Hf	2.00
C	0.95
B	0.20
Zr	0.50
γ'_{vf}	0.68
Temperature (^{o}C)	21 - 800
Output	**Range**
Yield Strength (MPa)	165 - 1310

Figure 3.3 shows the correlation between experimental and neural network predictions for the training and test data in the trained network.

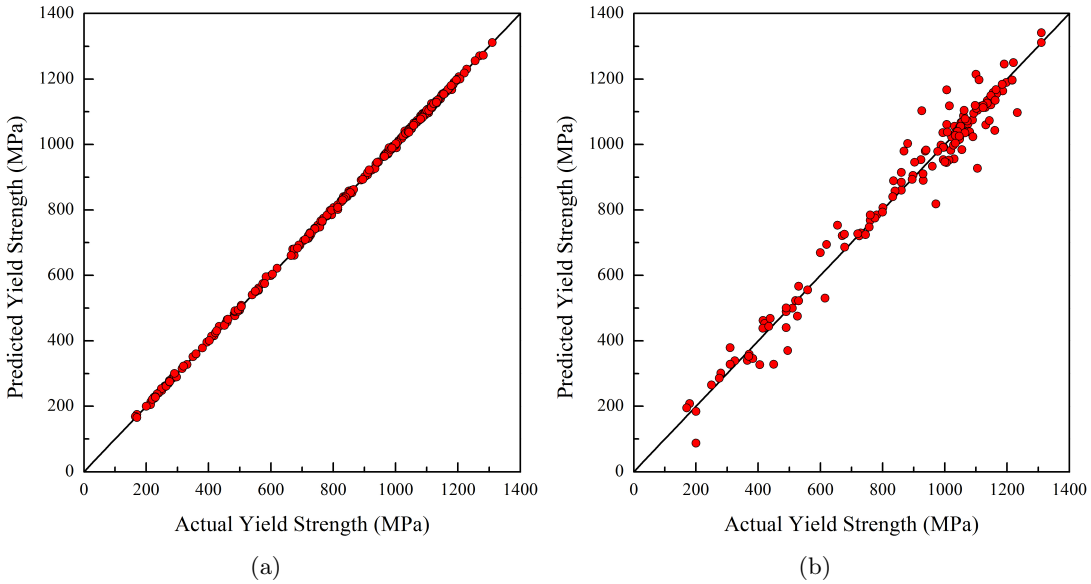


Figure 3.3: Performance of the neural network compared with data contained in the (a) training set and (b) testing set.

3.2.3 Estimation of Oxidation Resistance

Typical turbine disc alloys may contain between 10-20 wt% of chromium. The chromium additions are made to improve oxidation resistance via the promotion of a protective chromia scale [47, 78–80]. Accordingly, the relevant oxidation reaction for these alloys may be written

$$\frac{4}{3}\mathrm{Cr} + \mathrm{O_2} \rightarrow \frac{2}{3}\mathrm{Cr_2O_3} \tag{3.1}$$

The kinetics of chromia scale growth may be described by Wagner's theory [81]. Based on this theory, the parabolic oxidation constant, k_t, is taken to be proportional to the Gibbs free energy of chromia formation, $\Delta \mathrm{G}_f$. Thus,

$$k_t \propto \Delta G_f \tag{3.2}$$

Considering the chromia reaction presented in Equation 3.1, Equation 3.2 may be rewritten as,

$$k_t \propto \left\{ \Delta G_o + RT \ln \left(\frac{a_{\mathrm{Cr_2O_3}}^{2/3}}{a_{\mathrm{Cr}}^{4/3} P_{\mathrm{O_2}}} \right) \right\} \tag{3.3}$$

where ΔG_0 is the standard free energy of formation, R the universal gas constant, T the absolute temperature, $a_{\mathrm{Cr_2O_3}}$ activity of chromia, a_{Cr} activity of chromium, and $P_{\mathrm{O_2}}$ the partial pressure of oxygen. Taking $a_{\mathrm{Cr_2O_3}}$ to be unity and $P_{\mathrm{O_2}}$ equal to 0.23 atm (in 1 atm of air), the parabolic oxidation constant is found to be inversely proportional to a_{Cr}. In this work, a_{Cr} is used as a measure for assessment and ranking of the oxidation response of different alloy chemistries. The higher the activity, the smaller the parabolic oxidation constant would be and, accordingly, the better the oxidation resistance. In this analysis, the activity of chromium is calculated for the alloy system of interest using Thermo-Calc with a two-phase equilibrium imposed.

3.2.4 Estimation of Creep Resistance

To rank the creep resistance of different alloy compositions, it is assumed that the un-pinning of dislocations from pinned configurations is rate-controlling. Following [1] and assuming that the rate-controlling processes of diffusion represent a very first approximation, one writes

$$M_{\mathrm{creep}} = \sum_i \frac{x_i}{D_i} \tag{3.4}$$

where x_i is the atomic fraction of solute i in the alloy and D_i is the interdiffusion coefficient for solute i with nickel. The interdiffusion coefficients are expressed by

$$D_i = D_{0i} \,.\exp(-Q_i/RT) \tag{3.5}$$

where D_{0i} is a pre-exponential term, Q_i is the activation energy for diffusion, R is the universal gas constant (8.3145 J mol^{-1} K^{-1}), and T is the absolute temperature.

3.2.5 Estimation of Density

For the calculation of density, a simple rule-of-mixtures based on the densities of the pure elements and scaled by a factor of 1.05 is used, i.e.

$$\rho = 1.05 \times \left[\sum_i x_i \rho_i \right] \tag{3.6}$$

following [1]. Here, x_i is the atomic faction of alloying element i and ρ_i is its density. The values for the different parameters introduced in the above equations are taken from the literature [82–84] and are provided in Table 3.2.

Table 3.2: Various constants used in this work [82–84].

Element	D_0 m^2/s	Q kJ/mol	ρ g/cm^3
Cr	1.25×10^{-4}	267	7.220
Co	1.80×10^{-4}	282	8.900
Mo	8.53×10^{-4}	270	10.220
W	8.00×10^{-6}	264	19.300
Ta	2.19×10^{-5}	251	16.650
Al	1.87×10^{-4}	268	2.300
Ti	4.10×10^{-4}	275	4.508
Ni	-	-	8.902

3.3 Results

The composition design space selected for the present analysis is the Ni-Cr-Co-Al-Ti-Mo-W-Ta system, illustrated in Figure 3.4. The alloying elements and their corresponding composition ranges are typical of industrial-grade turbine disc superalloys. Note that the present composition space lies within the patent space for disc alloys, Figure 3.4. In addition to the delineated elements, trace elements Zr, C, and B are also included in the analysis at fixed concentrations of 0.06 wt%, 0.027 wt%, and 0.015 wt%, respectively. Noted in Table 3.3 are the composition limits considered in this work.

To evaluate this space, the design space was randomly sampled while considering only whole-number (integer) wt% variations for each of the elements. In total, in excess of 22,500 different compositions were analysed within the bounds of the composition design space.

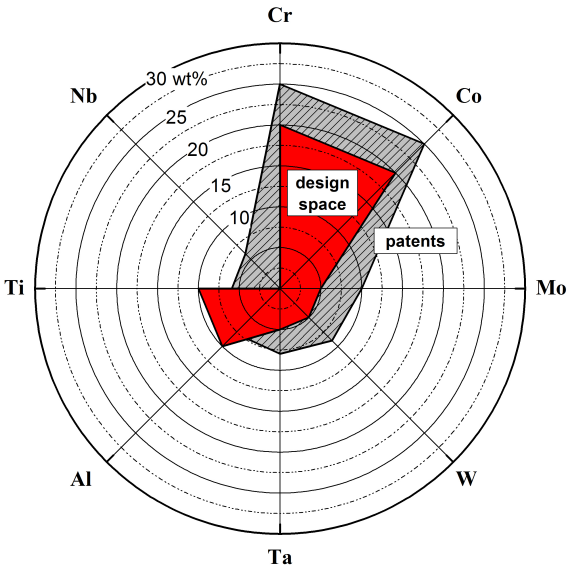


Figure 3.4: Limits of the composition design space used in the present study (Table 3.3). The extent of the patented compositional space for nickel-based disc alloys (Figure 3.1) is also delineated.

Table 3.3: Limits of the composition design space used in the present study

Element	Min wt%	Max wt%
Cr	15	20
Co	15	20
Mo	0	5
W	0	5
Ta	0	5
Al	1	8
Ti	1	10
Zr	0.06	0.06
C	0.027	0.027
B	0.015	0.015

Figure 3.5 gives an overview of the trade-offs observed between the γ' volume fraction and the two predicted mechanical behaviour characteristics studied here: yield strength and creep resistance. It can be seen from Figure 3.5a that there is a general trend towards higher yield strengths as the volume fraction of γ' in the alloys is raised. However, there is a spread in the yield strength values for a fixed volume fraction of γ'. This spread is especially notable for volume fractions greater than approximately 40%. At such high volume fractions, the overall correlation between the γ' volume fraction and yield strength becomes weaker. In contrast to the yield strength values, the calculated creep merit indices do not have any correlation with the volume fraction of γ', as shown in Figure 3.5b.

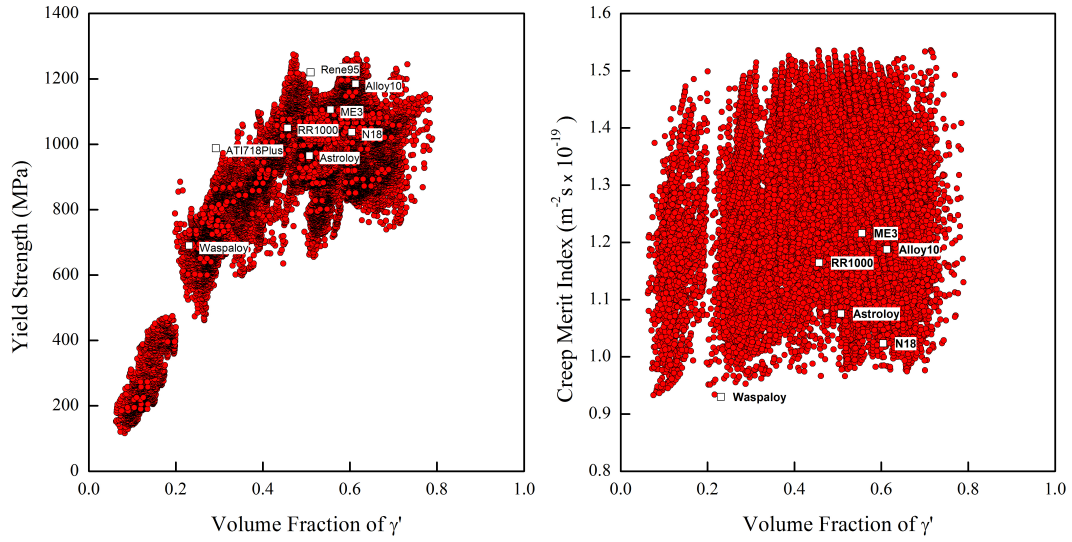


Figure 3.5: Predicted (a) yield strength and (b) creep merit index as a function of γ' volume fraction at 650 °C.

Figure 3.6a shows that, in general, an increase in the γ' volume fraction results in a reduction of the density of the alloys. The data are, however, clustered into a number of distinct groups. A strong correlation between γ' content of the alloys and the γ' solvus temperature is also evident, as shown in Figure 3.6b. Similar to yield strength, the

dependence of γ' solvus temperature on γ' volume fraction becomes less pronounced beyond γ' volume fractions of 40%. Once again, at these volume fractions there is an increase in the spread of γ' solvus temperature.

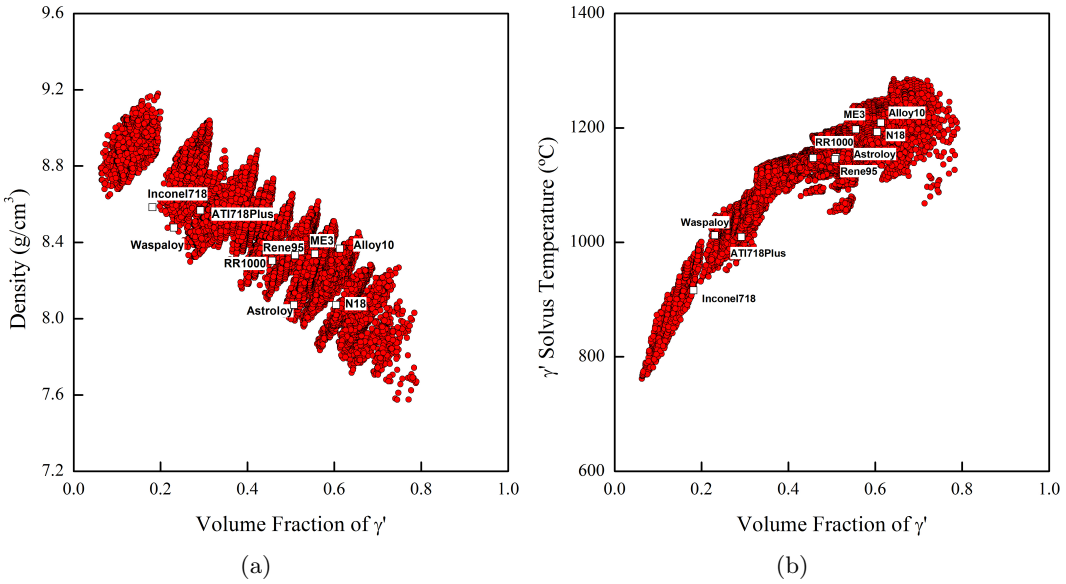


Figure 3.6: Predicted (a) density and (b) γ' solvus temperature as a function of γ' volume fraction at 650 °C.

The trade-off between γ' volume fraction and volume fraction of σ phase (i.e. alloy stability) is depicted in Figure 3.7a. It is evident here that by increasing the γ' content of the alloy, the propensity of the alloy to detrimental, σ phase formation also increases. A notable feature of this diagram is the significant spread in calculated properties. It is also important to note that at γ' contents greater than approximately 55%, formation of σ phase is unavoidable. Figure 3.7b shows that the stability of the alloy has a close correlation with the activity of chromium, a_{cr}, which as outlined in Section 2.3, is taken to be associated with an oxidation resistance. This figure shows that increasing the activity of chromium in the alloy makes the alloy more unstable. Care should, however, be taken in highlighting this general correlation given that, once again, there is a considerable spread in the data.

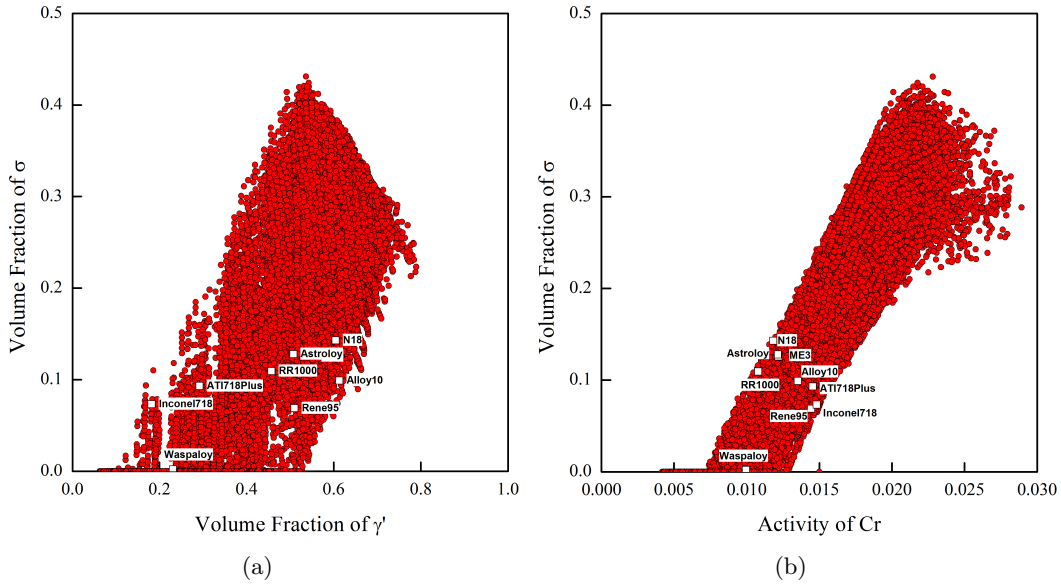


Figure 3.7: Predicted σ volume fraction as a function of (a) γ' volume fraction and (b) chromium activity at 650 °C.

It is emphasised that the predicted values for a number of common industrial disc alloys are superimposed on all the aforementioned trade-off diagrams. These data points are included on the diagrams to highlight areas where improvements in present disc alloys may be attained.

3.4 Discussion

To deliver improved efficiency for future gas turbines, the thermal efficiency of the turbine's thermodynamic cycle must be increased. This is achieved by using higher pressure ratios, higher turbine entry temperatures, and higher rotational speeds [85]. However, these goals cannot be met unless materials that can withstand such demanding conditions are identified. The alloys used for turbine discs are examples. The stress and temperature distribution across a turbine disc creates a demand for a mixture of high performance characteristics. High stresses at moderate temperatures in the

hub of the disc demand high yield and tensile strengths combined with resistance to low cycle fatigue. The rim of the disc, operating at much higher temperatures, must have resistance to creep and stress rupture, as well as good tensile strength and dwell fatigue resistance [86]. These alloys must maintain their integrity in a demanding environment to deliver an acceptable component life. At these high temperatures the alloy must remain stable and resist degradation due to corrosion and oxidation processes. Therefore, the overarching goal when designing new alloy chemistries is to achieve the highest temperature capability where reasonable component life is still achievable. In Section 4.1 the factors limiting the mechanical behaviour of a turbine disc, particularly its yield strength, will be discussed and in Section 4.2, the factors which limit the life of a turbine disc alloy will be discussed.

3.4.1 Mechanical Behaviour Considerations in Design of Alloys

Figure 3.5a demonstrates that at a given volume fraction of γ' there can be a significant spread in alloy strength. For example, consider the locations of Astroloy and René 95 on this plot. These alloys have very similar γ' contents but their yield strengths differ by approximately 160 MPa at 650 °C. Clearly, alloy chemistry is one of the main factors responsible for this variation in yield strength. In Figure 3.8a, the impact of the molybdenum and tungsten content of the alloy on yield strength is depicted. It is evident here that at a fixed γ' volume fraction, molybdenum and tungsten – which predominantly partition to γ – increase the yield strength. This is in agreement with the experimental work by Mishima et al. [87]. These authors found that among the elements which preferentially partition to the γ matrix, molybdenum and tungsten provided the most substantial solid solution strengthening effect. Similarly, Gayda and Gabb [88] observed that additions of up to 3 wt% tungsten to disc alloy CH98 produced a 70 MPa increase in yield strength of the alloy at 704 °C. The beneficial effect of these

elements in optimisation of alloy strength is also reported in the development of alloy RR1000 [2], LSHR [5], and Allvac 718 [89].

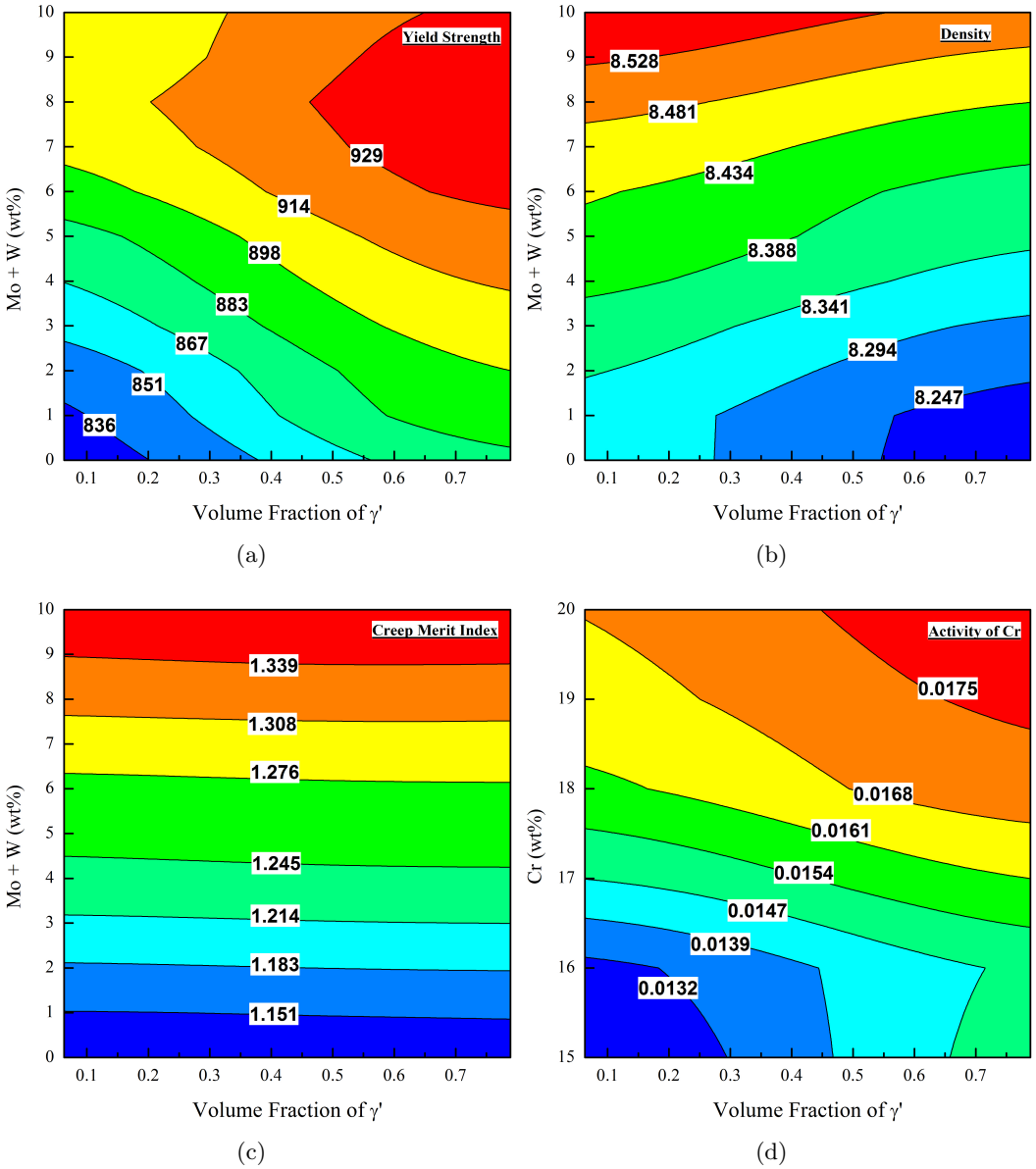


Figure 3.8: Contour plots showing the effect of different alloying elements and γ' volume fraction on (a) yield strength in MPa, (b) density in g/cm^3, (c) creep merit index in m^{-2}s $\times 10^{-19}$, and (d) activity of chromium.

The spread in yield strength at a given volume fraction of γ', Figure 3.5a, is too large to

be explained solely by strengthening of the γ matrix. The overarching factor controlling this spread is most likely the chemistry of the γ' phase itself. Changes in the chemistry of γ' have an impact on the anti-phase boundary (APB) energy of this phase and, accordingly, on the precipitation strengthening effect of the alloy. Among the different strengthening mechanisms in nickel-based superalloys, precipitation strengthening has been found to have a very pronounced effect, c.f. Nembach [90] and Kozar et al. [34]. Tantalum [18], titanium [91] and niobium [23] have been shown to increase the APB energy of the γ' phase. The APB energy strongly determines the magnitude of precipitate strengthening at a fixed volume fraction of γ'. This is evident from Equation 3.7 which describes the maximum strengthening effect from the precipitates [2],

$$\sigma_{y_{\text{peak}}} = \overline{M} \, . \, \frac{1}{2} \gamma_{\text{APB}} f^{1/2} / b \tag{3.7}$$

Here, $\sigma_{y_{\text{peak}}}$ is the maximum yield strength contribution from precipitates, $\overline{M}$ is the mean Taylor factor, γ_{APB} is the APB energy of γ', f is the volume fraction of γ', and b is the magnitude of the Burgers vector. It is hypothesised here that the variation in APB energy explains the increasing spread of yield strength at volume fractions of γ' greater than 40% as seen in Figure 3.5a. As the γ' volume fraction increases, precipitation strengthening becomes the dominant strengthening mechanism, meaning the distribution in strength is then driven by variance in the APB energy. An example of how changing APB energy can be used in alloy design is highlighted in the development of NR3 alloy [62]. In this development, N18 was used as the base chemistry; the γ' content of the alloy was maintained while its molybdenum was removed to improve stability. The aim was for NR3 to be as strong as N18 but to counteract for the reduction in solution strengthening due to removal of molybdenum, an increase in the Ti/Al ratio (in at%) from 0.6 to 0.9 was utilised [62]. The tensile properties of NR3 are equivalent to N18, this is possible because titanium additions raise the APB energy [91],

increasing the magnitude of strengthening from precipitates and, thus, balancing the loss in solid solution strengthening. It is to be noted here that the neural network used in this study does not explicitly account for APB energy or for that matter, precipitation or solid solution strengthening effects. However, these effects are implicit in the database used for the training of the model.

Neural network models have found utility in predicting the yield and tensile strength of polycrystalline nickel-based superalloys, see e.g. [45, 55, 92]. Although a good approximation of alloy strength is achieved using this method, there is still a limit to the understanding which can be deduced from the model. To obtain a more comprehensive understanding of alloying effects on the yield strength of nickel-based superalloys, a phenomenological model can certainly provide a greater insight. In particular, such models would ideally allow the complicated correlation between chemistry, microstructure, and processing/service parameters to be evaluated. This is demonstrated in the recent work of Kozar et al. [34]. These authors have successfully described the yield strength of IN100 by considering the various strengthening mechanisms that come into play in nickel-based superalloys and by explicitly taking into account the different microstructural features of superalloys that impact the yield strength (e.g. size of precipitates). However, extending this work to other nickel-based superalloys does require further work as the chemistry dependence of the different variables of the model is yet to be established. In particular, the chemical dependance of APB energy. Although first-principles calculations [93] and thermodynamic modelling [94] have been applied to understand the chemical dependance of the APB, an increased understanding of this chemical dependance is certainly needed for future development of high strength nickel-based superalloys.

When developing an alloy for high strength it is important to consider density, as an input into specific strength. Figure 3.6a shows that an increase in γ' content reduces

the density of the material. This decrease may be understood in terms of the increased additions of aluminium and titanium which are required to raise the γ' volume fraction of the alloy. This correlation between γ' content and density is highly advantageous as increasing γ' content will increase the yield strength, see Figure 3.5a and Equation 3.7. Another issue to be treated is that at a given volume fraction of γ', there is a spread in density. This spread in density is a consequence of the addition of heavy refractory elements molybdenum, tungsten and tantalum. As shown in Figure 3.6a, there is also a clustering of the data in this plot. These clusters represent the sum of Ti+Al, each cluster shows a small increase in γ' content with a corresponding increase in density. This correlation is explained by tantalum additions, which increases the volume fraction of γ' phase but since it is heavier than nickel, it increases the density. Figure 3.8b shows that at a given volume fraction of γ', molybdenum and tungsten additions increase density. Cobalt and chromium additions have little effect on density as they have a density similar to that of nickel.

Having observed the above trade-offs and correlations, the obvious choice when designing a high strength, low density alloy would be to move towards higher γ' contents and to make little use of refractory elements. However, considering Figures 3.6b and 3.7a, it can be seen that the γ' content must be selected with caution. A high γ' content is predicted to correspond to an increase in both the γ' solvus temperature and the susceptibility of the alloy to TCP phase, σ, formation. Considering that Figure 3.6a shows that the γ' content is related to the Ti+Al content it is suggested that there is an upper limit to this value. As indicated earlier in Section 2, work by Gayda et al. [11] showed that a high γ' solvus temperature makes an alloy more prone to quench cracking and, thus, makes its making processing more difficult. An alloy with a high propensity to σ formation will show a rapid deterioration in mechanical properties. Furthermore, the refractory elements are essential to improving creep resistance, Figure 3.8c. It is, therefore, necessary to take all these considerations into account.

Figure 3.8c shows that for a given volume fraction of γ' the creep resistance increases with additions of tungsten and molybdenum. This agrees well with the experimental work conducted on CH98 [88] where additions of 3wt% tungsten to CH98 gave a five fold increase in 0.2% creep life at 704 °C. In development of alloy, ME3, [86] the importance of these elements for creep resistance is also highlighted. It is noted there that a tungsten content between 2-4 wt% and a molybdenum content of greater than 2 wt% is required to maintain adequate creep resistance. The current creep model assumes that creep is a diffusion controlled process. Therefore, as shown in Equation 3.4, the elements which diffuse slowest in nickel impart the greatest creep resistance. The results presented in Figure 3.5b suggest the volume fraction of γ' has no influence on creep resistance. However, the size and distribution of γ' precipitates may lead to the operation of a variety of deformation mechanisms [95]. At the intermediate creep temperatures considered in this work it is assumed that dislocation climb is the dominant deformation mechanism [3]. Inclusion of the effects of microstructure through a phenomenological model based upon sound theory does merit further investigation.

3.4.2 Lifing Considerations in Design of Alloys

Chromium is added in significant quantities to improve corrosion resistance, promoting the formation of a protective chromia scale [47]. Figure 3.8d shows the change in the activity of chromium at a given volume fraction of γ'. For a given volume fraction of γ' additions of chromium increase the activity of chromium in the system. Based on the merit index described earlier it is predicted that an increase in the chromium activity will produce an improved oxidation resistance. This is consistent with observations of the Ni-Cr [9] and Ni-Cr-Al system [41] where increased levels of chromium improved the formation of a continuous chromia scale. In Figure 3.9, the a_{Cr} for the Ni-Cr compositions examined in [9] is calculated, the increased chromium activity correlates

with a reduction in the parabolic rate constant.

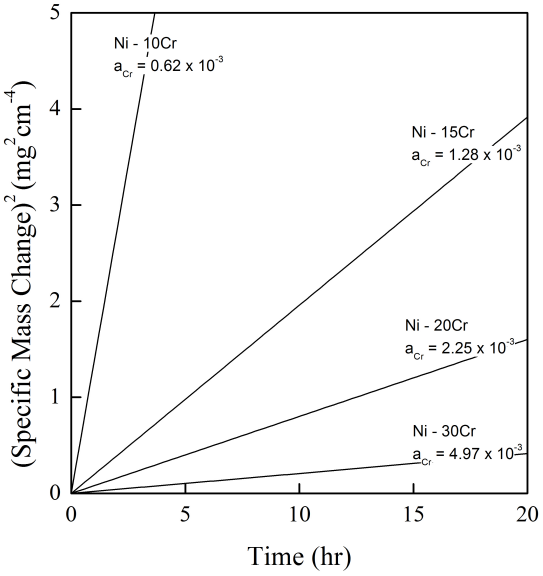


Figure 3.9: Oxidation data for Ni-Cr binary alloys at 900 °C in 0.1atm of O_2, adapted from [9]

The assumption that oxidation resistance is purely controlled by chromium is rather crude. Although it does provide a basis for ranking oxidation performance, previous studies have shown that consideration must also be given to other active elements within the alloy system [47, 78–80]. Upon oxidation, the structure and chemistry of the scale is much more complex than that assumed in the present study. In particular, it is understood that the aluminium and titanium content of a superalloy also influences the oxidation response of the alloy. For example, Chen et al. [47] showed that a high titanium content can have a significant detrimental effect on the oxidation performance of an alloy. There is still more work required to characterise and model the oxidation resistance of different alloys based on their chemistry. We believe the work of Sato et al. [96] provides a good basis for such developments.

Figure 3.8 indicates that improvements to the mechanical properties and oxidation resistance can be met by high levels of alloying. This suggests that to develop alloys

for next generation of gas turbines, a higher degree of alloying is required. Figure 3.10a shows that the problem is perhaps more complex. Firstly, as shown in figure 3.7a volume fractions of γ' beyond approximately 55% will lead to a high propensity to the precipitation of the σ phase. Also, depletion of nickel within the alloy raises the propensity to σ formation and this increase in instability due to excessive alloying might ultimately lead to an unacceptable component life. Figure 3.10b shows that in particular raising the molybdenum and tungsten content of the alloy for strength and creep resistance, and chromium for improved oxidation will increase alloy instability. At a given volume faction of γ' these elements must be used in balanced proportions as they contribute significantly to volume fractions of σ in the alloy. Past work has shown that reducing chromium levels can control stability; Udiment720Li was developed by reducing the chromium levels of Udimet720 [15]. In the development of the RR1000 alloy a balance had to be struck between the levels of chromium and molybdenum in the alloy [85], chromium was maximised at the expense of molybdenum, meaning a reduction in high temperature strength and creep resistance.

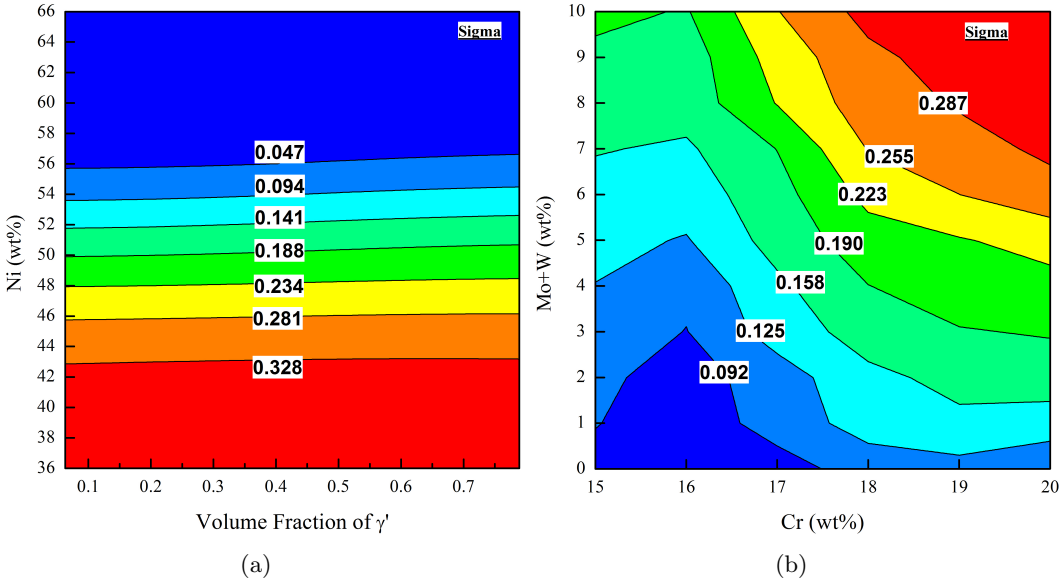


Figure 3.10: Contour plots showing the variation of σ volume fraction with (a)nickel content and γ' volume fraction and (b) molybdenum, tungsten, and chromium content of the alloy.

3.4.3 Example: Management and Optimisation of Alloy Chemistries

A close examination of Figures 3.8 and 3.10 shows that the minima and maxima delineated on these plots do not coincide with each other according to the design requirements. For example, the maximum yield strength region in Figure 3.8a is at the top, right-hand corner while the minimum density region in Figure 3.8b is at the bottom, right-hand corner. This highlights the trade-off necessary between yield strength and density. The work presented in this Chapter is aimed at giving the reader guidance to make informed decisions when developing a new disc alloy. An example of how this approach can be implemented in the development of a new alloy, considering the outlined trade-offs, is presented below.

In Section 3, Figures 3.5 - 3.7 demonstrate the importance of selecting an appropriate γ' content. Consider a γ' content of approximately 50%, which is typical of many

recently developed disc alloys. This γ' content gives the designer a good range of values for material properties taken into account in this work, see Table 3.4. Once the γ' content has been selected, the trade-offs can be balanced considering Figures 3.8 and 3.10. Figure 3.11, which is a duplicate of Figure 3.10b, highlights the key design options which can be made to optimise the alloy. The main limiting factor is the alloy stability. By reducing chromium content, the stability of the alloy can be improved but oxidation resistance will be reduced as shown in Figure 3.8d. Alternatively, by reducing the Mo+W content, stability will improve. However, strength and creep resistance will likely be lost, Figures 3.8a and 3.8c. By changing both the Cr content and the Mo+W content, the designer can achieve a balanced trade-off, i.e. a likely optimal alloy. It is to be noted here that the previous two sections demonstrate that the Alloys-By-Design predictions do align with empirical observations reported in the literature. It is, however, acknowledged that confirmation of predicted 'optimal alloy' chemistries, as determined through the approach presented in this section, by experimental validation is necessary.

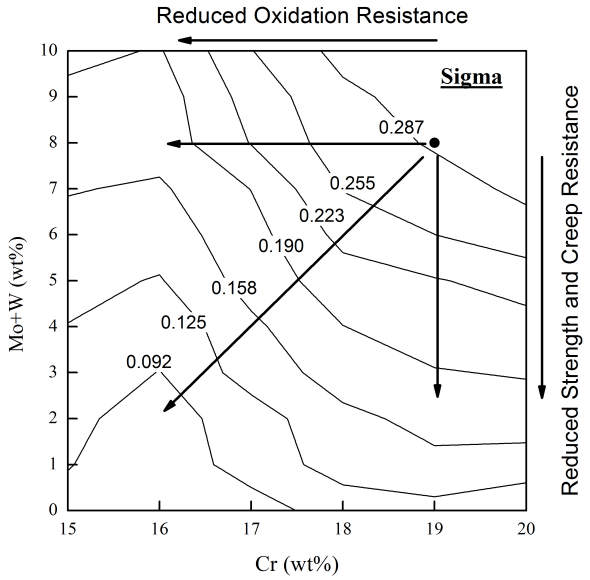


Figure 3.11: A case study showing how the Alloys-by-Design method can be used to optimise alloy properties at a given volume fraction of γ'.

Table 3.4: Range of alloy properties predicted at approximately 50% volume fraction of γ'

Property	Range
Yield Strength (MPa)	662 - 1186
Activity of Chromium	0.00949 - 0.02178
Creep Merit Index ($m^{-2}s \times 10^{-19}$)	0.977 - 1.51
Density (g/cm^2)	7.989 - 8.654
Volume Fraction of σ	0.0 - 0.4
γ' Solvus Temperature (^oC)	1053 - 1198

Finally, a note on the architecture of the Alloys-By-Design approach employed here. First, in this study consideration is given only to the γ, γ', and σ phases. It is, however, acknowledged that a hierarchy of phases, desirable and undesirable, may form in these complex alloy systems. Many of these phases, even though not present at high fractions, do have a pronounced effect on a number of properties. Consider, for example, the impact of carbides and borides on the mechanical response of nickel-based superalloys [97–99]. A comprehensive alloy design programme does need to account for these phases; a necessity for such a goal to be realised is the availability of sound thermodynamic databases that can adequately model such phases. Second, there is still a large scope for integration of more models within the Alloys-By-Design approach to obtain a more comprehensive alloy design tool. Many properties which limit the success of a disc alloy still have to be understood, e.g. fatigue crack propagation and resistance to sulphidation. Furthermore, models such as the yield strength model and the creep model presented in this work require further development to give a greater insight into how chemistry controls these factors. True optimisation of alloy chemistries will not be realised until our understanding of these properties is improved further.

3.5 Summary and Conclusions

The following conclusions can be drawn from this work:

1. The utility of an Alloys-by-Design modelling approach for the evaluation of compositional design spaces relevant to nickel-based superalloy turbine discs is demonstrated. The Ni-Cr-Co-Al-Ti-Ta-Mo-W(-Zr-C-B) system is considered, and alloys within this system are ranked based on their resistances to mechanical and environmental degradation and microstructural characteristics, e.g. fraction of γ', γ' solvus temperature, propensity to σ precipitation.

2. The activity of chromium in an alloy is utilised as a measure of its resistance to oxidation. It is found that chromium additions correlate with improved oxidation resistance. However, a trade-off between improving oxidation resistance by this method and maintaining acceptable alloy stability exists.

3. A Bayesian artificial neural network is used to predict the yield strength of the alloys as a function of their chemistry and temperature. The γ' volume fraction – estimated via Thermo-Calc calculations – is included as an additional input parameter into the neural network. The predicted yield strengths correlate with the concentration of molybdenum and tungsten in the alloys.

4. The propensity for σ phase formation (i.e. a measure of alloy stability) is found to correlate closely with the level of alloying. A higher degree of alloying induces greater alloy instability. In particular, molybdenum, tungsten, and chromium are found to have a pronounced effect on instability.

5. The model predictions are used to construct chemistry-property maps. The maps demonstrate graphically the trade-offs that exist between different properties. These are useful for pedagogical pursues.

6. The application of the developed chemistry-dependent trade-off maps in optimisation of nickel-based disc superalloy has been demonstrated via a number of examples.

7. The Alloys-by-Design methods are ultimately only as accurate as the underlying validity of the underlying sub-models and databases, e.g. for thermodynamic properties. The methods are already valuable, but will become increasingly so as further improvements in the sub-models and the introductions of new ones are made to the system.

4

Modelling of the flow stress of Nickel-Based Supealloys

4.1 Introduction

The nickel-based superalloys display excellent high temperature mechanical properties, particularly in creep and fatigue [100–102]. But why is this? The overarching reason is that deformation on the microscale is restricted by the precipitation hardening conferred by a significant fraction of the $Ni_3(Al, Ti, Ta)$ phase, which is commonly referred to as gamma prime (γ'). The origin of this effect cannot be explained by differences in the elastic moduli of matrix and precipitate, since these do not differ greatly from phase to phase. Instead, it is the fault energies associated with anti-phase boundaries (APBs) and stacking faults (SFs) which are responsible for it [103, 104]. Their magnitudes severely limit the penetration of the γ' phase achieved by the dislocations introduced during deformation, and thus bulk plastic flow.

It follows that the fault energies are of great significance to the physical metallurgy of

nickel-based superalloys. This is emphasised further by considering theoretical expressions which describe the how yield strength varies in the alloy with respect to precipitate size and distribution. Take the case of so-called weakly and strongly coupled dislocations; Equations 4.1a and 4.1b describe permeation of a superalloy containing a fraction f of precipitates. The shear yield stress τ_y varies according to [2]

$$\tau_y = \frac{\Delta E_{\mathrm{APB}}}{2b}\left[\left(\frac{6\Delta E_{\mathrm{APB}} f r}{\pi T_L}\right)^{1/2} - f\right] \tag{4.1a}$$

$$\tau_y = \sqrt{\frac{3}{2}}\left(\frac{Gb}{r}\right) f^{1/2}\frac{w}{\pi^{3/2}}\left(\frac{2\pi\Delta E_{\mathrm{APB}} r}{wGb^2} - 1\right)^{1/2} \tag{4.1b}$$

for the cases of weakly and strongly-coupled dislocations respectively. Here, ΔE_{APB} is the APB energy, b is the Burgers vector, r is the mean precipitate radius T_L is the line tension, G is the shear modulus of the γ phase and w is a dimensionless constant to account for uncertainties, which is expected to be of the order of unity. One can see that the APB energy is expected to influence the flow properties substantially. Moreover, some of the dependence of mechanical strength on alloy chemistry is due to differences in the APB energy, which depends upon the chemistry of the γ' phase. Elements such as Ti and Ta which partition strongly to γ', which thus influence the APB energy, might therefore be expected to enhance the yield stress. The stoichiometry of $\mathrm{Ni_3(Al, Ti, Ta)}$ is also likely to be important. But calculations are needed to deduce the precise details of these quantitative relationships.

The work reported in this Chapter was motivated with the above in mind. We set out to identify quantitative alloy composition/mechanical property relationships in polycrystalline nickel-based superalloys. Emphasis is placed on the APB energy and its role in conferring static strength in these materials. The Chapter is structured in the following way. First, the experimental and theoretical evidence for the magnitude of the APB energy is considered. Next, the dependence of the APB energy on changes

in chemistry of $Ni_3(Al, Ti, Ta)$ is quantified, using methods based upon computational thermodynamics and electron structure calculations. Finally, models for the yield stress which contain a composition-dependent APB energy are considered. These are used to rationalise the role played by the composition-dependence of the APB energy in conferring strength.

4.2 Background

In Ni-based superalloys, precipitates of the ordered $L1_2$ phase (γ') reside within a coherent f.c.c. matrix, commonly referred to as the γ phase. The dislocations in γ have a Burgers vector of $a/2[1\bar{1}0]$ on the $\{111\}$ plane, but this is not a full dislocation in the γ' phase. Two dislocations with Burgers vector $a/2[1\bar{1}0]$, or superlattice partial dislocations, are required to generate a full dislocation within the precipitate. In practice, a superlattice partial dislocation can enter the γ' precipitates forming a planar fault called an anti-phase boundary (APB) – see Figure 4.1. Depending on the plane the superlattice partial dislocation resides on either $\{111\}$ or $\{001\}$, with the order imposed by the $L1_2$ crystal structure being locally overcome by forcing undesirable first (in the case of $\{111\}$ planes) or second (in the case of $\{001\}$ planes) neighbour bonds. A trailing superlattice partial dislocation is then able to restore the ordered $L1_2$ structure.

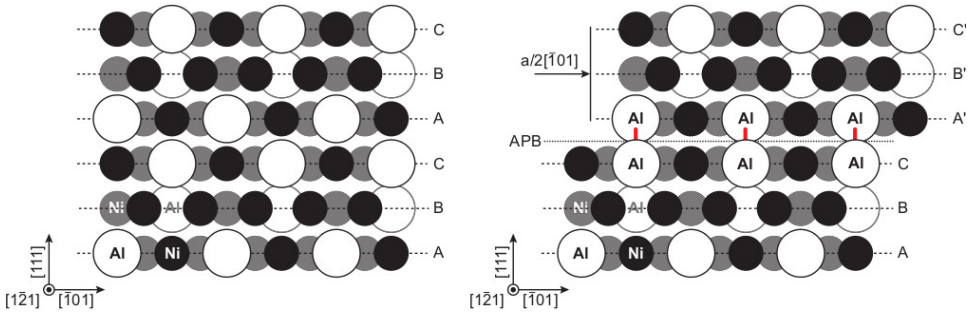


Figure 4.1: Illustration showing the formation of an APB on the {111} plane, in the γ' phase.

Early approximations of the APB energy for the $L1_2$ phase appealed to an Ising model. In this approach the energy is determined by relating changes in internal energy – approximated from thermodynamic values – to the interaction of atom pairs at the planar defect. Flinn [105] proposed a model to calculate APB energy in superlattices based on atomic interactions. Applying this model to the $L1_2$ crystal structure yields the following equation

$$\Delta E_{\mathrm{APB}} = \frac{2\phi h}{a^2\sqrt{h^2+k^2+l^2}} \tag{4.2}$$

where h, k and l are the Miller indices of the plane the superlattice partial dislocation resides on, and $\phi = \Omega_{\mathrm{AB}} - 1/2(\Omega_{\mathrm{AA}} + \Omega_{\mathrm{BB}})$ is the ordering energy, with Ω_{AB}, Ω_{AA} and Ω_{BB} representing the interaction energies of the A–B, A–A and B–B bonds, respectively. A number of ordered structures, including Ni_3Al, exhibit a proportional relationship between the ordering energy and the disorder-order transition temperature, T_{ord}, consistent with

$$\phi = kT_{\mathrm{ord}}/w \tag{4.3}$$

where k is the Boltzmann constant and w is a constant determined by the crystallo-

graphic structure and model applied. For $L1_2$ alloys w can vary between 0.82 [106], 1.0 [107] and 1.5 [108]. Figure 4.2, taken from [109], shows that Flinn's model gives a reasonable approximation of experimentally determined values for the APB on the {111} plane for a number of $L1_2$ alloys; the plotted lines have been determined using Equations 4.2 and 4.3.

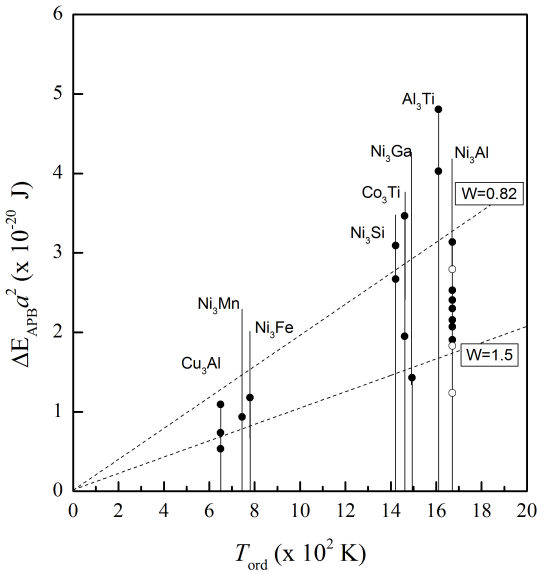


Figure 4.2: The APB energies on the {111} plane for $L1_2$ alloys plotted against the disorder-order transition temperature. Full circles represent TEM measurement and open circles represent atomistic calculations. The straight lines are APB energies determined from the nearest neighbour interaction with ordering energies derived from T_c using $w = 0.82$ and $w = 1.5$ [109].

The APB energy can be determined experimentally by using transmission electron microscopy (TEM) to measure the distance between superlattice partial dislocation pairs in the γ' phase [18,20–22,110–121]. Repulsive forces exist between dislocations due to their associated strain fields, which decrease as separation between the dislocations increases. However, as the separation gets larger, the surface area of the APB and the energy associated with this fault acts to bring the partial dislocations together. Assuming elastic isotropy, the forces acting on the partial dislocations can be balanced to find their equilibrium separation. The APB energy and the separation distance of

partial dislocations, d, are related using

$$\Delta E_{\mathrm{APB}} = \frac{\alpha \mu b^2}{2\pi d} \tag{4.4}$$

where α is dependent on the dislocation character, μ is the shear modulus and b is the Burgers vector [122]. In practice the measurements made using TEM methods may significantly deviate from actual APB energies. The most significant source of error arises from misrepresentation of separation distances in TEM images. Image correction methods have been developed in order to determine true separation from TEM observations. Cockayne, Ray and Whelan [123] derived an isotropic correction for observations under weak beam conditions. Corrections have been further improved using image simulations – that provide an anisotropic Cockayne-like correction – to determine dislocation separation [22].

The APB energy in binary Ni_3Al has been studied extensively using TEM experiments [22,110–115]; this work has been predominantly focused on Ni and Al rich compositions. Douin and Veyssiere [113] showed that APB energy on {100} is increased by excess Al and lowered by excess Ni. Dimiduk et al. [111] also observed that excess Ni reduces the APB energy on {100}; they concluded that APB energy on the {111} was increased by excess Al. Comparing the results for a number of studies of the Ni-Al system it appears that a weak correlation between Al content in Ni_3Al and APB energy on {111} exists, Figure 4.3.

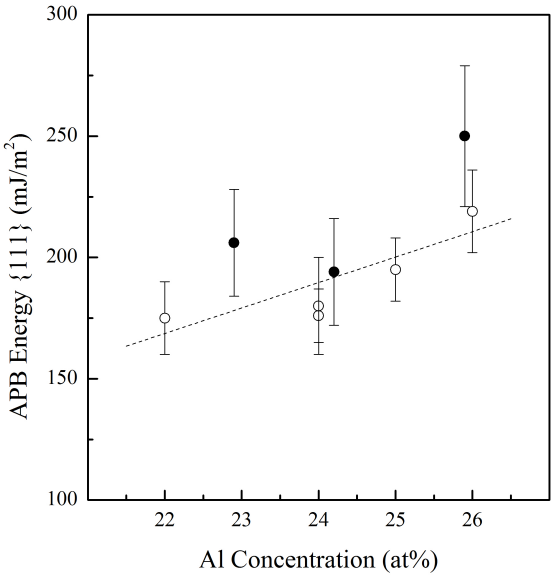


Figure 4.3: Review of literature values for variation of APB energy in binary Ni_3Al with Al content: full circles Cockayne corrected values, open circles image simulations.

The effect of ternary elements – Ti [20, 21], Ta [18, 19], V [111], Sn [111], Pb [120], B [22, 116], Hf [117–119] – on APB energy are summarised in Table 4.1. Dimiduk et al. [111] conducted an extensive study to determine whether 'effective' Al concentration or ternary additions were responsible for changes in APB energy. It was found that while Sn additions increase only slightly the APB energy on {111}, small V additions cause increases in APB energy on {111} that can only have been created due to the ternary element [111]. Baluc et al. observed dislocations in Ni-24.7Al-1Ta, concluding that Ta increased APB energy on both {111} and {100}. Korner [20] found that Ti additions significantly increased the APB energy. This is agreement with observations by Kawabata et al. [21], who studied Ni-15Al-10Ti using high resolution TEM techniques. A value of 560 mJ/m^2 was calculated using isotropic theory; application of anisotropic theory lowered the measured value to 353 mJ/m^2.

Table 4.1: APB energies measured using weak beam TEM methods (in mJ/m^2). TEM measurements have been corrected using: Cockayne correction methods (c), Image simulations (s).

Composition	$APB_{(111)}$	Corrected $APB_{(111)}$	$APB_{(100)}$	Reference
Ni - 22Al	-	175±15(S)	104±15	[110]
Ni - 22.9Al	169±22	206±22(C)	104±11	[111]
Ni - 22.9Al (Annealed 1h 700^0C)	123±21	140±21(C)	92±10	[111]
Ni - 24Al	-	176±11(S)	135±18	[112]
Ni - 24Al	147±15	180±20(S)	-	[22]
Ni - 24.2Al	163±22	194±22(C)	122±12	[111]
Ni - 24.4Al	-	-	75±25	[113]
Ni - 25Al	180±30	-	140±14	[114]
Ni - 25Al	-	195±13(S)	160±20	[112]
Ni - 25.5Al	-	-	90±5	[113]
Ni - 25.5Al	111±15	-	90±5	[115]
Ni - 25.9Al	-	-	120±20	[113]
Ni - 25.9Al	190±29	250±29(C)	170±25	[111]
Ni - 26Al	-	219±17(S)	184±16	[112]
Ni - 24.1Al - 0.9Sn	166±22	201±22(C)	129±13	[111]
Ni - 21.1Al - 3.7Sn	174±27	215±27(C)	146±18	[111]
Ni - 23.4Al - 1.0V	192±31	254±31(C)	155±19	[111]
Ni - 20.8Al - 4.0V	198±37	276±37(C)	201±36	[111]
Ni - 24.7Al - 1.0Ta	190±20	250±30(C), 237±30(S)	225±25	[18, 19]
Ni - 17.4Al - 6.16Ti	250±31	-	250±30	[20]
Ni - 15Al - 10Ti	561* (353**)	-	560* (353**)	[21]
Ni - 23.8Al 0.7B	153±10	173±15(S)	-	[22]
Ni - 22.8Al - 1B	-	170±20(S)	110±25	[116]
Ni - 24.8Al - 1B	-	210±20(S)	135±25	[116]
Ni - 24Al - 0.25Hf	160	-	120	[117]
Ni - 24Al - 1.5Hf	185	-	150	[118]
Ni - 24Al - 2Hf	190	-	170	[117]
Ni - 22Al - 3Hf	-	300±25(S)	250±25	[119]
Ni - 23.5Al - 2Pd	144±20	-	102±11	[120]
Ni - 19Al - 4.2Ti - 2.1Cr - 8.3Co - 0.5Mo	280±28	-	-	[121]
Ni- 10.4Al - 13.3Ti - 3.2Fe - 1Cr	350±20	-	-	[121]

*Measurement made using high resolution TEM methods.
**APB energy has been calculated using non isotropic theory.

The APB energy may also be deduced from tensile testing experiments, using models based on strengthening theory. Baither et al. [121] compared APB energies measured using TEM with values determined in this way. Good agreement between both techniques was observed. Baither et al. concluded that there was strong correlation between Ti/Al ratio and APB energy, supporting the work of Kroner [20] and Kawabata et al. [21]. Guo and Ma conducted similar tensile testing experiments on Ni-Cr-Al-Ti-Nb alloys [23]. In these experiments the effect of Nb additions on APB energy was

evaluated by correlating tensile test results with the Nb content in the γ' phase. Results showed that APB energy increased approximately 22 mJ/m^2 per at.% of Nb added to the γ' phase.

Computational modelling has also been employed to calculate the APB energy for Ni_3Al. The methods include: embedded atom method (EAM) [124–126], full potential linear augmented wave (FPLAWP) [127], linear muffin-tin orbitals (LMTO) [128], and the density functional theory [129–134]. Table 4.2 summarises the values for APB energy determined using the different calculation methods.

Table 4.2: A summary of APB energies calculated for Ni_3Al (in mJ/m^2).

Composition	Method	$APB_{(111)}$	$APB_{(100)}$	Reference
Ni_3Al	Ab-initio	188	-	[129]
Ni_3Al	Ab-initio	210	-	[130]
Ni_3Al	Ab-initio	172	-	[131]
Ni_3Al	Ab-initio	152	58	[133]
Ni_3Al	Ab-initio	181	104	[134]
Ni_3Al	Ab-initio	170	-	[132]
Ni_3Al	EAM	96	28	[124]
Ni_3Al	EAM	252	80	[125]
Ni_3Al	EAM	142	83	[126]
Ni_3Al	FP LPAW	175	140	[127]
Ni_3Al	LMTO	240	137	[128]

The density functional theory calculations indicate that the APB energy is approximately 170 mJ/m^2 for Ni_3Al on the {111} plane, showing good agreement with findings from TEM experiments (195 mJ/m^2). The use of ab-initio modelling methods to evaluate the APB energy for ternary or multi-component γ' compositions remains limited. Chandran and Sondhi [134] recently calculated APB energies for ternary systems using density functional theory (DFT). This was made possible by comparing the total energy of the structure that contains the planar fault, E_{APB}, with that of a perfect crystal, E_0, according to

$$\Delta E_{\mathrm{APB}} = \frac{E_{\mathrm{APB}} - E_0}{A} \tag{4.5}$$

where A is the area of the APB in the faulted structure. This approach renders the APB energy at 0 K, and excludes the effect of electronic, vibrational and configurational entropy. For the ternary systems, E_{APB} and E_0 were determined by averaging over several calculations with different atomic configurations. Figure 4.4a shows the expected effect of ternary additions on the APB energy. Chandran and Sondhi concluded that Ta, Ti and Nb increase the APB energy. Vamsi and Karthikeyan [133] extended the DFT approach to consider the effect of stoichiometry on the APB energy of Ni_3Al and $Ni_3(Al, X)$, where X = Ta, Ti. In this work they found the APB energy of Ni_3Al to be 152 mJ/m^2, and observed that Ni-rich compositions result in a lower APB energy, see Figure 4.4b. Both studies report that Ta has the greatest effect in APB energy; however, Vamsi and Karthikeyan predict alloying has a much stronger effect on APB. There is also a disagreement between the point at which maximum APB energy is achieved in these ternary systems.

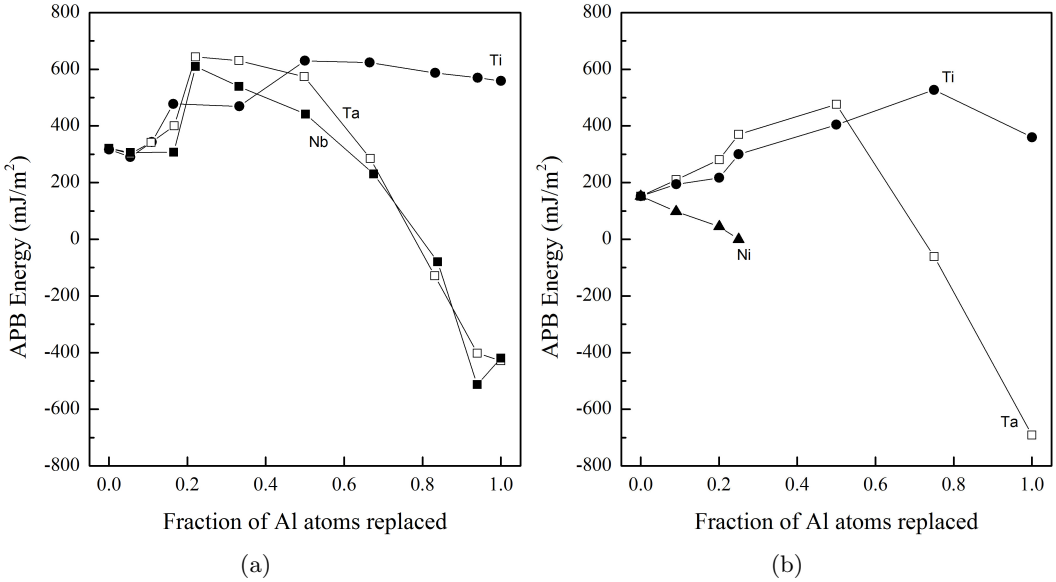


Figure 4.4: Computer estimates of APB energies in $Ni_3(Al, X)$ using DFT methods, Chandran and Sondhi [134], Vasmi and Karthikenyan [133].

In order to design future high strength nickel-based superalloys, the selection of alloy chemistries for which γ' has a high APB energy seems sensible. Significant challenges remain when trying to determine the effect of chemistry on APB energy using direct measurement or ab-initio methods. Both approaches require significant efforts and have severe limitations. Direct measurement requires complex sample preparation and microscopy techniques. The DFT approach at present is limited to ternary systems. This work describes a CALPHAD approach for rapid calculation of the APB energy. Thus, application of this method for the optimisation of future high-strength polycrystalline Ni-based superalloys becomes possible, as will be demonstrated.

4.3 Modelling Approach

The CALPHAD method for calculating the APB energy using a thermodynamic database is described in Section 4.3.1. The DFT calculations performed as part of this work are

described in Section 4.3.2; these were used to validate the thermodynamic database. It is necessary to validate the thermodynamic database – which is empirically based – using ab-initio calculations to ensure reasonable agreement between both methods in regions where the CALPHAD may rely on a high degree of interpolation or possibly even extrapolation, i.e. determination of enthalpy of mixing for metastable phases which cannot be readily evaluated through experiments. The final part of this section describes how the calculation for APB energy can be used to rank the yield strength of nickel-based superalloys based only on alloy chemistry.

4.3.1 Calculation of the APB energy using the CALPHAD Approach

An Ising model was used determine the APB energy assuming the available thermodynamic data. Inden [135] showed that for f.c.c. alloys with long range ordering at least second nearest neighbour (NN) interactions must be considered to relate interchange energies and thermodynamic data. For transition metals, accuracy can be further improved by considering higher order interactions [136, 137]. Hence, the model proposed by Inden et al. [138] which considers up to fourth NN interactions has been used in this work. The APB energies on {111} and {100} – $\Delta E_{\mathrm{APB}(111)}$ and $\Delta E_{\mathrm{APB}(100)}$ respectively – are assumed to be given by

$$\Delta E_{\mathrm{APB}(111)} = 3^{-0.5}\,(2a)^{-2}\left[\left(\xi^{\mathrm{I}}-\xi^{\mathrm{II}}\right)^2+\left(\xi^{\mathrm{III}}-\xi^{\mathrm{IV}}\right)^2\right]\times\left(V^{(1)}-3V^{(2)}+4V^{(3)}-6V^{(4)}\right) \tag{4.6a}$$

$$\Delta E_{\mathrm{APB}(100)} = (2a)^{-2}\left[\left(\xi^{\mathrm{I}}-\xi^{\mathrm{III}}\right)^2+\left(\xi^{\mathrm{II}}-\xi^{\mathrm{IV}}\right)^2\right]\times\left(-V^{(2)}+4V^{(3)}-4V^{(4)}\right) \tag{4.6b}$$

where ξ^{I}, ξ^{II}, ξ^{III}, and ξ^{IV} are mean correlation functions which describe site occupation of the lattice sites (I-IV). In the case of a perfectly ordered $\mathrm{L1_2}$ crystal structure,

$\xi^{\mathrm{I}} = -1$ and $\xi^{\mathrm{II}} = \xi^{\mathrm{III}} = \xi^{\mathrm{IV}} = 1$. The energy for first, second, third and fourth NN interactions are accounted for by the terms $V^{(1)}, V^{(2)}, V^{(3)}$ and $V^{(4)}$, respectively. Here, up to third NN interactions have been considered, i.e. it is assumed that $V^{(4)} = 0$.

Thus in Equation 4.6 there are three unknown quantities: $V^{(1)}, V^{(2)}$ and $V^{(3)}$. These energies are determined by using: (i) the ordering energy for the $\mathrm{L1_2}$ phase ($\Delta H_{\mathrm{ord}}^{\mathrm{L1_2}}$), (ii) the enthalpy of mixing for the disordered f.c.c. phase ($\Delta H_{\mathrm{mix}}^{\mathrm{FCC}}$) and (iii) the ordering temperature of the γ' phase (T_{ord}). The relationships between these values are defined according to

$$\Delta H_{\mathrm{mix}}^{\mathrm{FCC}} = -N_{\mathrm{A}} x_s (1 - x_s) \left[6V^{(1)} + 3V^{(2)} + 12V^{(3)} \right] \tag{4.7a}$$

$$\Delta H_{\mathrm{ord}}^{\mathrm{L1_2}} = -N_{\mathrm{A}} x_s^2 \left[6V^{(1)} - 9V^{(2)} + 12V^{(3)} \right] \tag{4.7b}$$

$$T_{\mathrm{ord}} = x_{\mathrm{sro}} N_{\mathrm{A}} x_s (1 - x_s) \left[4V^{(1)} - 6V^{(2)} + 8V^{(3)} \right] \tag{4.7c}$$

where x_s is the concentration of solute atoms in the γ' phase (cobalt has not been considered as a solute atom and is treated as nickel in all further calculations), N_{A} is Avogadro's number and x_{sro} is a short range ordering parameter. It is not possible to produce a direct solution for $V^{(1)}$, $V^{(2)}$ and $V^{(3)}$, since they are not independent. Therefore, it is necessary to introduce an 'effective' interchange energy, $V_{\mathrm{eff.}}^{(1,3)} = V^{(1)} + 2V^{(3)}$. Miodownik and Saunders [139] proposed that there is a constant ratio between the first and third NN interchange energies, consistent with $V^{(3)}/V^{(1)} = 0.125$. This assumption is based on first principle calculations conducted by Sluiter [140], Table 4.3.

Table 4.3: First principle calculations for interchange energies considering up to 4th nearest neighbour interactions, given in k (1.38×10^{-23} $\mathrm{JK^{-1}}$) units.

Compound	$W^{(1)}$	$W^{(2)}$	$W^{(3)}$	$W^{(4)}$	$W^{(3)}/W^{(1)}$	Reference
Ni_3Al	2139	-114	256	-144	0.12	[140]
Ni_3Ti	2117	-364	300	41	0.14	[140]

Substitution of $V_{\text{eff.}}^{(1,3)}$ into Equations 4.7a and 4.7b makes it possible to determine the interchange energies according to

$$V_{\text{eff.}}^{(1,3)} = -\left(3\Delta H_{\text{mix}}^{\text{FCC}} + \Delta H_{\text{ord}}^{\text{L1}_2}(1-x_s)/x_s\right)/24N_{\text{A}}x_s(1-x_s) \tag{4.8a}$$

$$V^{(1)} = 0.8W_{\text{eff.}}^{(1,3)} \tag{4.8b}$$

$$V^{(2)} = \left(H_{\text{ord}}^{\text{L1}_2}(1-x_s) - \Delta H_{\text{mix}}^{\text{FCC}}x_s\right)/12N_{\text{A}}x_s^2(1-x_s) \tag{4.8c}$$

$$V^{(3)} = 0.125V^{(1)} \tag{4.8d}$$

Equations 4.6 - 4.8 can be used to calculate the APB energy using CALPHAD modelling. A flowchart outlining the process for doing this is given in Figure 4.5. One begins by defining the state variables for the CALPHAD calculation, i.e. temperature, alloy chemistry. The chemistry of the γ' phase is determined by finding the two phase (γ/γ') equilibrium. At this point two separate routines must be implemented.

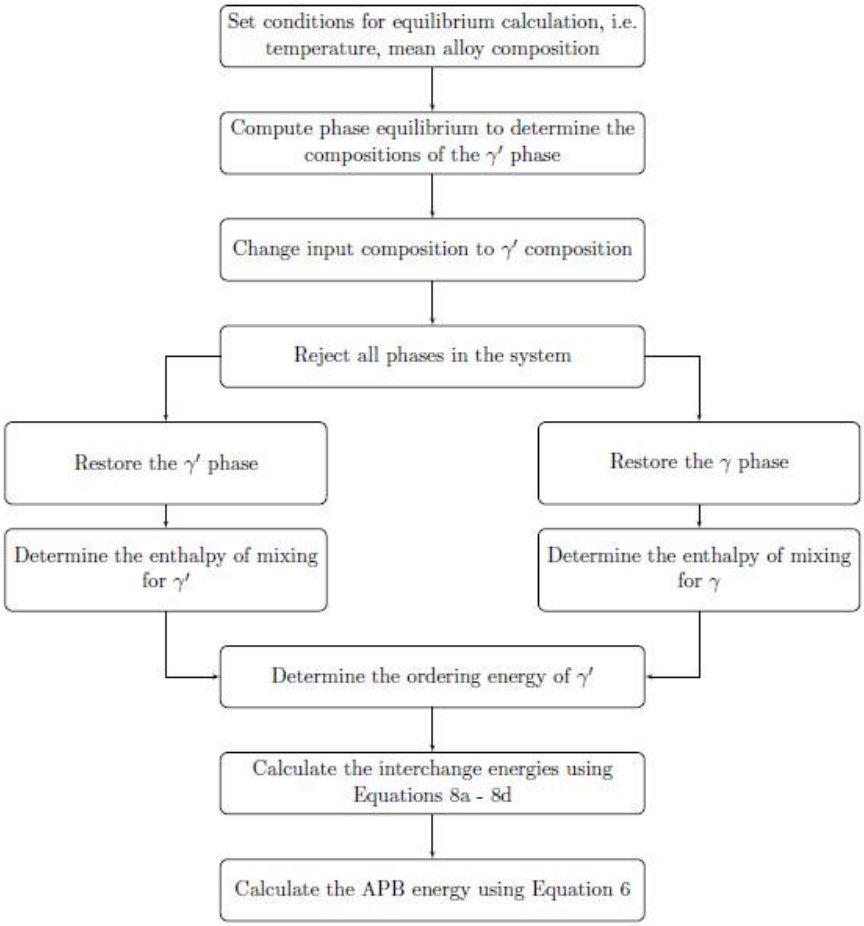


Figure 4.5: Flow chart outline the process for modelling the APB energy in Ni-based superalloys.

A first routine is required to calculate the enthalpy of mixing for the γ' composition in the $L1_2$ configuration ($\Delta H_{\text{mix}}^{L1_2}$). In this instance only the $L1_2$ phase is included in the thermodynamic database. A second, separate routine is required to calculate the enthalpy of mixing for the disordered f.c.c. configuration. Therefore, only the disordered f.c.c. phase is included. The Gibbs free energy curve for the disordered f.c.c. phase has been determined empirically. It is expected that some short range ordering (SRO) has been captured within the thermodynamic description for the phase. Equation 4.7a assumes no SRO. Therefore, the calculated enthalpy of mixing must be

corrected for SRO, Miodownik and Saunders [139] proposed a 10% increase to $\Delta H_{\text{mix}}^{\text{FCC}}$ obtained from the database. Using these two values it is possible to determine the ordering energy of the γ' phase, consistent with

$$\Delta H_{\text{ord}}^{\text{L1}_2} = \Delta H_{\text{mix}}^{\text{L1}_2} - \Delta H_{\text{mix}}^{\text{FCC}} \tag{4.9}$$

Table 4.4 shows the value for $\Delta H_{\text{ord}}^{\text{L1}_2}$ before and after the SRO correction was applied to the $\Delta H_{\text{mix}}^{\text{FCC}}$ determined using the TTNi7 database. Applying the SRO correction results in much better agreement with experimental data for Ni_3Al where SRO has been inhibited by mechanical alloying [141] and vapour deposition [142]. The ordering energy also correlates with values determined using ab-initio calculations [143].

Table 4.4: The ordering energy calculated using the TTNi7 database compared with: ab-initio calculations, experimentally measured values.

Method	Ordering Energy	Reference
TTNi7 Database	-6.6 kJ/mol	This work
TTNi7 Database (Corrected for SRO)	-9.9 kJ/mol	This work
Mechanical alloying	-8.0 kJ/mol	[141]
Vapor deposition at room temperature	-7.0 kJmol	[142]
Vapor deposition at -186°C	-9.0 kJ/mol	[142]
Full Potential Theory	-10.7 kJ/mol	[143]
Density Functional Theory	-11.8 kJ/mol	This work

In the results section the APB energy for ternary alloys has been calculated using the CALPHAD approach. For all the Ni-25Al-X alloys – where X= Ti, Ta, Nb, Mo, W, Cr – the Al atoms have been directly substituted with the ternary element so that the sum of solute atoms remains at 25 $at\%$.

4.3.2 DFT approach

Using DFT, the enthalpy of formation of $A_3B - L1_2$ compounds can be compared to the enthalpy of formation of A_3B – f.c.c. random solid solution to get an ordering enthalpy which is proportional to the ordering enthalpy obtained from the CALPHAD database. But calculation of the enthalpy of formation of a random compound in DFT is not trivial due to the presence of periodic boundary conditions. This problem has been resolved by the use of Special Quasi-random Structures (SQSs) [144, 145], special periodic supercells which emulate a random solid solution.

Using the ATAT code [146], several SQSs were obtained for $A_{.75}B_{.25}$ (f.c.c.), $A_{.75}B_{.125}C_{.125}$ (f.c.c.) and $A_3B_{.5}C_{.5}$ ($L1_2$). The total energies of these SQSs, as well as the simple ordered $A_3B - L1_2$, were calculated for the $Ni_3(Al, Ti)$, Ni3(Al, Ta), $Ni_3(Al, Nb)$, $Ni_3(Al, W)$, $Ni_3(Al, Mo)$ and $Ni_3(Al, Cr)$ systems using the Vienna Ab-initio Simulation Package (VASP) [147, 148]. The Projector Augmented Wave (PAW) method [149, 150] was used to describe the electron-ion interactions and the spin-polarised Generalised Gradient Approximation parameterised by Perdew et al [151] was adopted throughout the study. Plane waves were included up to 320 eV and the Monkhorst-Pack scheme was used to define the k-points grid, with a k-points density higher than 10^5 k-points/Å^{-3}. The self-consistent loops were stopped after the change in total energy fell below 10^{-5} eV, while structure relaxations were deemed converged when the ionic forces fell below 10^{-3} eV/Å.

To calculate the enthalpy of formation for these compounds, VASP was used to determine the energy of the pure elements in their reference state. We expect that the DFT calculations will show good qualitative agreement with the CALPHAD data, and strengthen our claim that a reliable CALPHAD database can be used to evaluate how the APB energies change with chemistry. It is important to note, however, that database validation is necessary, should this methodology be used to calculate APB

energies in other systems.

4.3.3 Modelling the Yield Strength for Alloy Design Purposes

The expressions for precipitate strengthening given in Equations 4.1a and 4.1b require detailed information regarding the size and distribution of the precipitate phase. Reppich [24] proposed that the critical radius for maximum precipitate strength can be found by taking the derivative of the Equation 4.1b – describing hardening due to strongly coupled partial dislocations – with respect to r. This results in the following approximation for maximum precipitate strength,

$$\sigma_{y_{\text{peak}}} = \overline{M} \,.\, \frac{1}{2} \Delta E_{\text{APB}} f^{1/2} / b \tag{4.10}$$

where $\overline{M}$ is the Taylor factor. Reppich confirmed this through experimental testing [35, 36] showing that the peak arises at the point where the transition between weakly and strongly coupled partial dislocations occurs. This simplified model for precipitate strengthening has been used for the purposes of alloy design, thus allowing alloy chemistry to be optimised for improved yield strength. For the results presented in this work the volume fraction of γ', f, has been calculated using a two phase (γ/γ') equilibrium at 650 °C.

4.4 Results

The results section is divided into three. The first section compares the enthalpy of mixing – in ternary Ni-Al-X alloys with both the $L1_2$ and f.c.c. configuration – calculated using the thermodynamic database and ab-initio methods. Following this, the APB energy for Ni-Al-X alloys with the $L1_2$ crystal structure is considered. The final section

focuses on the application of the model for APB energy within the context of designing high strength polycrystalline nickel-based superalloys for turbine disc applications.

4.4.1 Comparing the Enthalpy of Mixing from CALPHAD and DFT Calculations

Figures 4.6 - 4.7 show the percentage change in enthalpy of mixing for Ni-25Al when ternary elements are substituted for Al. This allows for a direct comparison between the CALPHAD and DFT calculations. In the $L1_2$ configuration the enthalpy of mixing for Ni-25Al is calculated to be $-39.6\,\mathrm{kJ/mol}$ at 650 °C using the CALPHAD method and $-42.01\,\mathrm{kJ/mol}$ at 0 K using the DFT approach. The enthalpy of mixing for Ni-25Al in the f.c.c. configuration is calculated to be $-29.72\,\mathrm{kJ/mol}$ using the CALPHAD method and $-30.22\,\mathrm{kJ/mol}$ using the DFT approach.

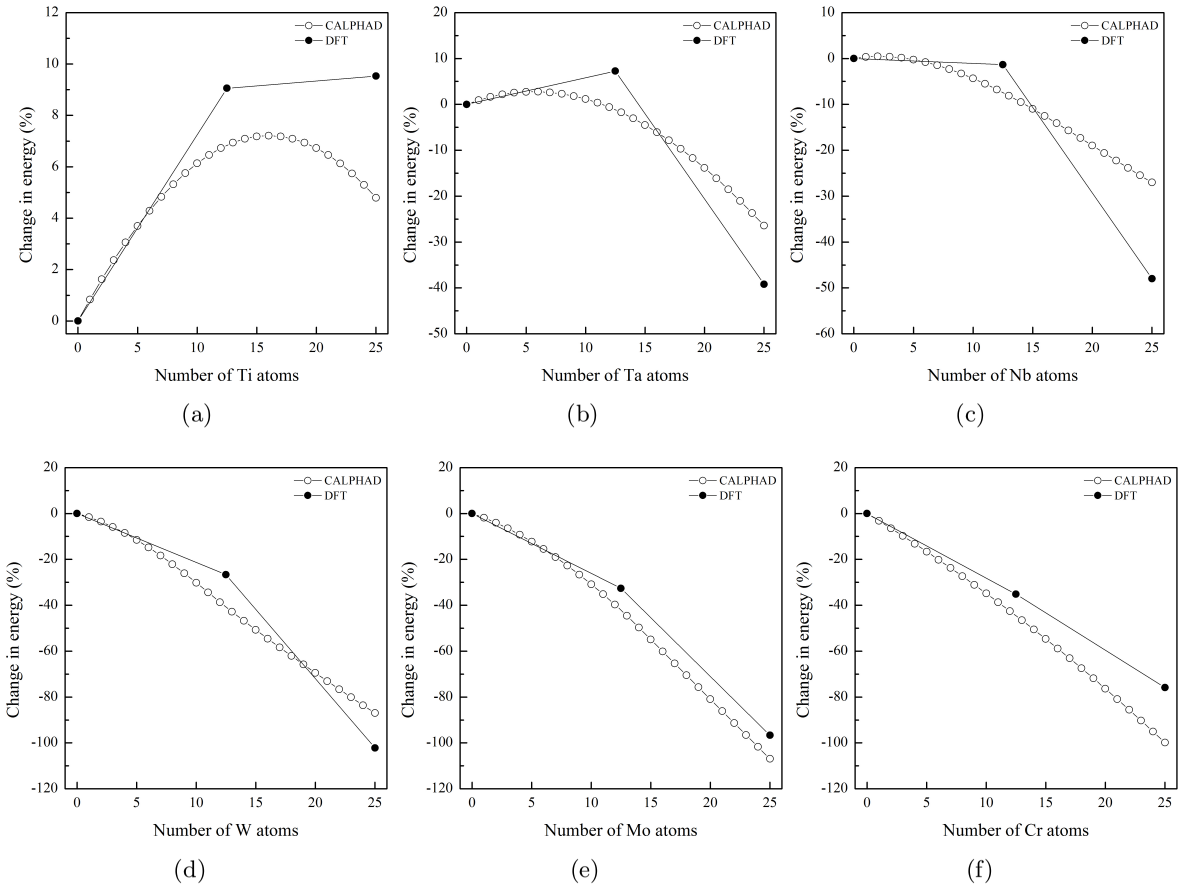


Figure 4.6: A comparison of enthalpy of mixing calculated using CALPHAD and DFT for the $L1_2$ phase when (a) Ti, (b) Ta, (c) Nb, (d) W, (e) Mo and (f) Cr are substituted for Al atoms. Changes in energy have been normalised to the value for Ni_3Al to allow for comparison between methods.

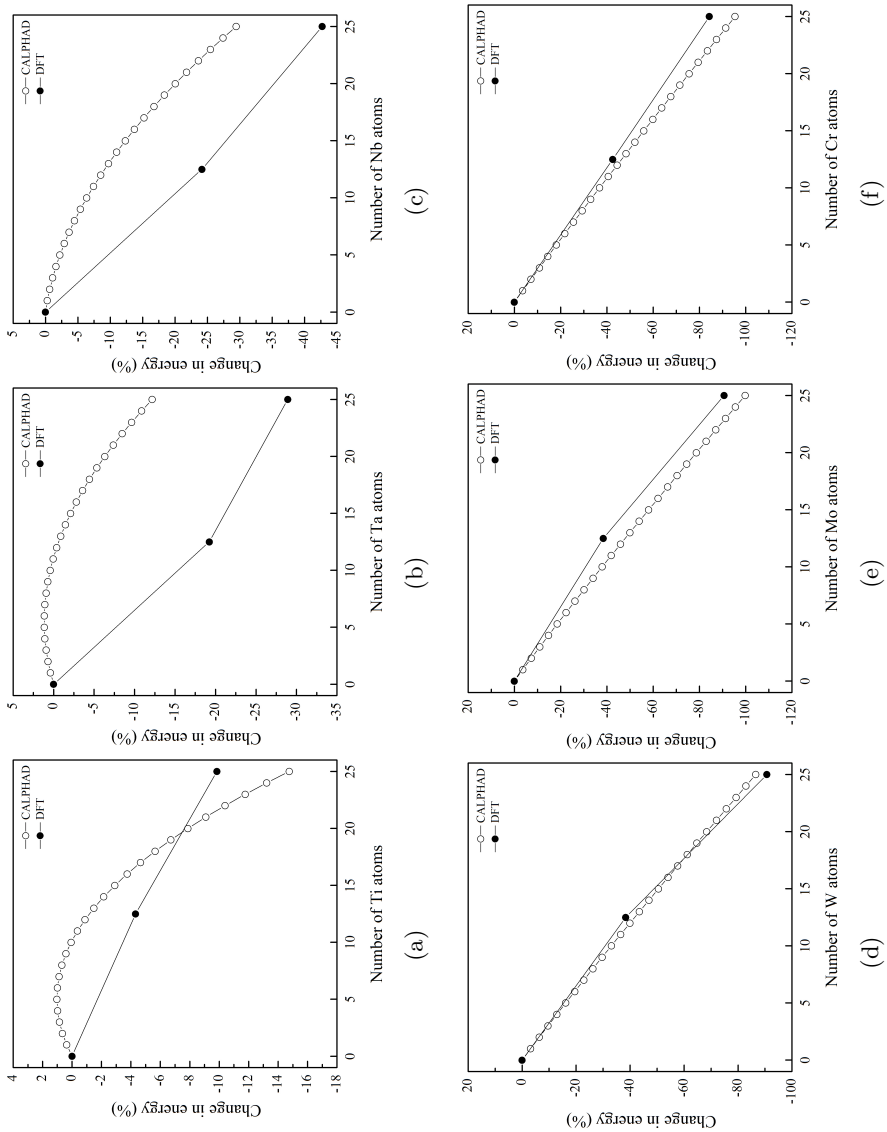


Figure 4.7: A comparison of enthalpy of mixing calculated using CALPHAD and DFT for the f.c.c. phase when (a) Ti, (b) Ta, (c) Nb, (d) W, (e) Mo and (f) Cr are substituted for Al atoms. Changes in energy have been normalised to the value for Ni_3Al to allow for comparison between methods.

In the $L1_2$ configuration good agreement between CALPHAD and DFT is observed for all ternary systems. At the composition Ni-12.5Al-12.5X the discrepency for Ti, Ta and Nb is less than 7%; for Cr and Mo less than approximately 10%. The largest disagreement at this composition is for W, approximately 20%. Once all the Al has been replaced with the ternary element, the disagreement between CALPHAD and DFT calculations increases further. The largest variation at this composition – a difference of 25% – is observed for Cr.

For the f.c.c. configuration both CALPHAD and DFT find similar trends for the change in energy when Al is replaced with ternary elements. For alloys where 50% of Al atoms are replaced with ternary additions, strong correlation between both methods is observed for Ti, Cr, Mo and W, with differences of less than 10%. The most significant disagreement is shown for Ta and Nb; the difference between results is around 20-25% at the composition Ni-12.5Al-12.5X.

4.4.2 APB Energies in Ni-Al-X Alloys

The APB energy of Ni_3Al calculated using CALPHAD (at 650 °C) and DFT was 232 mJ/m^2 and 310 mJ/m^2, respectively. The values determined from both CALPHAD and DFT are higher than APB energies measured experimentally, see Table 4.1.

Figure 4.8 shows the effect ternary additions have on the APB energy, predicted using both CALPHAD and DFT. The results for the CALPHAD method are in good agreement with APB energies measured experimentally for Ni-Al-Ti [20, 21] and Ni-Al-Ta alloys [18, 19]. According to CALPHAD, Ti has the strongest influence on the APB energy. For low levels of alloying, up to 3 at.% for Ta and Nb, and up to 5 at.% for Mo and W, the APB energy increases in a manner similar to Ti. For additions of Ta, Nb, Mo and W, the APB energy reaches a maximum at 5 at.%; higher concentrations of these elements influence APB energy negatively. The only element which does not

produce any increase in the APB energy is Cr.

DFT calculations indicate that Ta has the strongest influence on increasing the APB energy, followed by Nb and Ti. For CALPHAD and DFT, the change in APB energy calculated for Ni-Al-Ti and Ni-Al-Cr alloys show very similar trends. Both modelling methods predict similar changes in APB energy for additions of Mo and W. The most evident disagreement between the two methods is for Ni-Al-Ta and Ni-Al-Nb.

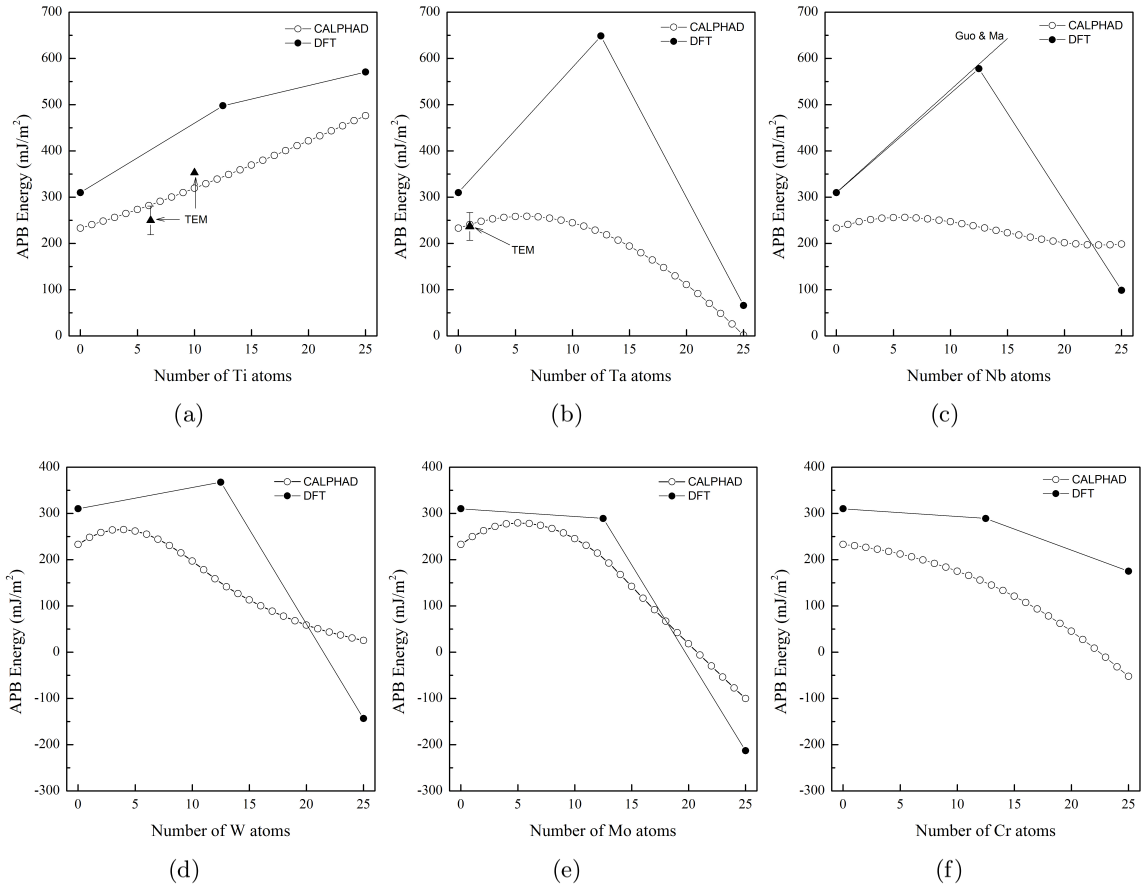


Figure 4.8: The change in APB energy on the {111} plane when (a) Ti, (b) Ta, (c) Nb, (d) W, (e) Mo and (f) Cr are substituted for Al in the γ' phase.

4.4.3 Application of CALPHAD method to multi-component alloys

The yield strength for a 42 different commercial/experimental polycrystalline nickel-based superalloys was taken from the literature [2, 59, 68, 70, 72, 75]. Equation 4.10 was used to calculate the precipitate strengthening in each alloy using only the mean chemical composition. To demonstrate the model's ability to rank the yield strength of multi-component nickel-based superalloys, the calculated precipitate strengthening has been compared with the experimental data. Figure 4.9 shows the correlation between experimental data and calculated precipitate strengthening. A line with a slope equal to 1 has been fitted to the data; the correlation coefficient, R^2, was calculated to be 0.52. The line intercepts the y axis at a value of 307 MPa; this is a systematic over-prediction from the model. The correlation is deemed to be acceptable for the purposes of ranking new alloy chemistries. The effect assumptions may have on scatter is considered later within the Discussion section.

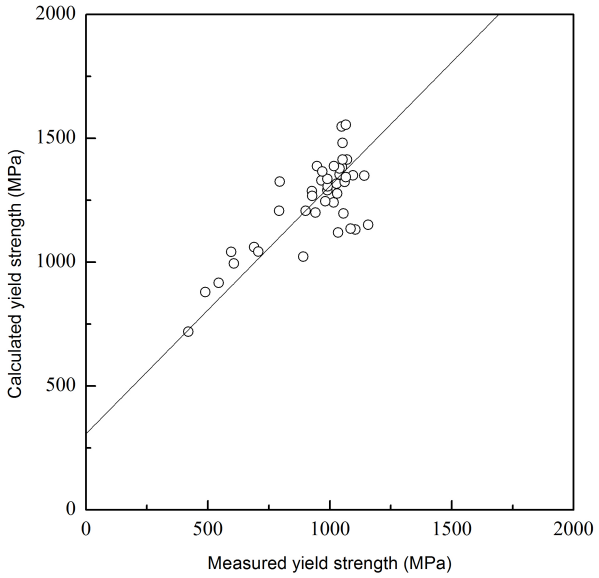


Figure 4.9: A comparison of measured yield strength values with calculated precipitate strengthening using the APB energy determined with the CALPHAD approach.

The motivation for developing a physically based model capable of ranking the the

yield strength of nickel-based superalloys was for the purpose of alloy design. Table 4.5 describes the alloy design space which was studied using the Alloys-by-Design concept developed by Reed et al. [1]. This particular compositional range has been considered previously for turbine disc applications [152], where high levels of strength are critical to material performance.

Table 4.5: Limits of the composition design space used in the present study.

Element	Min at.%	Max at.%
Cr	4	24
Co	2	22
Mo	0	4
W	0	2
Ta	0	2
Al	2	12
Ti	1	7
Zr	0.038	0.038
C	0.128	0.128
B	0.078	0.078

The contour plot shown in Figure 4.10 was constructed using Equation 4.10. This illustrates the relationship between APB energy, γ' volume fraction and precipitate strengthening. The contours show that at low volume fractions of γ', APB energy does not strongly influence precipitate strengthening; alternatively, if the volume fraction of γ' is high, precipitate strengthening is much more dependent on the APB energy. A number of common turbine disc alloys have been plotted on Figure 4.10 to illustrate possible changes that could be made to improve the tensile strength of turbine disc alloys. For the alloy space considered the APB energy is strongly dependent on Ti content in the alloy. Thus three different concentrations of Ti have been highlighted on the graph (1 at.%, 4 at.% and 7 at.%). Each level is predicted to create approximately a 200 MPa shift in yield strength contribution from the precipitate phase. The distribution of yield strength within the alloy design space highlights the possible latitude

for design, recognising that alloys with varied volume factions of γ' or chemistry may possess the same level of precipitate strengthening.

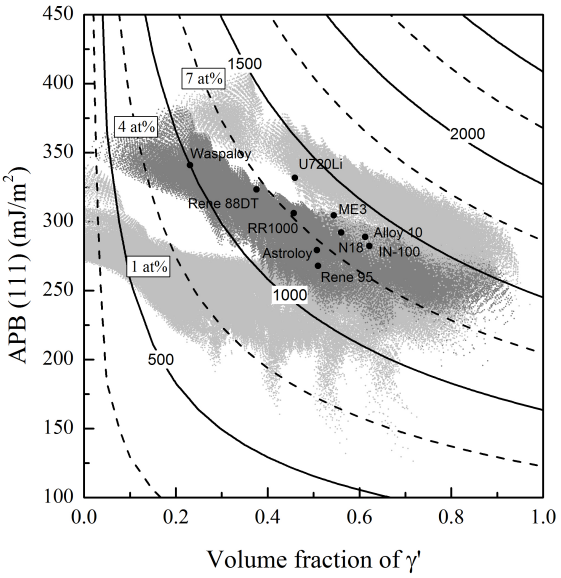


Figure 4.10: A contour plot showing how γ' volume fraction and APB energy affect precipitate strength. Clusters delineating specific levels of titanium in the alloy have been plotted.

4.5 Discussion

The results confirm that the composition-dependence of the APB can be accounted for in multi-component nickel-based superalloys. Furthermore, for a number of Ni-Al-X alloys, modelling predictions using CALPHAD have been shown to be broadly comparable with ab-initio calculations. The first section of the Discussion compares the APB energies determined using CALPHAD and DFT methods, with emphasis placed on some of the apparent limitations of the thermodynamic database used in this work. In Section 4.5.2 a model for calculating APB energy based upon the DFT calculations is proposed, improving the correlation of the precipitate strengthening model with experimental data. The final section considers the application of the precipitate strengthening

model in the context of designing high strength polycrystalline nickel-based superalloys.

4.5.1 Comparison of CALPHAD and DFT Calculation for APB Energies

The CALPHAD model for APB energy must consider meta-stable phases. To understand the accuracy of the thermodynamic database – particularly for meta-stable phases – selected alloys were compared with DFT calculations. For Ni-Al-X alloys – where X=Ti, W, Cr, Mo – good agreement was observed between CALPHAD and DFT methods. The most significant finding was that the enthalpy of mixing for Ni-Al-Ta and Ni-Al-Nb alloys in the f.c.c configuration varied greatly from DFT calculations. Hence, for these alloys systems, the APB energy determined using CALPHAD did not agree with more accurate ab-initio calculations. This is a major limitation of thermodynamic database used, as both Ta and Nb elements strongly partition to the γ' phase in nickel-based superalloys.

The APB energy of Ni_3Al was calculated to be $232\,mJ/m^2$ (at 650°C) and $310\,mJ/m^2$, for CALPHAD and DFT methods, respectively. Kruml et al. [112] measured the APB energy to be $195 \pm 13\,mJ/m^2$, using TEM methods corrected with image simulations. Overestimates for the APB energy may be explained by the assumption that in Equation 4.6 the APB is considered ideal with complete long range ordering (LRO), meaning different values would be required for the mean correlation functions which describe site occupation of the lattice sites. It is unlikely that complete LRO was present in the experimental specimens used for TEM studies, lowering the measured APB energy. The APB energy determined using the DFT method is 34% greater than the CALPHAD prediction. The DFT calculations are based on defect-free crystals; also, electronic, vibrational and configurational entropy effects are excluded. It is expected these effects may be contained implicitly within the thermodynamic database. These assumptions

rationalise why the enthalpy of mixing in the $L1_2$ configuration determined using DFT is much greater than the value determined using CALPHAD.

For the ternary systems studied CALPHAD and DFT estimate similar changes in the APB energy for Ni-Al-X alloys, where X=Ti, W, Cr, Mo. The relative change in APB energy correlates strongly for both methods for $Ni_3(Al, Ti)$, and these modelling results also agree with experimental measurements, Figure 4.8a. The DFT modelling shows that Ta and Nb have a very strong effect on APB energy; this differs from CALPHAD calculations. Experiments by Baluc et al. [18, 19] for $Ni_3(Al, Ta)$ show the Ta does strongly effect APB energy. The effect of Nb on APB energy has been determined by Guo and Ma [23], using tensile testing experiments. Guo and Ma found that the APB energy increases by $22\,mJ/m^2$ per at.% of Nb added to the γ' phase. The change in APB energy determined using DFT, when Nb has a positive influence on APB energy, is calculated to be $21.4\,mJ/m^2$ per at.% of Nb added. By comparing the modelling results from this work with the literature it is evident that using an Ising model combined with thermodynamic values is a suitable method for calculating the APB energy. However, there are deficiencies in the thermodynamic database, particularly when Ta or Nb are used as ternary additions; this effect must be accounted for if this technique to be fully exploited.

In the following section, DFT results have been used to produce an improved model for calculating the APB energy in multi-component nickel-based superalloys.

4.5.2 Improving APB modelling using DFT calculations

A model for the APB energy, based on DFT results, is now proposed to overcome the limitations of the thermodynamic database. It is assumed that the change in APB energy in multi-component nickel-based superalloys can be determined by linear superposition of the effect of individual elements. For each alloying element a linear

relationship – from the composition Ni-Al to Ni-12.5Al-12.5X – was assumed to determine the coefficient for change in APB energy, k_i, listed in Table 4.6.

Table 4.6: Coefficients for APB energy change determined from DFT work.

Element	Cr	Mo	W	Ta	Nb	Ti
k_i(mJ/m^2)	-1.7	-1.7	4.6	27.1	21.4	15.0

Considering that all the elements – with the exception of Cr and Ti – have a solubility limit below 12.5 at.% [17] it was assumed that this linear fit provides a reasonable approximation. Synergistic effects due to the presence of multiple solute elements are not considered. The model takes the form

$$\Delta E_{\mathrm{APB}} = \Delta E^0_{\mathrm{APB}} + \sum_{i=1}^{n} (k_i x_i) \tag{4.11}$$

where x_i is the concentration in at.% of the solute i in the γ' phase, n is the number of solute elements in the γ' phase, and $\Delta E^0_{\mathrm{APB}}$ is the APB energy for Ni_3Al measured by Kruml et al. [112].

The precipitate strengthening for commercial turbine disc alloys was calculated using this model and compared with experimental yield strength, Figure 4.11. A line with a slope of 1 was fitted to the data; the correlation coefficient, R^2, between modelling and experimental results was calculated to be 0.75. This represented an improvement in correlation in comparison to the CALPHAD model ($R^2 = 0.52$). The scatter observed of approximately 200 MPa may be explained by the fact that an idealised model is used to estimate the precipitate strengthening.

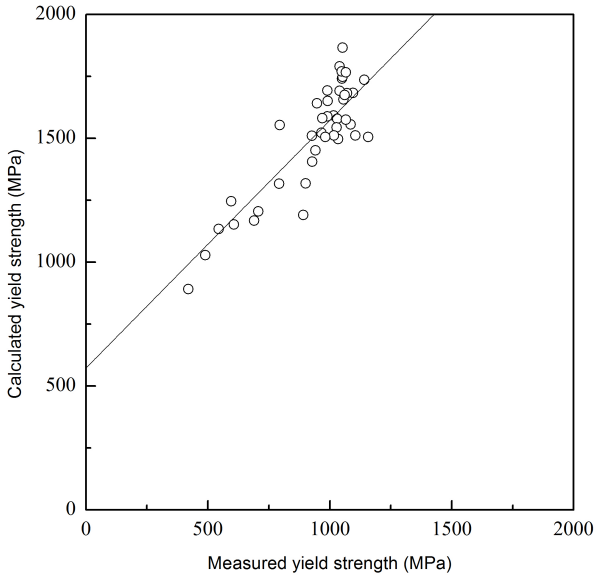


Figure 4.11: A comparison of measured yield strength values with calculated precipitate strengthening using the APB energy determined with the DFT approach.

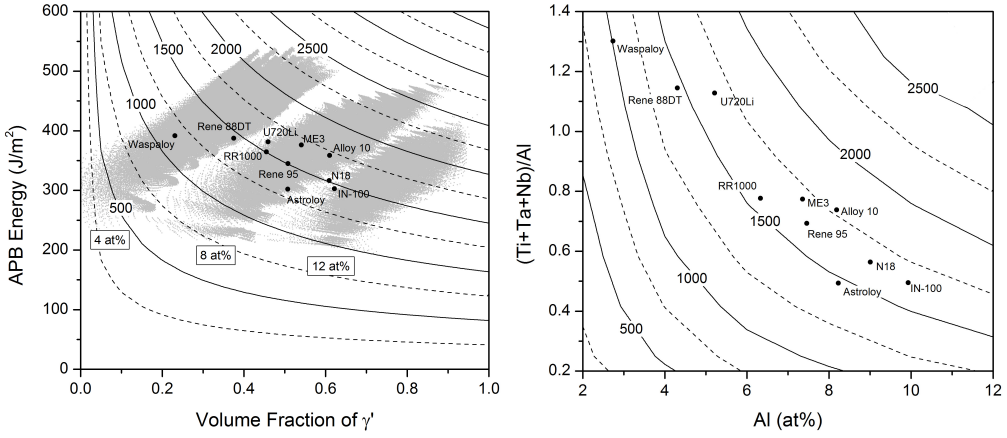
If the precipitate size and distribution for each alloy was characterised experimentally and precipitate strengthening was calculated using models for weak and strong dislocation shearing, it would be expected that this scatter would reduce. The systematic over prediction observed in Figure 4.11 is probably due to an over estimation of the APB energy based on the assumptions made in DFT modelling. Furthermore, the simple linear DFT model for calculating the APB energy in multi-component alloys disregards synergetic effects possibly arising from multiple solute additions. Work is ongoing to use the models presented in this work to accurately determine the yield strength of polycrystalline nickel-based superalloys where the microstructure and chemistry of the phases has been fully characterised, thus building on work reported elsewhere [34].

4.5.3 Relevance to alloy design

Kozar et al. [34] modelled the yield strength in the polycrystalline nickel-based superalloy IN100, showing that the majority of strengthening was gained from the γ' phase.

Using Equation 4.10 to estimate the maximum precipitate strengthening provides an insight into the factors which must be taken into account when designing a high strength turbine disc alloy. Consideration must be given to both the fraction of precipitate phase and APB energy, both of which are strongly affected by alloy chemistry.

In Figure 4.10 it is seen that for alloys with low volume fractions of γ', increasing the APB energy has very little effect on precipitate strengthening. However, at volume fractions of γ' greater than 20% APB energy strongly influences precipitate strengthening. Therefore, when developing new grades of superalloy it is necessary to increase both γ' volume fraction and APB energy. Figure 4.12a shows how precipitate strengthening is affected by alloy chemistry if the DFT model for APB energy is considered. The results are for the alloy design space defined in Table 4.5, and three different Al concentrations (4 at.%, 8 at.% and 12 at.%) have been highlighted. It is evident that Al has the effect of pushing the data to the right; this is expected as Al increases the fraction of the γ' phase. The elements Ta, Nb and Ti partition strongly to the γ' phase. These elements have the combined effect of increasing γ' volume fraction and APB energy, thus creating the positive slope seen for each Al concentration. It is shown in Figure 4.11b that the precipitate strength is primarily a function of the Al content and the (Ti+Ta+Nb)/Al ratio. It is possible to explore possible trade-offs when designing a high strength turbine disc alloy using the Alloys-by-Design approach [1].



(a) (b)

Figure 4.12: Contour plots showing the precipitate strengthening for the alloy design space calculated using APB energy determined from DFT calculations: (a) effect of γ' volume fraction and APB energy effect precipitate strength, clusters delineating specific levels of AL in the alloy have been plotted, (b) composition-property map showing the effect of Al content and (Ti+Ta+Nb)/Al ratio on precipitate strengthening.

In order for a newly designed alloy to be viable for commercial application it must be readily processable using conventional processing methods. One estimate of the ease of processing for turbine disc alloys is the γ' solvus temperature. Previous work has found that γ' should be below 1200 °C in order to minimise the susceptibility to quench cracking [11]. Figure 4.13 shows the γ' solvus temperature is affected by alloy chemistry; it is evident that it is strongly influenced by Al content.

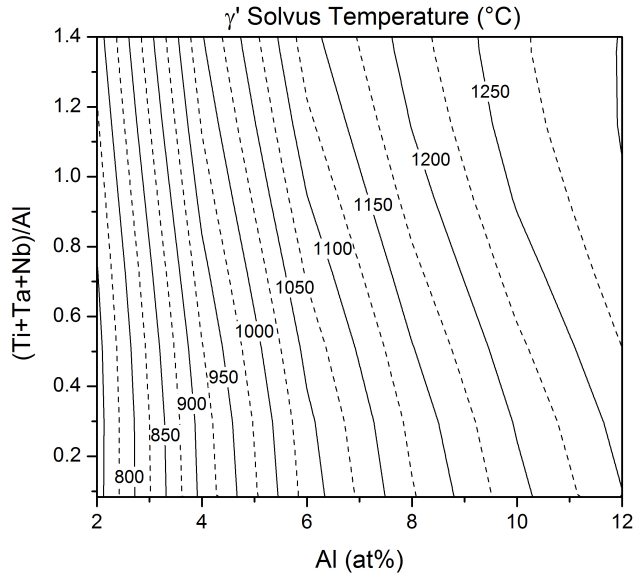


Figure 4.13: A composition-property map showing the effect of Al content and (Ti+Ta+Nb)/Al ratio on γ' solvus temperature.

In order to avoid alloys with unacceptably high γ' solvus temperatures it is necessary to keep the Al content below 10 at%. APB energy is strongly influenced by elements such as Ti, Ta and Nb. Phase equilibrium calculations for the alloy design space studied show that the ratio of (Ti+Ta+Nb)/Al is limited by the stability of the γ' phase, Figure 4.14. As this ratio is increased the alloy becomes more susceptible to deleterious phases, for example, the η phase. The modelling results for a number of commercial turbine disc alloys have been presented in Figure 4.12. The method described is a rational way to approach the design of new superalloys with improved strength.

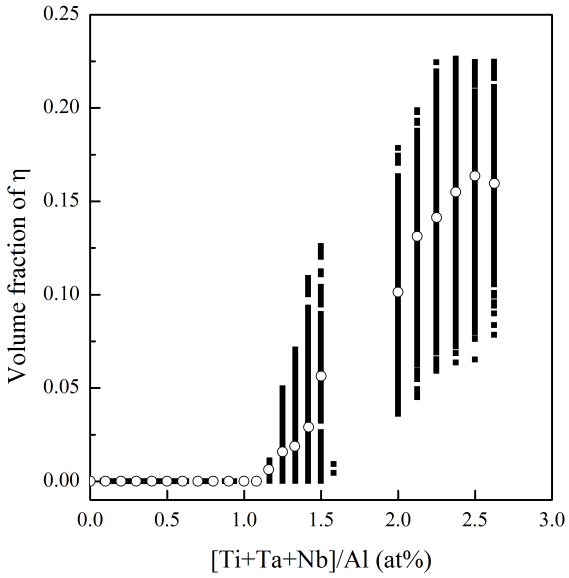


Figure 4.14: Alloys have been grouped based on their Ti/Al (at%) ratio. The fraction of η in the alloys has been displayed as a distribution. Open circles represent the median value for each distribution.

4.6 Conclusions

1. A direct relationship for the determination of the APB energy from a CALPHAD database for the $L1_2$ crystal structure in superalloys has been established. Predictions of APB energies on {111} for ternary and multi-component alloys have been obtained.

2. DFT calculations, using a Special Quasi-random Structures approach, have been used to study the accuracy of the CALPHAD predictions for simple ternaries. The method employed differs from that usually employed, which makes use of supercells.

3. Good correlation was observed between the CALPHAD and DFT predictions for the effect of Ti, W, Mo and Cr on the APB energy of Ni_3Al. Discrepancies were observed for the effect of Nb and Ta, with DFT predicting a more dramatic effect

on APB energy when compared to the CALPHAD calculations.

4. The discrepancy between the DFT and CALPHAD calculations for the Ni_3(Al,Ta) and Ni_3(Al,Nb) systems is attributed to the unreliability of the extrapolated energies for a random f.c.c. solid solution with high concentrations of Ta and Nb.

5. DFT calculations indicate that Ti, Nb, and Ta additions each have beneficial effects on the APB energy, with Ta showing the largest effect, followed by Nb and then Ti. This trend is not reproduced by the CALPHAD predictions. A model for APB energy based on the DFT calculations is proposed; the model shows an improved correlation between modelled alloy strength and the available experimental data.

6. Alloys-by-Design calculations are demonstrated. They indicate that there is a trade-off between APB energy and microstructural stability. Additions of Ti, Ta and Nb in order to increase the APB energy also increase the propensity to the formation of η phase which is known to be detrimental to mechanical properties.

5

Experimental Characterisation of Newly Designed Turbine Disc Alloys

5.1 Introduction

The next generation of gas turbine engines must have improved fuel efficiency with reduced emission of harmful gases, such as CO_2 or NO_x. Achieving these improvements requires newly designed engines to have increased turbine entry temperatures, higher rotational speeds and increased pressure ratios [85]. Meeting these design targets requires the development of new alloys capable of tolerating increased thermal and mechanical loads. The Alloys-by-Design (ABD) method [1, 152] has been used to optimise the chemistry of three new polycrystalline nickel-based superalloys for turbine disc applications.

The design requirements for the new alloy were based upon RR1000, Rolls-Royce's

most technologically advanced turbine disc material. The ABD method was employed to discover a disc alloy with an operational temperature of at least 800°C, representing a 50°C improvement in comparison to RR1000. The specific design requirements include:

- Yield strength – in the coarse grained microstructure – must be at least 95% of fine grain RR1000.
- Resistance to creep strain accumulation and fatigue crack growth must be improved in comparison to coarse grained RR1000.
- The precipitation of unwanted topologically close packed (TCP) phases must be avoided or reduced.
- Resistance to oxidation must remain comparable to RR1000.
- The cost of the new alloy must remain similar to that of RR1000.
- The alloy must be amenable to the current powder metallurgy process used for RR1000.

The ABD approach was used to optimise the additions of major alloying elements (Cr, Co, Al, Ti, Mo ,W, Ta). Minor alloying editions (C, B, Zr) have not been considered, the levels found to be optimal for RR1000 were used. The three new compositions were manufactured for the purpose of validating the modelling predictions made by the ABD software. Experimental validation has focused on microstructural characterisation, tensile behaviour, creep strength and oxidation resistance. The mechanical properties – tensile strength and creep resistance – have been assessed as a function of temperature. The oxidation behaviour has been assessed at the maximum operational temperature. These properties were studied to provide an initial insight into the accuracy of modelling predictions.

5.2 Optimising Alloy Chemistry

In Chapter 3 the ABD method was used to evaluate composition-property relationships in nickel-based superalloys over substantial compositional space. It was shown

that for turbine disc applications complex design trade-offs must be managed when selecting alloy chemistry. The most prevalent trade-off identified was between mechanical strength, oxidation resistance and microstructural stability, see Figure 3.11. From the compositional space studied three alloy chemistries that met the design specification were isolated. The compositions of the newly designed alloys are listed in Table 5.1, RR1000 has also been included for comparison. In this section the design rationale behind the compositions selected is presented.

Table 5.1: Chemistries (wt.%) for RR1000 and the new polycrystalline alloys designed using the ABD method.

Alloy	Cr	Co	Al	Ti	Ta	Mo	W	C	B	Zr	Ni
RR1000	15.00	18.50	3.00	3.60	2.00	5.00	-	0.027	0.015	0.06	Bal
ABD-D1	20.25	19.00	3.94	3.45	2.00	-	1.00	0.027	0.015	0.06	Bal
ABD-D2	17.25	19.00	3.81	3.45	2.00	-	3.00	0.027	0.015	0.06	Bal
ABD-D3	15.25	19.00	3.69	3.45	2.00	-	5.00	0.027	0.015	0.06	Bal

The ABD model identified that γ' volume fraction significantly influenced the properties of the turbine disc alloys. Modelling predictions showed that increasing γ' volume fraction would improve yield strength and reduce density. It is also known that increased levels of γ' phase can improve resistance to creep [2]. From the calculations presented in Chapter 3 it was determined that the volume fraction of γ' must be greater than 50% for sufficient yield strength and creep resistance. The trade-offs considered made it possible to identify the upper limit for γ' volume fraction. The γ' solvus temperature and propensity to TCP phases increased as the fraction of γ' increased. A high γ' solvus is undesirable as it increases the propensity to quench cracking during processing [11], the TCP phase are known to degrade mechanical properties [15]. Hence, the upper limit for γ' volume fraction was determined to be 55%. Predictions made using the CALPHAD method showed that alloys required the sum of γ' forming elements (Al, Ti, Ta) to be within 8 - 10 wt.% to produce the desired fraction of γ' phase. For the alloys selected the additions of γ' forming elements was fixed at approximately 9

wt.%. Further consideration was given to the exact levels of Al, Ti and Ta included in the final alloy. The Ti/Al ratio was fixed at approximately 1 (in wt.%), previous work has reported that maximising this ratio is beneficial for yield strength [45, 121, 153]. The Ti/Al ratio was limited to 1 as increasing it further may lead to the formation of the unwanted η phase (Ni_3Ti) [6, 153]. Tantalum was added as it has been found to improve the resistance to crack propagation in turbine disc alloys [98]. However,the high cost and density of Ta required that additions were limited to 2wt.%.

Careful optimisation of the elements which partition to the γ phase (Co, Cr, Mo and W) was required as they promote the formation of TCP phases [14]. Additions of Mo and W were found to improve yield strength and creep resistance. However, these elements negatively impact upon density and microstructural stability. The addition of W in favour of Mo was used as a novel design concept. The low rate of diffusion of W in Ni provided a stronger effect on creep resistance in comparison to Mo. There are currently no turbine disc alloys which are free from Mo. The low levels of W required for good creep properties allowed for better control over microstructure stability. In the alloys designed W levels of 1 wt.%, 3 wt.% and 5 wt.% were selected to understand the best balance between mechanical properties and density.

High levels of Cr are required for oxidation resistance, however, this can often promote the formation of deleterious phases such as σ [15]. The current model for oxidation ranks alloys based on the activity of Cr, where a high Cr activity is preferred. The alloys selected had an activity of Cr higher than that of RR1000. The CALPHAD model allowed for selection of microstructurally stable alloys containing high levels of Cr. For the three new alloys Cr contents of 15.25 wt.%, 17.25 wt.% and 20.25 wt.% were selected. Additions of Co content were found to increase the creep resistance without any effect on alloy density or microstructural stability, it has also been reported that Co lowers the γ' solvus temperature [10] which is beneficial for processing. A high Co

content of 19 wt.% was specified to provide creep resistance and improve processing for the selected alloys.

A summary of material properties estimated using the ABD model is given in Table 5.2, modelling results for RR1000 have been included for comparison. The compositions of these alloys have been chosen with varying levels of W and Cr, with the following rationale. Whilst W is expected to improve the high temperature strength, excessive levels especially in combination with Cr are known to give rise to the precipitation over time of topologically close-packed (TCP) phases such as sigma, R and P, which is unacceptable. Alloy D1 has been designed for good oxidation resistance at the expense of creep resistance and strength. Alloy D3 has been designed for high strength and superior creep resistance at the expense of oxidation resistance. Alloy D2 is expected to have the optimal balance of oxidation resistance, creep resistance and strength.

Table 5.2: Modelling predictions for the properties of RR1000 and newly designed alloys. Calculations conducted at 650°C.

Alloy	**Volume Fraction** γ'	**Volume Fraction** σ	**Density (g/cm^3)**	**Activity of Cr**	**Yield Strength (MPa)**	**γ' Solvus (°C)**	**Cost (£/kg)**	**Creep Merit Index** ($m^{-2}s \times 10^{-19}$)
RR1000	0.47	0.05	8.31	0.009	1051	1150	11.88	1.16
ABD-D1	0.53	0.02	8.07	0.011	1046	1170	12.10	1.25
ABD-D2	0.54	0.02	8.22	0.011	1101	1175	12.30	1.31
ABD-D3	0.54	0.03	8.35	0.011	1156	1175	12.51	1.37

5.3 Experimental Procedures

5.3.1 Material Preparation

The alloys ABD D1-D3 were produced by ATI powder materials using their laboratory scale gas atomiser. This equipment was used to make 30 lbs of powder for each experimental alloy. The powder was screened using a -270 mesh so that powder particles

were no larger than 53 μm in diameter. The screened powder was loaded into mild steel cans for hot isostatic pressing (HIP). The HIP cycle was conducted at 100 MPa at a temperature of 1007°C, this was below the γ' solvus temperature. For each composition 2 mults were produced measuring 65 mm in diameter and 76 mm in height.

The HIP compacts were forged at a strain rate of 0.2 per minute. The height of the final forging was approximately 34 mm, this allowed for the extraction of 2 rows of test bars using electro-discharge machining (EDM) wire erosion processes. The final forgings are shown in Figure 5.1.



Figure 5.1: Final forgings of alloys ABD D1-D3 measuring approximately 110mm in diameter.

The forged material required a super-solvus heat treatment, which is conducted above the γ' solvus temperature. The solvus temperature for the newly designed alloys was calculated using CALPHAD method described in Chapter 3, the solvus temperature was also measured experimentally using a NETZSCH 404 F1 Pegasus® differential scanning calorimeter (DSC). Specimens, 3 mm in diameter and 1 mm thick, were produced from the HIP material. All surfaces on the specimen were ground to a 1200 grit

finish using silicon carbide griding paper, after which they were cleaned for 5 minutes in ethanol using an ultrasonic bath. The samples were placed in a platinum crucible with an alumina liner. Heating was conducted in a protective argon environment using a flow rate of 70 ml/min. The heating cycle was as follows: samples were heated from 700°C to 1210°C at 10°C/min, at the maximum temperature there was an isothermal hold for 15 minutes, samples were then cooled to 500°C at 10°C/min. Each specimen received this heating cycle twice, the first cycle was used to remove any effects that processing history may have on the γ' solvus temperature. The results of the DSC testing for each alloy are presented in Figure 5.2. The γ' solvus temperature for alloys D1, D2 and D3 were 1111°C, 1118°C and 1140°C, respectively.

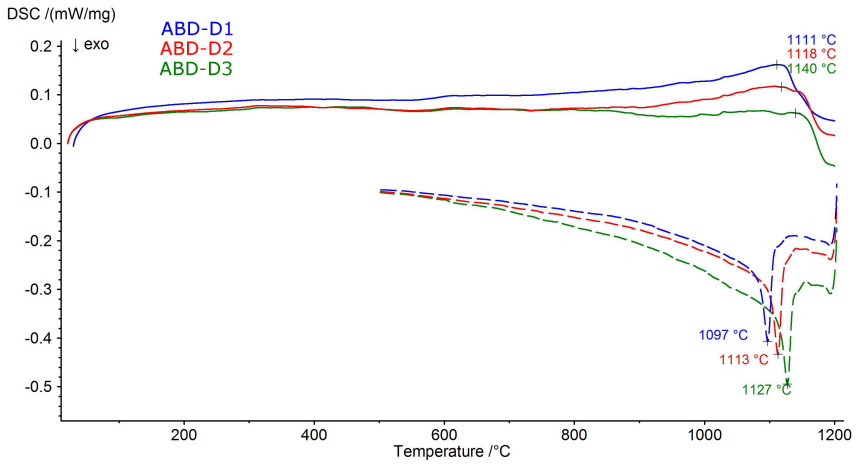


Figure 5.2: Measurement of γ' solvus temperature for alloys D1 - D3 using DSC.

The heat treatment used for the new alloys is illustrated schematically in Figure 5.3. Bar specimens extracted from the forgings were heat treated – as opposed to heat treating the entire forging – to provide good uniformity of heat in the specimen. This also reduced the propensity to quench cracking during the heat treatment process. The super-solvus heat treatment was carried out at 1170°C for 2 hours followed by a controlled quench of 1°C/s to a temperature of 1050°C. The alloys were then aged at

temperature of 850°C for 4 hours. This aging temperature was proposed as it is 50 $°C$ above the maximum operating temperature required for the new alloys.

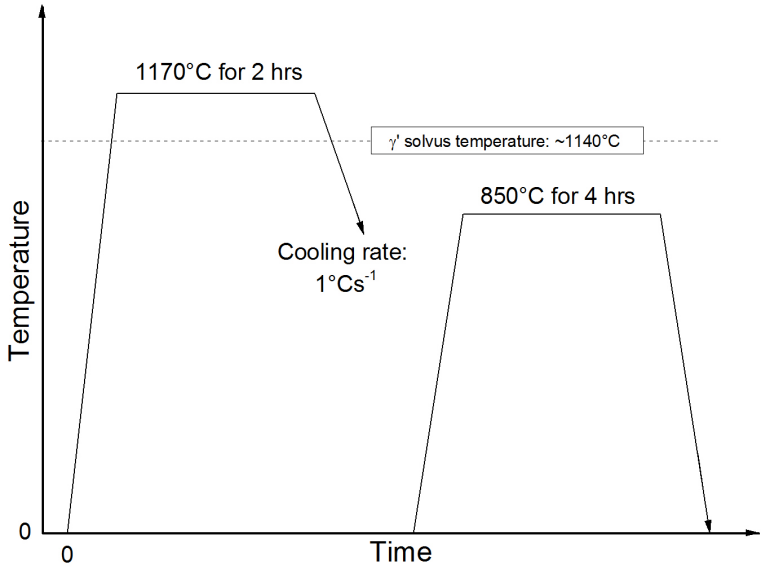


Figure 5.3: Heat treatment process applied to alloys ABD D1-D3.

5.3.2 Microstructural Analysis

The specimens prepared for optical microscopy were polished to a 1 μm surface finish using a diamond suspension then etched with Kalling No.2 solution (5 g $CuCl_2$ + 100 ml Hydrochloric acid + 100 ml ethanol) to reveal the grain boundaries. The γ/γ' microstructure was examined using scanning electron microscopy (SEM), polished specimens were electrolytically etched using 10% phosphoric acid in water. The γ' volume fraction and precipitate size was determined using the open source image analysis software ImageJ [154]. The precipitate size was calculated by taking the area of each precipitate measured, A, and converting this into and equivalent diameter, d, using $d = 2\sqrt{A/\pi}$.

5.3.3 Atom Probe Tomography

APT specimens were prepared by first electropolishing in an electrolyte solution of 10% perchloric acid and 90% acetic acid using around 30V DC. The specimens were further sharpened in a mixture of 2% perchloric acid and 98% butoxyethanol during a second electropolishing stage, using DC voltages of around 6-9V. Specimens were subsequently analysed using a Cameca LEAP 3000X-HR instrument. The analyses were carried out in voltage pulsing mode with a specimen temperature of 50 K, using a 25% pulse fraction to maximise compositional accuracy, and at a pulse rate of 200 kHz. Reconstructions of the data/compositions of the various phases were obtained using the standard IVAS software.

5.3.4 Oxidation Testing

Cyclic oxidation experiments were used to characterise the oxidation performance of the newly developed turbine disc alloys. A number of commercially available turbine disc alloys, listed in Table 5.3, were also examined using the same experimental procedure. This allowed for a direct comparison between the newly developed alloys and the current state of the art. Studying this number of alloys also generated a larger set of results for validation of the oxidation model used in the ABD software.

Table 5.3: Chemistry (at.%) of polycrystalline alloys studied in oxidation experiment. The levels of minor alloying elements C, B and Zr have not been included.

Alloy	Cr	Co	Mo	Al	Ti	Ta	W	Nb	Fe	Hf	Ni
ABD D1	21.6	17.8	-	8.1	4.0	0.6	0.3	-	-	-	Bal
ABD D2	18.7	18.2	-	8.0	4.1	0.6	0.9	-	-	-	Bal
ABD D3	16.8	18.5	-	7.8	4.1	0.6	1.6	-	-	-	Bal
ATI 718+	20.2	9.0	1.6	3.1	0.9	-	0.3	3.5	9.9	-	Bal
IN100	13.0	17.0	1.9	10.0	4.9	-	-	-	-	-	Bal
IN738	17.6	8.2	1.0	7.2	4.0	0.6	0.8	0.6	-	-	Bal
Inconel 718	21.2	-	1.9	1.1	1.1	-	-	3.3	19.6	-	Bal
RR1000	16.5	18.0	3.0	6.4	4.3	0.6	-	-	-	0.2	Bal
Udimet 720Li	17.4	14.3	1.8	5.2	5.9	-	0.4	-	-	-	Bal
Waspaloy	21.4	13.0	2.6	2.7	3.6	-	-	-	-	-	Bal

The oxidation specimens used for this study were approximately 1 mm thick with a surface area of approximately 300 mm^2. The specimens were ground to a 1200 grit surface finish using silicon carbide paper, after which they were cleaned in ethanol for five minutes using an ultrasonic bath. The mass of the cleaned samples was measured using a microbalance with a resolution of ± 10 μg. Samples were placed in an alumina boat and exposed to lab air in a tube furnace preheated to 800°C. The uniform heated length in the tube furnace had a temperature stability of ± 10°C. Samples were removed in 20 hour intervals, at each interval the samples were weighed then placed back into the furnace. The testing was conducted for a total of 100 hours. After oxidation the samples were cold mounted in an epoxy resin ensuring no damage was caused to the oxide scale. The mounted samples were polished to a 1 μm surface finish using a diamond suspension. This revealed the cross sectional profile of the oxide scale for analysis using SEM and electron micro-probe analysis (EPMA).

5.3.5 Mechanical Testing

Heat treated bars were machined to Rolls-Royce drawing number RLH10259. The specimens had a gauge length of 20 mm and a gauge diameter of 4 mm. Creep and tensile tests were conducted for each alloy using the conditions defined in Table 5.4. All mechanical testing was conducted at IncoTest UK.

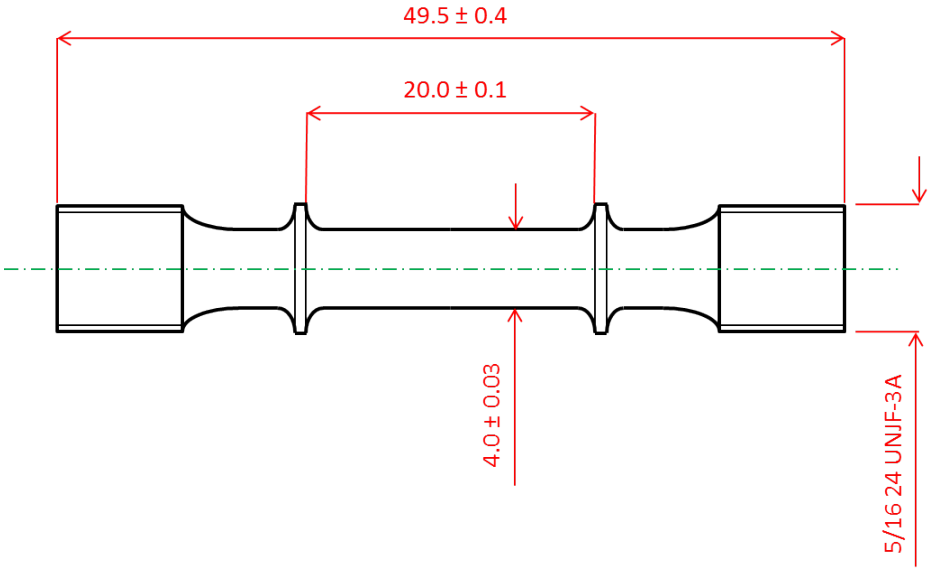


Figure 5.4: Geometry of RLH10259 test specimen used for tensile and creep testing.

Table 5.4: Conditions used for tensile and creep testing.

Test Type	Temperature (°C)	Stress (MPa)	Strain Rate
Tensile	20	-	0.01
	600	-	0.01
	700	-	0.01
	800	-	0.01
Creep	650	1000	-
	700	800	-
	750	600	-
	800	300	-

5.4 Results

5.4.1 Microstructural Analysis

The microstructure of the alloys after heat treatment was investigated using both optical and scanning electron microscopy. Figure 5.5 shows the grain structure of alloy D3 after the final aging heat treatment. For alloys D1-D3 the average grain size was between $15-30$ μm, this was the target grain size selected to provide a balance between yield strength, creep strength and resistance to crack propagation.

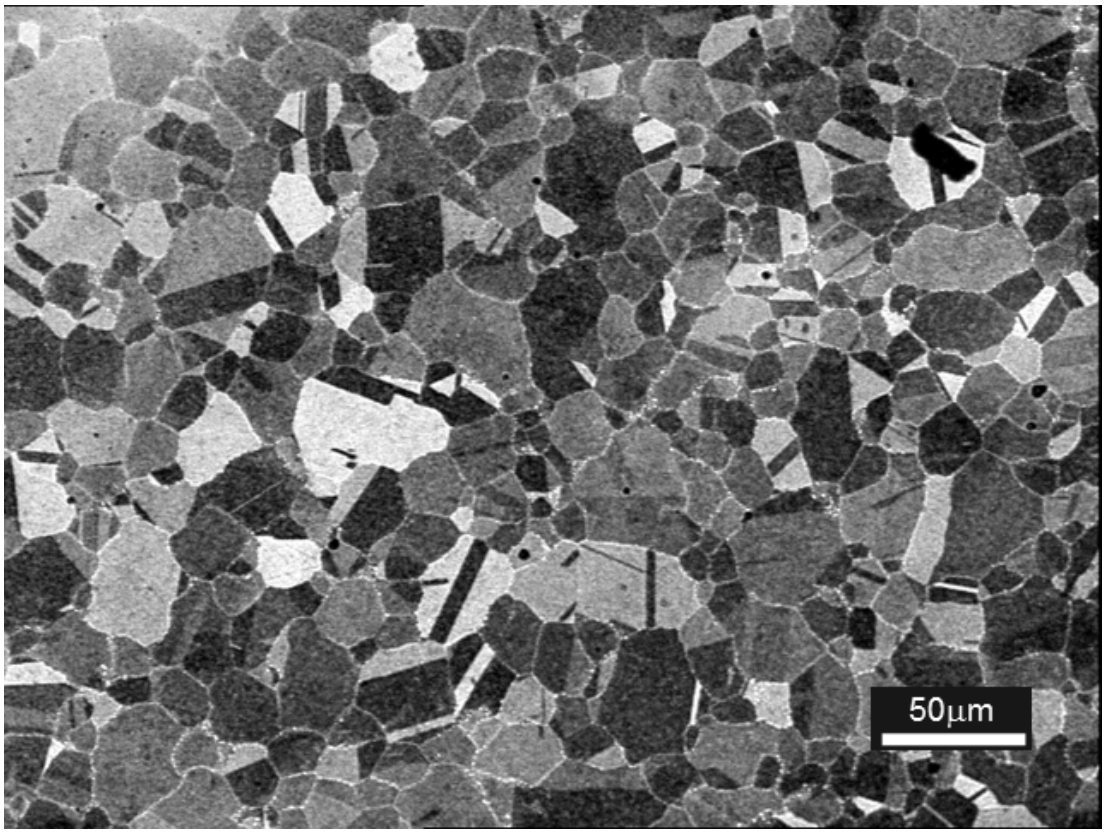


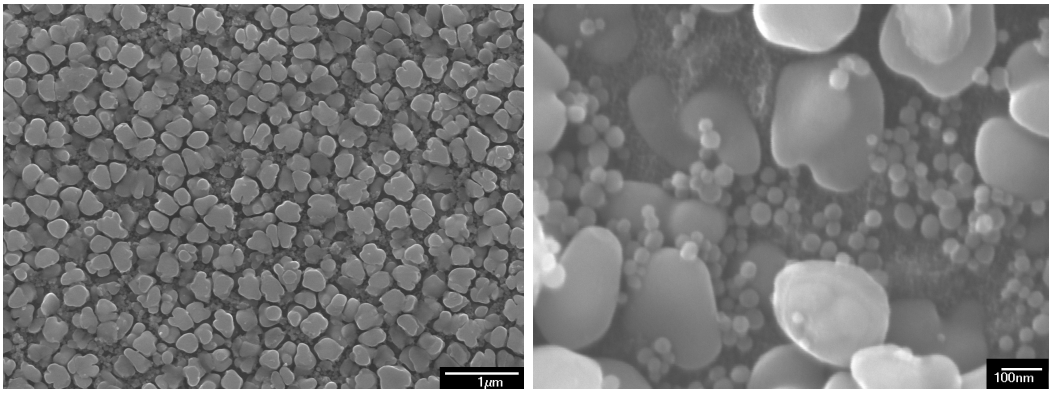
Figure 5.5: The microstructure of alloy D3 after aging heat treatment, observed using optical microscopy.

The intragranular γ/γ' microstructure is shown in Figure 5.6. The precipitates in

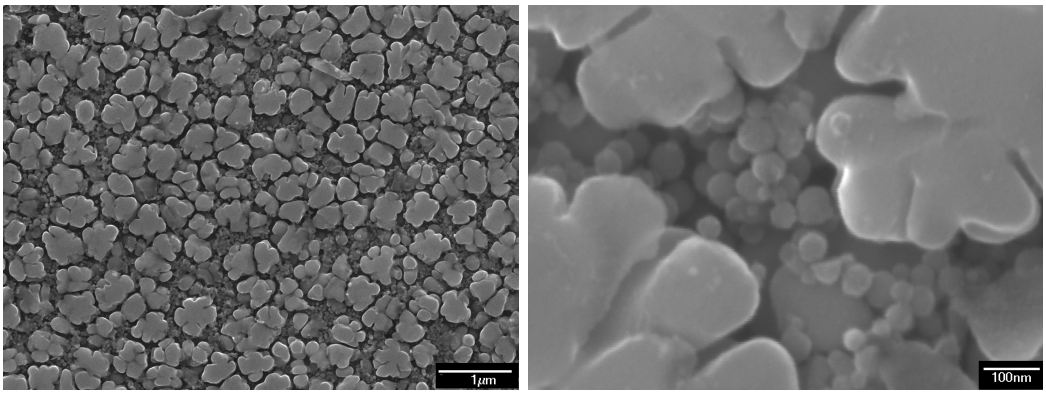
alloy D1 appeared close to spherical, differing from alloys D2 and D3 which had an octodendritic clover leaf shape. The volume fraction of γ' – determined from image analysis of SEM micrographs – agreed closely with predictions made using CALPHAD modelling, see Table 5.5. The precipitate size distribution for secondary γ' is shown in Figure 5.7. The precipitate size in alloy D1 had a normal distribution, with an average precipitate diameter was approximately 275 nm. In alloys D2 and D3 a bi-modal size distribution was observed. For each alloy two individual peaks were observed with averages at approximately 150 nm and 350 nm. It was not possible to quantify the volume fraction or size distribution of tertiary γ' using SEM, however, the images showed that tertiary precipitates were present with a diameters between 40-60 nm.

Table 5.5: Measured volume fraction of γ' compared with CALPHAD predictions.

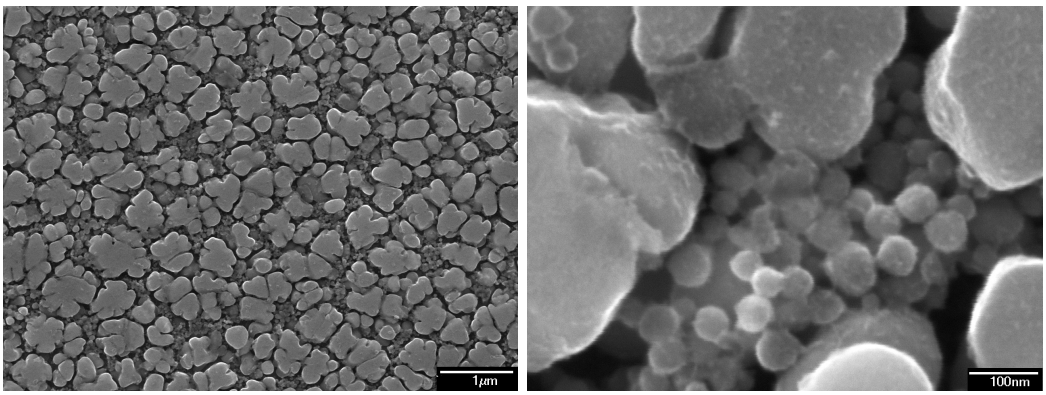
		Measured (Area Fraction)			Measured (APT)
Alloy	CALPHAD	Average	Minimum	Maximum	
ABD D1	53%	49%	45%	52%	45%
ABD D2	54%	54%	50%	59%	48%
ABD D3	54%	55%	51%	59%	50%



(a)



(b)



(c)

Figure 5.6: SEM secondary electron images showing the γ' morphology after heat treatment for alloy, (a) D1, (b) D2, (c) D3.

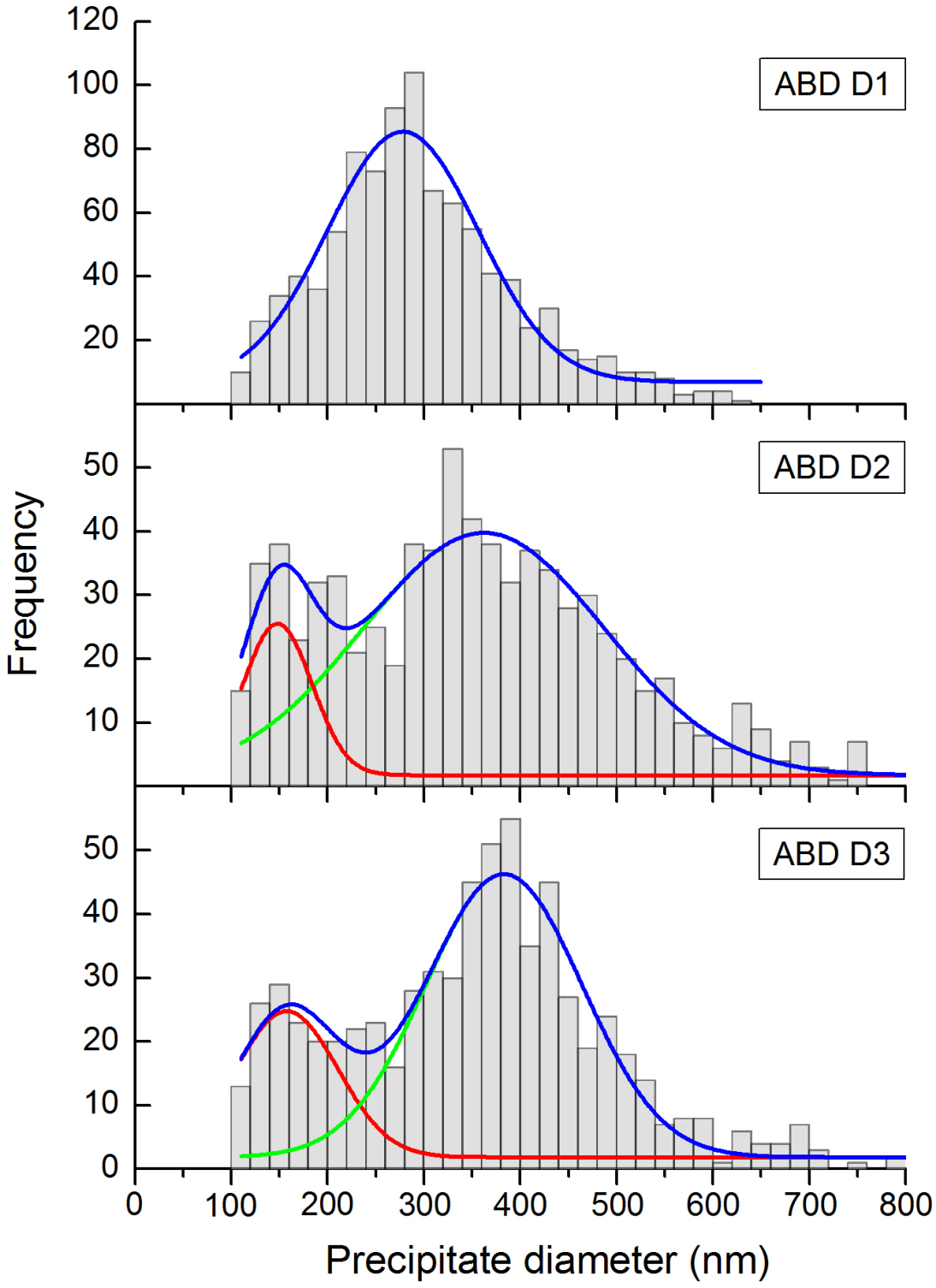


Figure 5.7: Precipitate size distribution for secondary γ' determined for alloys D1-D3 using ImageJ analysis.

The compositions of the γ and γ' phases was measured using APT, an example of a reconstructed atom probe needle is given in Figure 5.8. The measured composition of the γ and γ' phase for each alloy is given in Table 5.6. The results show that Al, Ti and Ta strongly partition to the γ' phase, Cr partitioned strongly to the γ phase. Concentrations of Co and W were observed in both phases, a preference for γ was observed for both these elements with partitioning coefficients (γ:γ') of approximately 3.2 and 1.7, respectively. Overall, the phase compositions predicted using Thermo-Calc were in good agreement with experimental results. One notable difference between the modelling and experimental data was a significant concentration of Al content measured in the γ phase.

Phase compositions determined by APT were used to calculate the volume fraction of γ' in alloys D1-D3. This was calculated using Lever rule,

$$C_{\mathrm{n}} = f C_{\gamma'} + (1 - f)\, C_{\gamma} \tag{5.1}$$

where f is the volume fraction of γ' and C_{n}, $C_{\gamma'}$ and C_{γ} is the composition of the alloy, γ' phase and γ phase, respectively. By plotting $C^{n} - C^{\gamma}$ vs. $C^{\gamma'} - C^{\gamma}$ for each alloy constituent it is possible to determine the volume fraction of γ' from the gradient of the linear fit, Figure 5.9. The volume fraction of γ' was determined to be 45%, 48% and 50% for alloys D1, D2 and D3, respectively. The volume fraction of γ' calculated from the Lever rule was lower than the CALPHAD prediction by approximately 5-10%.

Table 5.6: Phase compositions and partitioning coefficients determined using CALPHAD compared with APT measurements.

	Cr	Co	Al	Ti	Ta	W	Zr	C	B
D1									
γ /at.% (Calculated)	43.3	28.4	0.7	0.0	0.0	0.2	0.000	0.020	0.160
γ /at.%(Measured)	38.7	25.0	3.3	0.5	0.0	0.4	0.000	0.050	0.000
γ' /at.% (Calculated)	2.2	8.5	14.8	7.5	1.1	0.4	0.000	0.000	0.000
γ' /at.% (Measured)	1.8	7.8	14.3	8.7	1.4	0.2	0.000	0.000	0.020
Partitioning coefficient ($\gamma : \gamma'$)									
Calculated	19.8	3.4	0.0	0.0	0.0	0.6	0.000	0.000	0.000
Measured	21.0	3.2	0.2	0.1	0.0	1.7	0.000	0.000	0.000
D2									
γ /at.% (Calculated)	38.2	29.0	0.8	0.0	0.0	0.9	0.000	0.010	0.170
γ /at.%(Measured)	34.2	26.8	2.7	0.5	0.0	1.1	0.000	0.010	0.000
γ' /at.% (Calculated)	2.0	9.0	14.2	7.5	1.0	1.0	0.000	0.000	0.000
γ' /at.% (Measured)	1.9	8.4	13.3	8.6	1.5	0.7	0.000	0.000	0.020
Partitioning coefficient ($\gamma : \gamma'$)									
Calculated	19.0	3.2	0.1	0.0	0.0	0.9	0.000	0.000	0.000
Measured	18.3	3.2	0.2	0.1	0.0	1.7	0.000	0.000	0.000
D3									
γ /at.% (Calculated)	34.7	29.4	0.8	0.0	0.0	1.7	0.000	0.010	0.170
γ /at.%(Measured)	33.0	27.0	3.0	0.7	0.1	1.8	0.000	0.030	0.000
γ' /at.% (Calculated)	1.9	9.4	13.8	7.6	1.0	1.4	0.000	0.000	0.000
γ' /at.% (Measured)	1.9	8.7	13.6	8.5	1.4	1.0	0.000	0.000	0.030
Partitioning coefficient ($\gamma : \gamma'$)									
Calculated	18.7	3.1	0.1	0.0	0.0	1.2	0.000	0.000	0.000
Measured	17.1	3.1	0.2	0.1	0.1	1.9	0.000	0.000	0.000

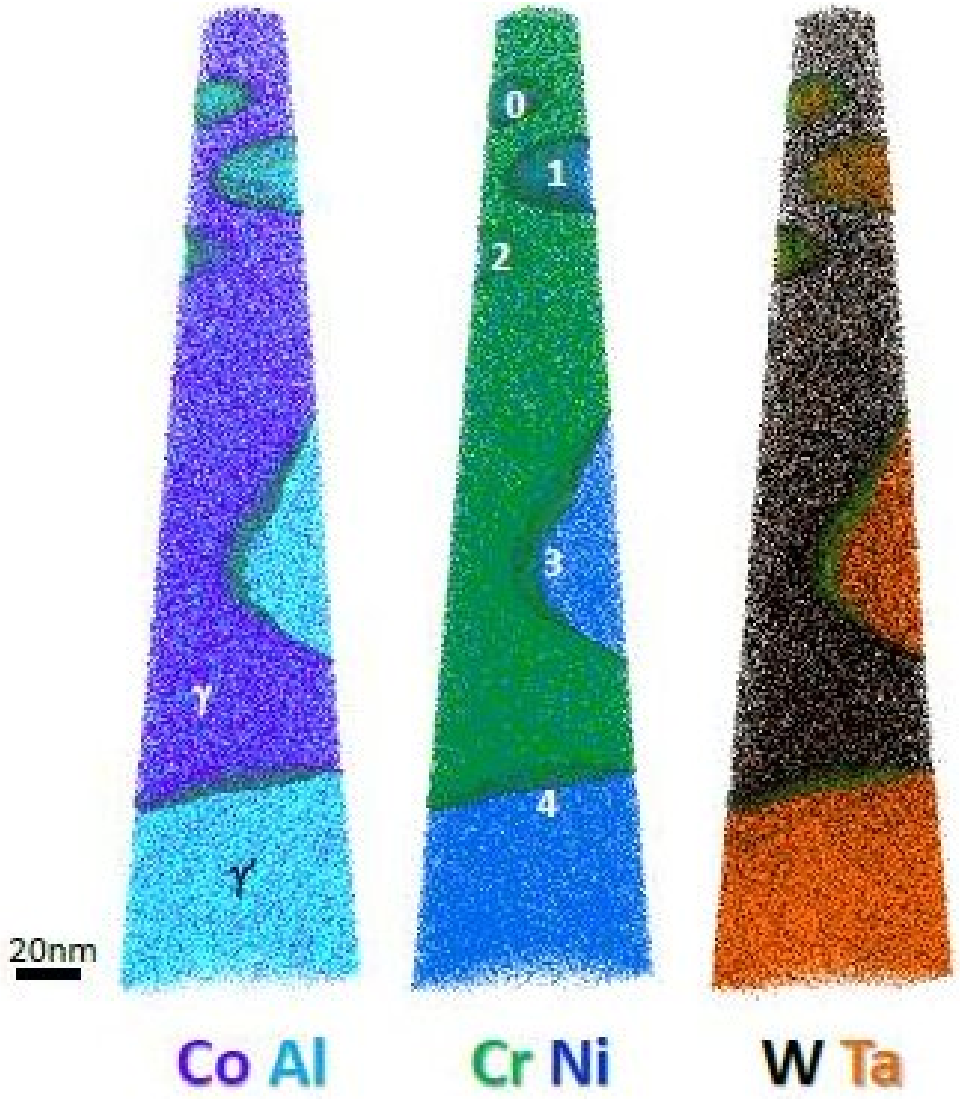
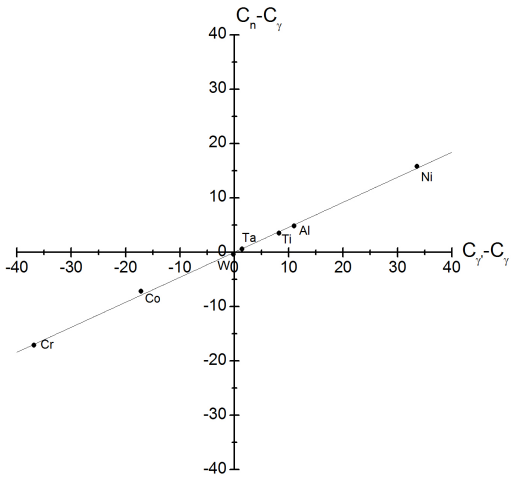
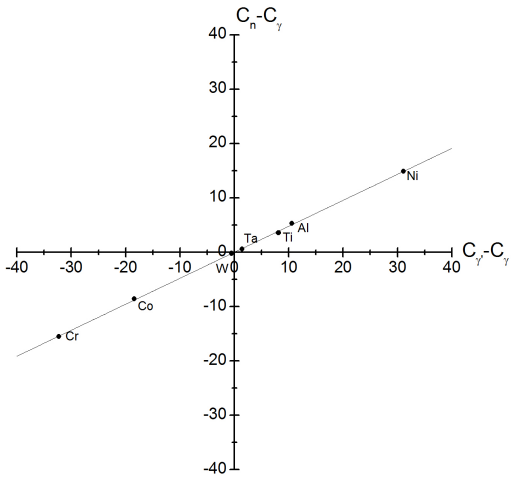


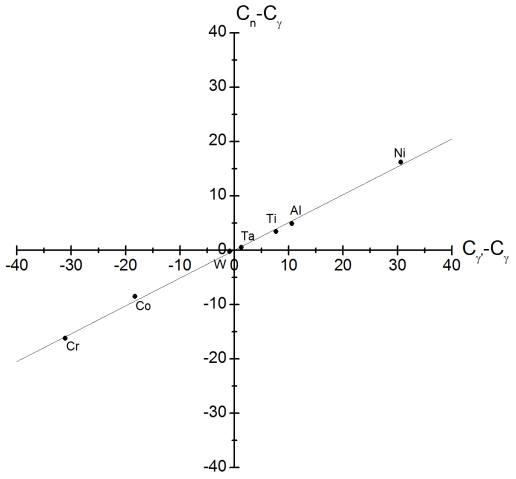
Figure 5.8: Reconstruction of atom probe data for alloy D2.



(a)



(b)



(c)

Figure 5.9: Plots of $C^n - C^\gamma$ vs. $C^{\gamma'} - C^\gamma$, constructed using the phase compositions measured using APT for alloy (a) D1, (b) D2, (c) D3.

5.4.2 Mechanical Properties

Figure 5.10a shows the variation in yield strength for the new alloys as a function of temperature, the results are compared with RR1000 in both a fine grain (FG) and coarse grain (CG) microstructure. Alloys D1-D3 have a grain size equivalent to that of CG RR1000. The RR1000 alloy in the FG microstructure is approximately 200 MPa stronger than the coarse CG variant between ambient temperature and 700°C. At all temperatures alloy D1 had the lowest strength, alloy D3 was the strongest. The yield strength of the alloys increased as the Cr content reduced and the W content is increased, for each alloy the strength increase was approximately 50 MPa. The yield strength of the new alloys was equivalent to CG RR1000 between ambient temperature and 700°C. However, the new alloys did not achieve the target yield strength – 95% of RR1000(FG) – within this temperature range. At 800°C the new alloys performed better than RR1000, alloy D3 was approximately 150MPa stronger than RR1000(CG). The required yield strength was achieved for all three alloys at 800°C.

A neural network was used to predict yield strength when designing alloys D1-D3. The yield strength predicted by the neural network is presented as a function of temperature in Figure 5.10a. It was estimated that alloy D1 would have similar strength to RR1000, alloys D2 and D3 were expected to have increased yield strength of approximately 80 MPa and 130 MPa, respectively. The relative change in yield strength predicted for alloys D1-D3 – approximately 70MPa for each alloy – was in good agreement with experimental observations. However, the neural network systematically over estimated the yield strength by approximately 200 MPa.

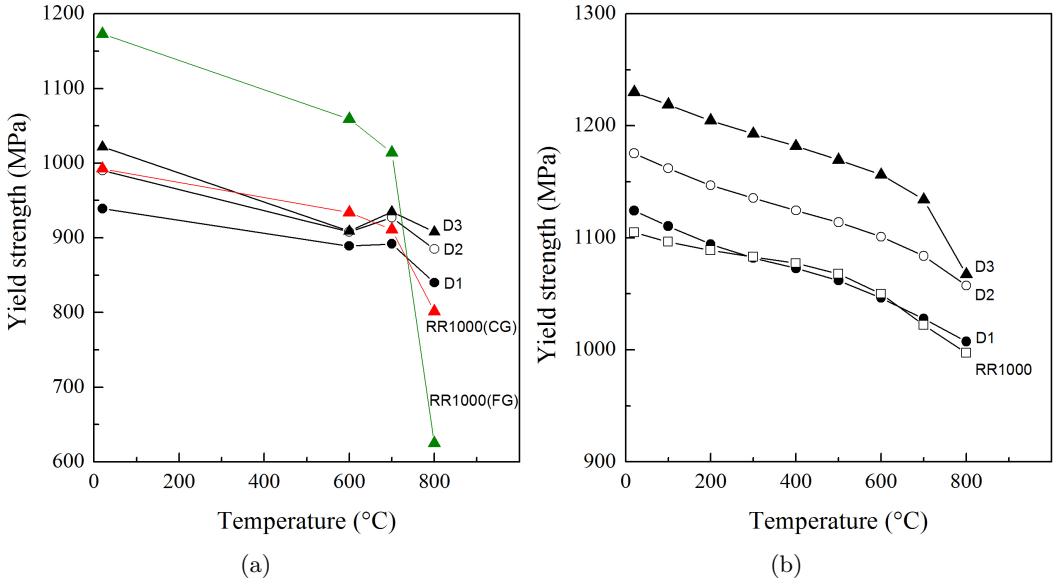


Figure 5.10: The temperature dependent yield strength for alloys D1-D3 determined, (a) experimentally, (b) using neural network predictions.

Creep resistance was tested over a range of stresses and temperatures for alloys D1-D3, the rupture life for each test is listed in Table 5.7. Alloy D1 preformed the worst in creep, alloy D3 preformed the best. As the Cr content was reduced and the W content was increased the creep resistance improved. The results were plotted on a Larson-Miller plot allowing comparison with RR1000, Figure 5.11. Creep resistance increased by 1 Larson-Miller parameter between alloys D1 to D3. The target for creep life was a 50°C improvement over RR1000(CG), the new alloys did not satisfy this requirement.

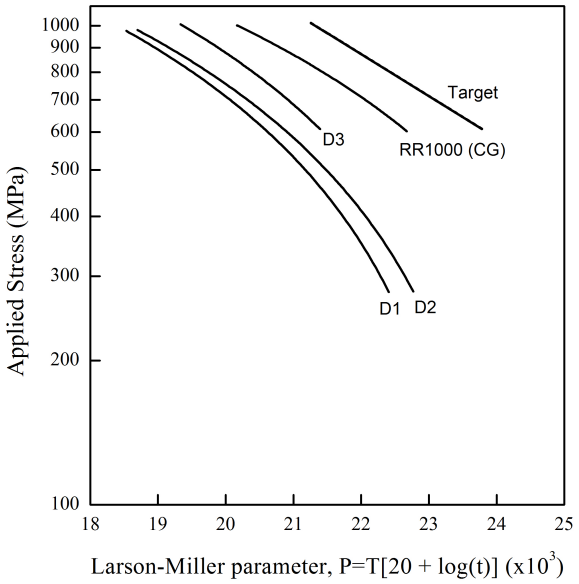


Figure 5.11: Larson-Miller plot for alloys D1-D3, RR1000 is included for comparison.

Table 5.7: Creep rupture life in hours for alloys D1-D3 for a number of creep conditions.

	Creep Condition			
Alloy	1000MPa/650°C	800MPa/700°C	600MPa/750°C	300MPa/800°C
ABD D1	1.2	-	0.8	7.6
ABD D2	1.8	2.2	1.4	16.5
ABD D3	8.8	11.2	8.1	-

5.4.3 Oxidation Resistance

The oxidation resistance of alloys D1-D3 was evaluated along with a number of commercially available turbine disc alloys. Oxidation test were conducted at 800°C in air over a 100 hour period. The specific mass change for the new alloys is presented as a function of time in Figure 5.12, RR1000 has been included for comparison. Alloy D1 – containing the highest Cr content – performed the best in oxidation, the rate of oxidation was significantly lower than that of RR1000. The oxidation resistance of alloys D2 and D3 was similar to RR1000 over the 100 hour period. The oxidation kinetics for all the turbine discs studied followed a parabolic law. The parabolic rate constant,

K_p, was determined from the change in mass, Δm, over the oxidation time, t, using the following Equation,

$$(\Delta m)^2 = K_p t \tag{5.2}$$

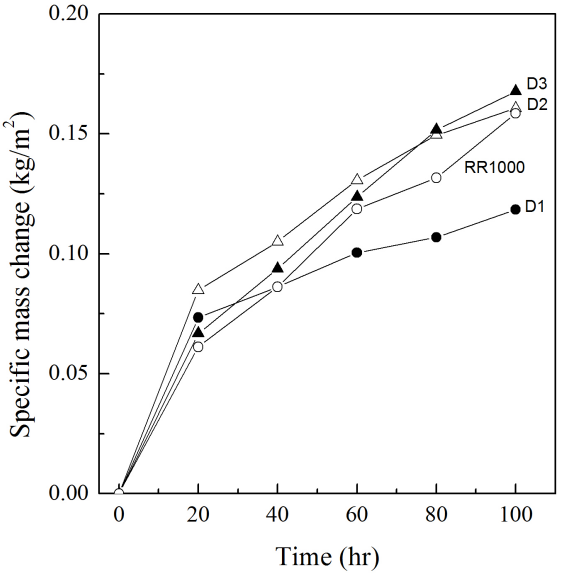


Figure 5.12: Oxidation rate for newly developed turbine disc alloys after 100 hours exposure in air at 800°C. A comparison is made with RR1000.

This study had two main objectives: (i) benchmark the new alloys against the current state of the art, (ii) evaluate the performance of the model for estimating the oxidation resistance which is based upon the activity of Cr. Figure 5.13a shows the correlation between the activity of Cr calculated for each alloy and the measured parabolic rate constant. A negative correlation is expected, however, only a weak correlation between activity of Cr and oxidation resistance is observed. The results in Figure 5.12b show that there is strong correlation between the Cr content and oxidation resistance.

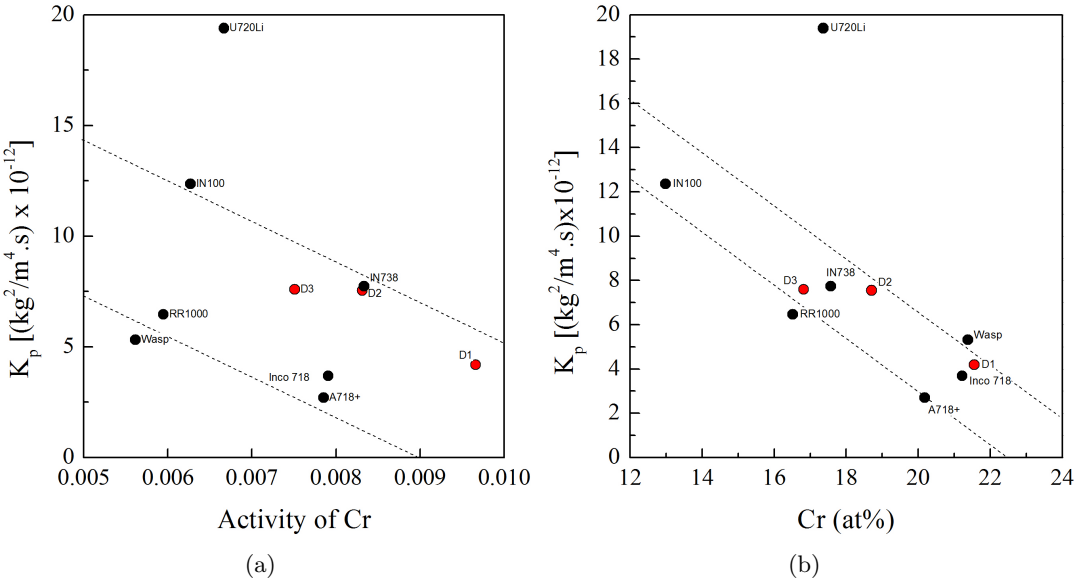
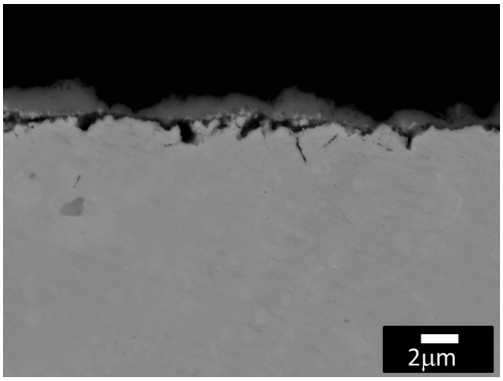
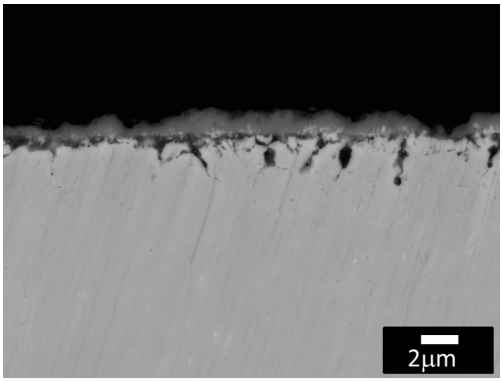


Figure 5.13: The parabolic oxidation rate for alloys D1-D3 and a number of commercial turbine disc alloys compare with, (a) calculated activity of chromium in the alloy, (b) chromium content in at%.

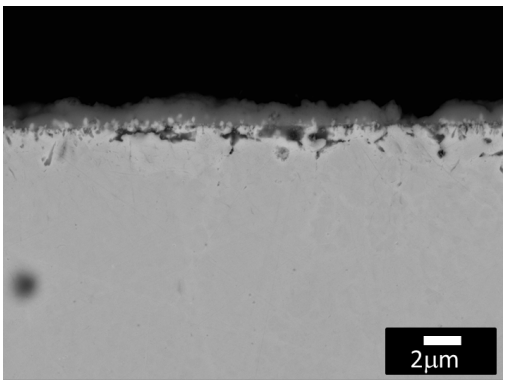
A cross sectional view of the oxidation damage for alloys D1-D3 was observed using SEM, Figure 5.14. A similar microstructure was observed for oxide developed on each alloy. The distribution of alloying elements within the oxygen affected zone was examined using EPMA, see Figure 5.15. For each alloy the outer scale was determined to be chromia rich. Below the chromia rich scale was the development of an inward growing alumina oxide. Results from the EPMA mapping showed significant concentrations of Ti were contained within the chromia rich oxide scale.



(a)

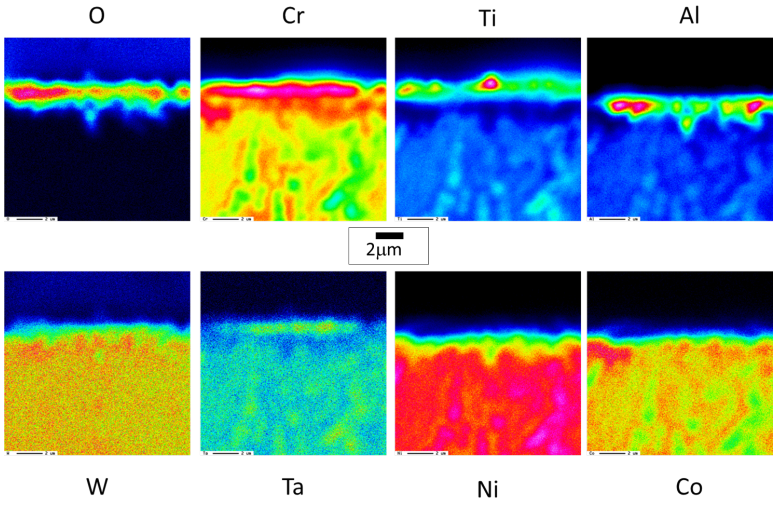


(b)

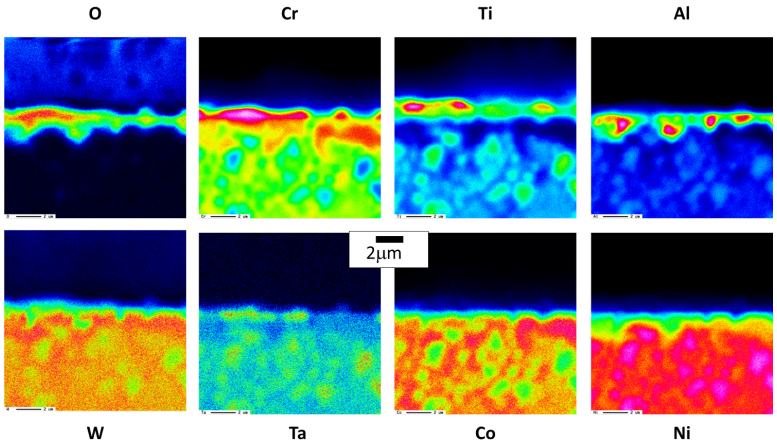


(c)

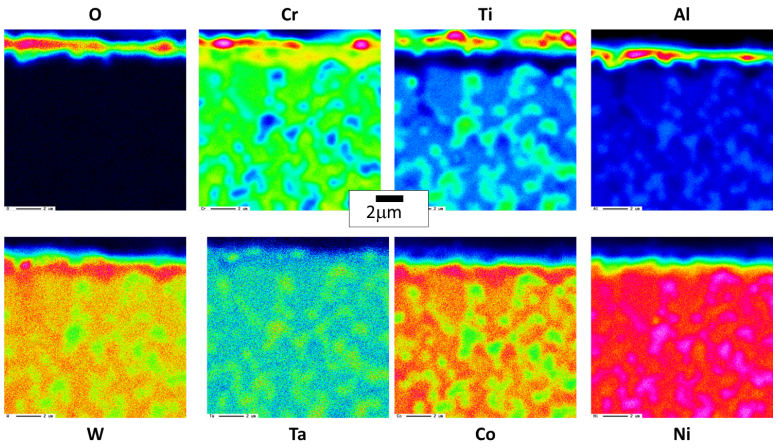
Figure 5.14: Backscattered electron images showing the oxidation damage after 100 hours of exposure in air at 800°C for alloy (a) D1, (b) D2, (c) D3.



(a)



(b)



(c)

Figure 5.15: EPMA maps showing the distribution of alloying elements after 100 hours of exposure in air at 800°C for alloy (a) D1, (b) D2, (c) D3.

5.5 Discussion

The ABD method was used to optimise the chemistry of three new polycrystalline nickel-based superalloys for turbine disc applications. Modelling predictions were validated experimentally with focus was placed on microstructure, yield strength, creep resistance and oxidation resistance. The CALPHAD method accurately determined the volume fraction and composition of γ and γ' phases, this was confirmed using a combination of SEM and APT. Accurate prediction of phase equilibrium is essential when designing new alloys, as these results are used to determine design critical material properties, for example, yield strength as calculated in Chapter 4. Although some of the new alloys showed improved oxidation resistance and yield strength at 800°C, no alloy achieved all the intended design targets. Mechanical properties and oxidation resistance are discussed in Section 5.5.1 and Section 5.5.2, respectively. In section 5.5.3 the lessons learned from the modelling and experimental work are discussed, suggestions are made on how the chemistry for the new turbine disc alloy could be further improved to meet design targets.

5.5.1 Mechanical Properties

Consistent with the neural network model, experimental results show reducing Cr and increasing W content improve yield strength. Strength in polycrystalline alloys may originate from the grain size, γ matrix and precipitate phase [34]. A similar grain size was observed for the three new alloys. Therefore, changes in the γ or γ' phases must have influenced yield strength, both these phases are strongly related to alloy chemistry. CALPHAD calculations at 650°C predicted that the volume fraction of γ' was approximately the same for the new alloys ($\sim$53%), this was supported by SEM measurements. Atom probe tomography found that γ' volume fraction was between

5-10% lower than CALPHAD predictions. Interestingly if CALPHAD calculations are conducted at the aging temperature (850°C) good agreement with APT measurement for γ' volume fraction is seen with D1, D2 and D3 expected to have 47.8%, 49.7% and 50.0% volume fraction of γ', respectively. This lower γ' volume fraction explains the lower than predicted yield strength for the new alloys and suggests that future alloy design calculations should be conducted using the aging temperature as opposed to the normal operating temperature of the component. The APT results showed γ' volume fraction increased with additions of W and removal of Cr. The partitioning coefficients (γ:γ') of W and Cr measured using APT show that W is a weak γ' former, whereas Cr strongly partitions to the γ phase. The increasing volume fraction of γ' as W was added to the alloy suggests that one way in which W provides strengthening in turbine disc alloys is by increasing precipitate strengthening. This is something which has not previously reported in the literature.

Increasing the levels of W and reducing the levels of Cr in the alloy improved creep resistance. This was in agreement with the ABD model for creep, as the creep merit index increased for the new alloys so did the measure creep life. The change in creep merit index was influenced mainly by the W content in the alloy. Based on the calculations and experimental results it can be concluded that additions of W were beneficial to creep resistance in the new alloys due to its low diffusivity in Ni. The new alloys had a higher creep merit index than RR1000, however, they performed worse in creep than RR1000. This poor creep life in comparison to RR1000 is mainly attributed to the γ' size and distribution. Previous work on turbine disc alloys has shown that creep resistance is sensitive to heat treatment [62]. The aging treatment given to the new alloys appeared to be coarsening in tertiary γ' significantly reducing creep resistance. Further optimisation of the heat treatment would be expected to improve the creep performance of these alloys. The role of grain boundary elements has also not been considered in the design of this alloy. Changes to the levels of C, B and Zr may influence

the creep resistance significantly.

5.5.2 Oxidation Resistance

The newly developed alloys had Cr concentrations ranging from 15.25 wt.% - 20.25 wt.%, this allowed for the effect of Cr on oxidation resistance to be studied. It was found that alloy D1 – containing the highest Cr content – performed best in oxidation. Alloys D2 and D3 showed very similar oxidation resistance. The alloys were selected using a model which ranked the oxidation resistance of alloys based on the activity of Cr, with a higher Cr activity corresponding to improved oxidation resistance. The oxidation resistance for a number of different alloys was measured experimentally, it was found that only a very weak correlation existed between Cr activity and oxidation resistance. A good correlation was observed between Cr content and oxidation resistance, however, there was still a spread in results suggesting that other factors must be influencing oxidation.

A strong relationship between Ti content and oxidation resistance was observed for all the alloys studied. It has been reported in previous work that Ti has a negative influence on the oxidation of Ni-Cr alloys [46] and also more complex multi-component superalloys [43, 47–51]. Results from EPMA work on the oxide scales for the three new alloys confirmed that there were significant quantities of Ti within the protective chromia oxide. It is believed that deleterious role of Ti on oxidation is due to an increase in cation vacancies resulting in faster chromium diffusion. This is described using the following,

$$\mathrm{TiO_{2(s)}} + \frac{3}{4}\mathrm{Cr^{x}_{Cr}} \rightarrow \mathrm{Ti^{\bullet}_{Cr}} + \frac{1}{3}\mathrm{V'''_{Cr}} + \frac{2}{3}\alpha - \mathrm{Cr_2O_{3(s)}} \tag{5.3}$$

where $Cr^{\mathrm{x}}_{\mathrm{Cr}}$ is a chromium ion in its normal state, $Ti^{\bullet}_{\mathrm{Cr}}$ is a Ti^{4+} in in a Cr^{3+} site, V'''_{Cr}

is a chromium vacancy site with three effective charges. The effect of other alloying elements on oxidation processes provides an explanation to why the activity of Cr model – which works for binary systems – is not sufficient for ranking the oxidation resistance of multi-component nickel-based superalloys. It was observed from experimental results that there is a strong correlation between Cr/Ti and the parabolic oxidation rate, Figure 5.16b. In absence of a physics based model that can relate alloy chemistry to oxidation resistance the author proposes that maximising the Cr/Ti ratio may be a method for selecting turbine disc alloys with improved oxidation resistance.

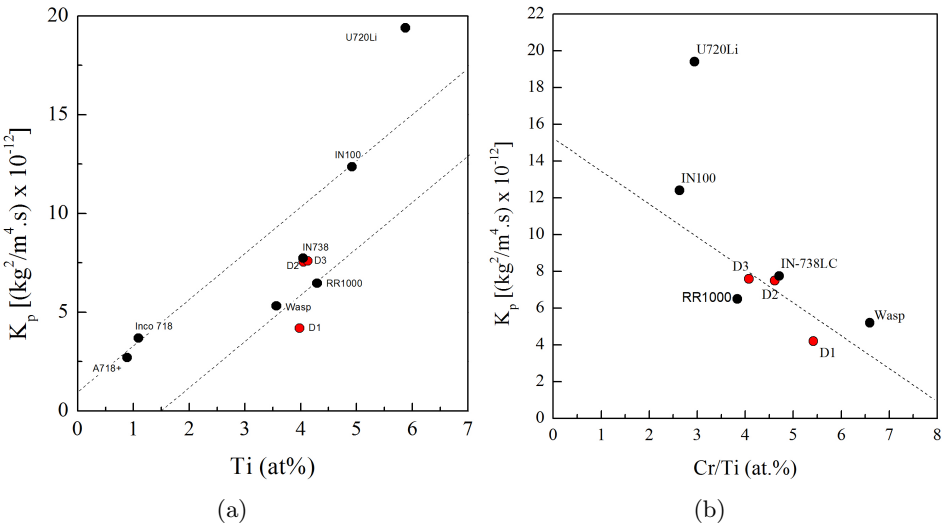


Figure 5.16: The parabolic oxidation rate for alloys D1-D3 and a number of commercial turbine disc alloys compared with, (a) titanium content in at.%, (b) Cr/Ti ratio in at.%

5.5.3 Considering the design for future alloys

The newly developed alloys did not meet the intended strength requirements. The design focused on the influence of γ' volume fraction on yield strength, it was expected that increased γ' volume fraction would improve yield strength. This design concept was supported by the neural network model, which predicted that alloy D3 would be approximately 100 MPa stronger than RR1000, the anticipated strength was not

realised. One possible explanation for why the neural network did not accurately predict strength is that the complex composition-microstructure interactions captured within the experimental data used to train the neural network. It is not possible for the neural network to distinguish between microstructural and chemical contributions to yield strength. Hence, the effect of alloy chemistry on yield strength could not be fully quantified by the neural network model. In comparison, the physics based model for yield strength presented in Chapter 4 clearly indicated how alloy chemistry influence microstructure and phase chemistry to achieve increased yield strength. By plotting RR1000 and alloys D1-D3 on the contour plots for strength calculated by the physics based strength model it is clear that although γ' volume fraction was increased APB energy was reduced resulting in little change to yield strength. Future alloy design must focus on increasing γ' volume fraction and APB energy in order to produce high strength alloys. This requires increased addition of Ti, Ta and Nb.

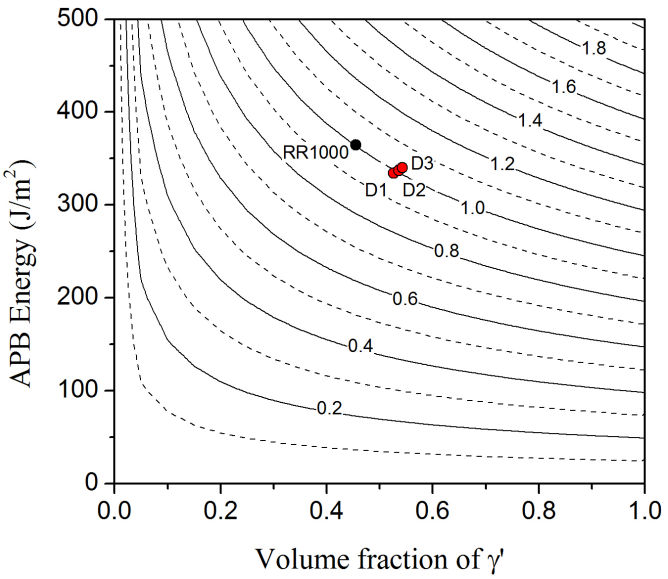


Figure 5.17: Yield Strength for RR1000 and alloys D1-D3 calculated using the DFT model described in chapter 4. Calculations conducted at 650 °C, contours for yield strength have been normalised to the modelled yield strength of RR1000.

The physics based model for yield strength identified that Ti is a potent strengthener

for turbine disc alloys. Oxidation work showed that Ti is detrimental to the oxidation resistance of chromia forming nickel-based superalloys. Therefore, a trade-off between oxidation resistance and yield strength exists. Furthermore, additions of Cr are found to increase the propensity to formation of deleterious phases, such as σ. Additions of Cr increase the propensity to TCP phases as γ' fraction increases, contributing further to the trade-off between oxidation resistance and yield strength. The modelling work presented in Chapters 3 and 4 show that there are possibilities to modify alloy chemistry to manage the trade-off between yield strength and oxidation resistance.

5.6 Conclusions

1. Three new polycrystalline nickel-based superalloys – their compositions isolated using the Alloys-by-Design approach of Chapter 3 – have been studied experimentally. The Cr/W ratio was varied in order to confer differing balance of mechanical properties and environmental resistance, e.g. oxidation.

2. The alloys were produced successfully using powder metallurgy methods, in such a way that the microstructure, yield strength, creep deformation behaviour and oxidation resistance could be studied in a rapid and economic fashion. Thus, the properties are likely to be representative of those found in the full-scale production process used for turbine disc manufacture.

3. Across the temperature range examined (from 20 to 800 deg C), the flow stress is found to be improved with reduced Cr and increased W levels respectively.

4. At 700°C and below, when yield occurs athermally, the yield stress is not improved substantially by increasing the volume fraction of γ'. Instead, it is proposed that the APB energy must be taken into account, such that the product of the APB energy and the square root of the volume fraction should be maximised for optimal

strength.

5. At 800°C when plasticity is likely to display sensitivity to the strain-rate, the yield strength is likely to have been improved by increasing the γ' fraction, as shown by comparison with data for the high-strength superalloy RR1000.

6. The creep behaviour of the new alloys is improved as the Cr/W ratio is reduced. This is in agreement with the modelling predictions which were used to design the alloys. This creep strengthening effect is attributed to W rather than Cr.

7. The creep resistance is nonetheless poor when compared with RR1000. This does not appear to be due to any precipitation of deleterious phases such as σ. The literature suggests that the creep performance may be sensitive to the range of γ' precipitate sizes present, so that further optimisation of the heat treatment used may be necessary.

8. The oxidation resistance of the newly developed alloys was studied for up to 100 hours. It was found that an increased Cr content improves the resistance to oxidation. The oxidation resistance is impaired by alloying with Ti.

6

Conclusions and Future Work

6.1 Conclusions

The aim of this research was to extend the capability of the Alloys-by-Design (ABD) model proposed by Reed et al. [1]. This computational method links thermodynamic calculations (CALPHAD) with so-called merit indices. The merit indices are physically based models which examine composition-property relationships for design relevant material properties e.g. yield strength or creep resistance. Understanding the relationship between composition and material behaviour enables the design of alloys where the chemistry has been optimised for a specific application. One can argue that this represents a paradigm shift from previous alloy design approaches which are typically reliant upon trial and error or statistical methods. The ABD approach was applied to the design the chemistry of a new nickel-based superalloy for turbine disc applications. Modelling predictions were verified by manufacturing and testing alloy compositions isolated using the ABD model.

In chapter 3 a compositional space within the Ni-Cr-Co-Al-Ti-Ta-Mo-W(-Zr-C-B) sys-

tem was studied using the ABD method. Microstructural characteristics, e.g. fraction of γ', γ' solvus temperature and merit indices e.g. yield strength and creep resistance were calculated for a large array of alloy compositions. The properties of the alloys in the compositional space were compared with commercial turbine disc alloys. The results suggest the existence of alloys with improved performance in comparison to the current state of the art. Composition-property maps were constructed to identify quantitative relationships between alloy chemistry and material properties. From this work it was possible to highlight how the composition of polycrystalline nickel-based superalloy must be controlled in order to deliver a truly optimal turbine disc alloy.

The ABD model proposed by Reed et al. [1] did not include a model for the yield strength of nickel-based superalloys. The design requirements for the turbine disc alloy identified yield strength as one of the most critical development goals. Initially, a neural network was used to model yield strength. However, the lack of training data and degree of interpolation/extrapolation motivated the development of a physics based model for yield strength. In Chapter 4 a model based upon hardening theory was proposed; a review of the literature concluded that strengthening in turbine disc alloys comes predominantly from the γ' phase. Precipitate strengthening was found to be dependent upon the product of the anti-phase boundary (APB) energy and square root of precipitate fraction. A CALPHAD method for calculating the APB energy in multi-component nickel-based superalloys was developed. The composition-dependent model showed that yield strength was strongly influenced by alloy chemistry. Additions of Ti, Ta and Nb were found to produce a potent strengthening effect by raising the APB energy. The accuracy of the method was evaluated by comparing CALPHAD and DFT calculations for APB energy in simple ternaries. By evaluating compositional design space using the new strength model and ABD model it was possible to identify the trade-offs encountered when designing a high strength alloys. The results indicated that there is a trade-off between yield strength, processing (γ' solvus temperature) and

stability of the γ' phase.

Chapter 5 was focused on the experimental validation of predictions made using the ABD model. Three new alloys – isolated using the ABD method – were manufactured using a scaled down version of the industrial powder processing route. Phase equilibrium calculations were validated using scanning electron microscopy (SEM) and atom probe tomography (APT). The tensile, creep and oxidation properties of the new alloys was also investigated. Good correlation between CALPHAD calculations and experimental measurements was observed. The alloys produced did not meet the intended design criteria; however, the information collected did provide information required to further refine the ABD model and the composition of the next generation turbine disc. The yield strength requirements were not met; a neural network model was used to predict the yield strength of these alloys. The strength model presented in Chapter4 identified that the chemistry had not been modified correctly to produce high strength. Oxidation resistance was studied for the new alloys and a number of commercially available turbine disc alloys. The results showed correlation between oxidation resistance and Cr/Ti ratio in the alloy. This is something that was not considered in the design of the new alloys and which will be incorporated into future design efforts.

Overall the ABD method has provided a useful insight into the challenges faced when trying to develop a nickel-based superalloy for turbine disc applications. The method is ultimately only as accurate as the underlying validity of the sub-models and databases, e.g. for thermodynamic properties. Good accuracy has been observed in thermodynamic databases and many gains have been made to improve the validity of the merit indices. The methods presented are already valuable, but will become increasingly so as the sub-models continue to improve.

6.2 Future Work

The knowledge gained from this research has been used for further design iterations of the turbine disc alloy. Results for three new alloy compositions (D1 - D3) are presented in this thesis; however, a further nine alloy compositions have been manufactured as part of this work, see Table 6.1. Research is ongoing to validate the performance of these alloys. The compositional range these alloys occupy is now subject to a UK patent application. The design rationale behind these compositions is detailed within the patent application, see Appendix 7.1. The performance of these alloys will be evaluated using the same experimental techniques presented in Chapter 5.

Table 6.1: The composition in wt.% of alloys developed using the ABD software, RR1000 is included for reference.

Alloy	Cr	Co	Mo	W	Al	Ti	Ta	Nb	C	B	Zr
RR1000	15.00	18.50	5.00	-	3.00	3.60	2.00	-	0.027	0.015	0.06
D1	20.25	19.00	-	1.00	3.94	3.45	2.00	-	0.027	0.015	0.06
D2	17.25	19.00	-	3.00	3.81	3.45	2.00	-	0.027	0.015	0.06
D3	15.25	19.00	-	5.00	3.69	3.45	2.00	-	0.027	0.015	0.06
D4	17.19	19.00	-	3.00	3.80	3.09	2.00	0.67	0.027	0.015	0.06
D5	17.14	19.00	-	3.00	3.79	2.74	2.00	1.33	0.027	0.015	0.06
D6	17.08	19.00	-	3.00	3.77	2.39	2.00	1.99	0.027	0.015	0.06
D7	12.85	16.67	-	3.25	3.81	4.25	2.00	-	0.027	0.015	0.06
D8	11.92	18.72	-	3.24	3.71	4.65	2.00	-	0.027	0.015	0.06
D9	11.32	18.64	-	3.23	3.32	5.06	2.00	-	0.027	0.015	0.06
D10	13.60	16.50	-	3.20	3.30	3.10	1.60	2.10	0.027	0.015	0.06
D11	14.40	14.30	-	3.20	3.30	2.70	3.10	1.60	0.027	0.015	0.06
D12	12.40	14.10	1.40	4.40	3.40	2.70	3.30	1.40	0.050	0.025	0.06

6.2.1 Strength Optimisation and Modelling

The newly developed alloys will undergo the same tensile test experiments as described in Chapter 5. The results from this experimental work will be used to validate the predictions made by the physics-based strength model described in Chapter 4. Figure

6.1 shows the predicted yield strength for the new alloys. It expected that alloys D8-D12 will have yield strength beyond current state-of-the-art turbine disc alloys such as ME3 or Alloy 10.

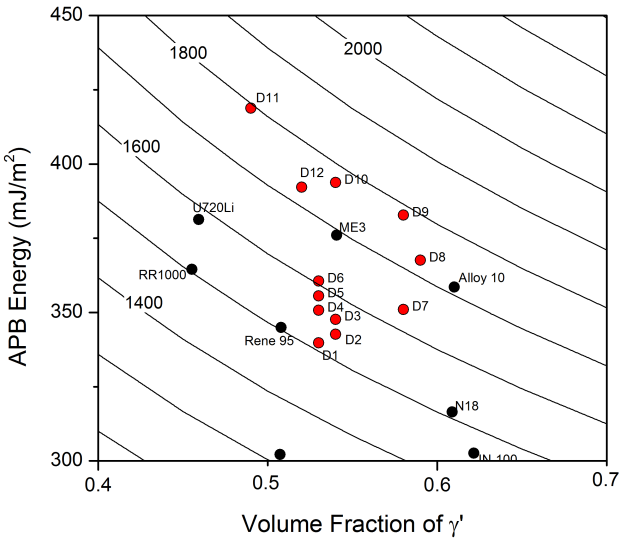


Figure 6.1: Contours for predicted yield strength (MPa) as a function of γ' volume fraction and APB energy. Red points indicate the calculated strength of alloys developed using the ABD method. Modelling predictions for a number of commercially available turbine disc materials are also included for reference.

Figure 6.2 shows tensile test results for alloys D1-D6. Alloys D5 and D6 have a yield strength greater than the alloys D1-D3 investigated in Chapter 5. The results correlate with strength model predictions, as D5 and D6 were predicted to be stronger than D1-D3. The red line on Figure 6.2 shows the minimum strength requirements for the new turbine disc alloy based on a Rolls-Royce design specification. Alloys D5 and D6 are within the design specification; these alloys also exhibit improved oxidation performance.

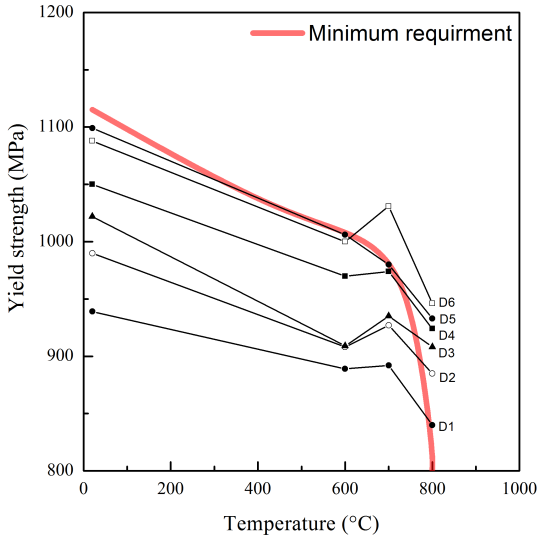


Figure 6.2: Yield strength as a function of temperature for the alloys D1-D6. The results are compared with the design requirement shown in red.

The optimisation of heat treatment has not been considered as part of the development of these materials, due to the limited availability of material. A reasonable quantity of forging remnants remain; however, this material is not suitable for traditional mechanical testing methods. It is proposed that the effect of heat treatment on these new alloys is investigated by using small scale mechanical testing. This would be conducted on a electrothermal mechanical testing machine (ETMT). This allows for a large number of tests using a very small quantity of material. Developing our understanding of these small scale mechanical tests is essential for accelerating the discovery and optimisation of materials. These methods can significantly reduced the cost and time associated with progressing an alloy from the design phase to deployment.

6.2.2 Grain Boundary Engineering

This research considered the use of computational modelling to optimise the levels of the major alloying elements. The work has shown that modifying the major elements

can significantly influence tensile properties and corrosion resistance. Although creep and fatigue are influenced by the major alloying elements, optimising the additions of grain boundary strengthening elements is expected to play a critical role for these properties. It is known that during creep, grain boundary sliding must be inhibited. These minor elements partition to the grain boundaries and form carbide and boride phases that can reduce grain boundary sliding. Fatigue cracks also propagate along grain boundaries, and carbide and boride phases may act as obstacles to fatigue crack propagation. Therefore, studying the relationship between grain boundary element additions, grain boundary character and fatigue/creep resistance is of critical importance to the ongoing development of a new turbine disc alloy.

It is proposed that alloys are manufactured with different levels of grain boundary elements. The levels of alloy additions would be selected using CALPHAD calculations to understand the fractions of grain boundary phases – for example, MC, $M_{23}C_6$ and M_3B_2 – in a similar manner to that applied to major elements in this work. Characterisation of these phases using high resolution techniques would be combined with traditional fatigue and creep testing. There is also the opportunity to observe small scale mechanical tests in-situ using a specially designed SEM stage; this would provide new understanding of the role of grain boundary phases during mechanical deformation.

6.2.3 Oxidation Modelling

The oxidation studies presented in Chapter 5 showed that the oxidation of chromia forming nickel-based superalloys was influenced by the Cr and Ti content. A strong correlation between Cr/Ti ratio (in at.%) and parabolic rate constant exists. Maximising the Cr/Ti ratio was proposed as a design concept for improving the oxidation resistance of the newly developed turbine disc alloy. This theory was tested in alloys D4-D6 listed in Table 6.1. Systematic replacement of Ti (in at.%) with Nb on a 1:1

basis was investigated. This allowed strength to be maintained whilst oxidation resistance to be improved. Initial studies into the oxidation behaviour of alloys D4-D6 has shown that increasing the Cr/Ti ratio will improve the oxidation resistance without detriment to the strength, Figure 6.3.

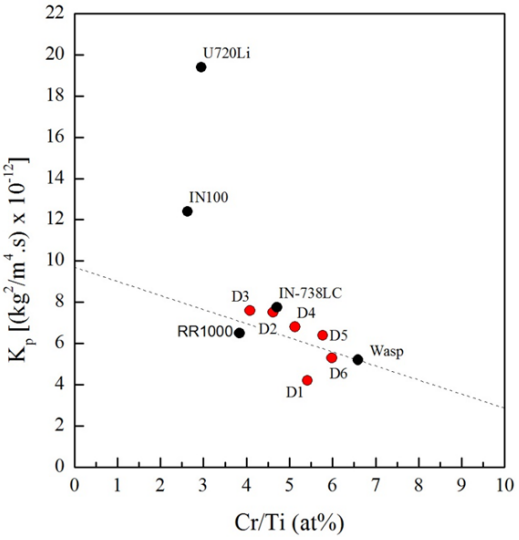


Figure 6.3: Correlation observed between Cr/Ti ratio and oxidation resistance for a number of turbine disc alloys. Oxidation studies were conducted at 800°C in air for 100 hours. The ABD alloys are highlighted in red.

As part of the future research oxidation studies will be conducted on all alloys listed in Table 6.1. These alloys have Cr/Ti ratio varying between 2.06 and 6.67. It is proposed to use a range of characterisation methods to understand the diffusion of Ti during oxidation. By coupling quantitative experimental techniques – for example atom probe tomography and electron-microprobe analysis – with computational modelling it is hoped that the physics behind oxidation of turbine disc alloys can be better understood, thus leading to the development of improved models which relate alloy composition to oxidation damage. The modelling of oxidation will be considered using both thermodynamic calculations and diffusion-based calculations.

6.2.4 Dwell Fatigue

The mechanism of dwell fatigue – sometimes referred to as creep fatigue – is still not well understood. In particular, the relationship between alloy composition and dwell fatigue has not been explored. The work presented in this thesis has shown that composition will influence a range of material behaviour, e.g. microstructural stability, creep resistance, tensile strength and oxidation resistance. This combination of properties is expected to influence the overall dwell fatigue performance of the alloy. Previous work on dwell fatigue has shown that oxidation may be driving crack growth. The alloys produced as part of this work exhibit different degrees of oxidation resistance; this allows for exploration of the relationship between oxidation resistance and dwell fatigue. The alloys also have varying degrees of strength and creep resistance. Thus determining the influence of these material properties in relation to dwell fatigue may also be important in developing an understanding of the relationship between alloy chemistry and dwell fatigue. As previously mentioned, the role of of grain boundary elements on fatigue resistance is also of interest for refining the design of turbine disc alloys.

6.2.5 Increasing the Scope of the Alloys-by-Design software

Currently the ABD method has been applied to the design of nickel-based superalloys in both single crystal and polycrystalline forms. Design work has been focused on turbine blade and disc applications for both aerospace and industrial gas turbines. As the capability of the method continues to improve, there is an opportunity to extend this method to other applications which use nickel-based superalloys, for example, nuclear power applications or high performance internal combustion engines. The ABD model has been developed in a way that makes it possible to adapt the algorithm for other alloy systems where thermodynamic databases exist, including Ti-, Fe-, Mg-, Al-. This

is an exciting opportunity as these alloys play a significant role in high performance applications, for example Ti- or Al- alloys in aerospace. However, there is the potential to design materials that will also be produced in significant quantities, for example development of Mg- or Fe- alloys for automotive applications.

The underlying principle of the Alloys-by-Design is to characterise large arrays of alloy compositions. In the period of this thesis over 3 million different alloys compositions – each alloy containing 10 alloying elements – were considered. For each alloy a minimum of 22 different variables were considered, producing 'Big Data' containing 3 million lines and 22 columns. A significant challenge of this research work has been managing, analysing and visualising such a complex data set. A key area of development for this method is the creation of more sophisticated methods of visualising and analysing data. This may be achieved through the use of advanced plotting packages and data-mining techniques.

Bibliography

[1] R. C. Reed, T. Tao, and N. Warnken. Alloys-by-Design: Application to nickel-based single crystal superalloys. *Acta Materialia*, 57(19):5898–5913, 2009. 3, 7, 38, 40, 41, 47, 48, 91, 97, 102, 135, 136

[2] R. C. Reed. *The superalloys: fundamentals and applications.* Cambridge University Press, 2006. 5, 10, 12, 13, 14, 15, 18, 20, 21, 22, 41, 44, 54, 55, 67, 90, 104

[3] T. M. Pollock and S. Tin. Nickel-based superalloys for advanced turbine engines: Chemistry, microstructure, and properties. *Journal of Propulsion and Power*, 22:361–374, 2006. 9, 12, 15, 58

[4] C.H. White, W. Betteridge, J. Heslop. *The nimonic alloys, Second Edition.* E. Arnold, 1959. 9

[5] T.P. Gabb, J. Gayda, I. Telesman, and P.T. Kantzos. US 6,974,508 B1 - Nickel base superalloy tubine disk, 2005. 9, 54

[6] C. T. Sims, N. S. Stoloff, and W. C. Hagel. Superalloys II. Wiley-Interscience, New York, NY1987. 10, 11, 14, 21, 105

[7] D. Furrer and H. Fecht. Ni-based superalloys for turbine discs. *JOM*, 51(1):14–17, 1999. 11, 12

[8] P. Caron and T. Khan. Evolution of ni-based superalloys for single crystal gas turbine blade applications. *Aerospace Science and Technology*, 3(8):513 – 523, 1999. 11, 12

[9] C.S Giggins and F.S. Pettit. Oxidation of ni-cr alloys between 800 and 1200c. *Tranactions of the Metallurgical Society of AIME*, 245:2495 – 2507, 1969. 11, 12, 28, 58, 59

[10] R. Jarrett and J. Tien. Effects of cobalt on structure, microchemistry and properties of a wrought nickel-base superalloy. *Metallurgical and Materials Transactions A*, 13:1021–1032, 1982. 11, 43, 105

[11] J. Gayda, P. Kantzos and J. Miller. Quench crack behavior of nickel-base disk superalloys. *Journal of Failure Analysis and Prevention*, 3:55–59, 2003. 11, 42, 57, 98, 104

[12] C.K.L. Davies, P.W. Davies and B. Wilshire. Effect of variations in stacking-fault energy on creep of nickel-cobalt alloys. *Philospohical Magazine*, 12(118):827–839, 1965. 11, 21

[13] H. Roth, C. Davis, and R. Thomson. Modeling solid solution strengthening in nickel alloys. *Metallurgical and Materials Transactions A*, 28:1329–1335, 1997. 11, 20

[14] C.M.F. Rae and R.C. Reed. The precipitation of topologically close-packed phases in rhenium-containing superalloys. *Acta Materialia*, 49(19):4113 – 4125, 2001. 12, 22, 105

[15] P.W. Keefe, S.O. Mancuso, and G.E. Maurer. Effects of heat-treatment and chemistry on the long-term phase-stability of a high-strength nickel-based superalloy. in R.A. MacKay, D.L. Anton, T. Khan, R.D. Kissinger, D.L. Klarstrom,

S.D. Antolovich, R.W. Stusrud, eds., *Superalloys 1992*, pages 487–496, 1992. 7th Internalional Symp on Superalloys, Champion, PA, Sep 20-24, 1992. 12, 42, 60, 104, 105

[16] R.C. Reed, M.P. Jackson, and Y.S. Na. Characterization and modeling of the precipitation of the sigma phase in udimet 720 and udimet 720li. *Metallurgical and Materials Transactions A*, 30(3):521–533, 1999. 12

[17] S. Ochial, Y. Oya, and T. Suzuki. Alloying behaviour of Ni_3Al, Ni_3Ga, Ni_3Si and Ni_3Ge. *Acta Metallurgica*, 32(2):289 – 298, 1984. 13, 95

[18] N. Baluc, H. P. Karnthaler, and M. J. Mills. TEM observation of the fourfold dissociation of superlattice dislocations and the determination of the fault energies in Ni_3(Al, Ta). *Philosophical Magazine A*, 64(1):137–150, 1991. 13, 55, 70, 72, 73, 87, 94

[19] N. Baluc, R. Schublin, and K. J. Hemker. Methods for determining precise values of antiphase boundary energies in Ni_3Al. *Philosophical Magazine Letters*, 64(5):327–334, 1991. 13, 72, 73, 87, 94

[20] A. Korner. Weak-beam study of superlattice dislocations moving on cube planes in Ni3(Al, Ti) deformed at room temperature. *Philosophical Magazine A*, 58(3):507–522, 1988. 13, 70, 72, 73, 87

[21] T. Kawabata, D. Shindo, and K. Hiraga. High-resolution TEM observations of superdislocations in Ni_3(Al, Ti). *Materials Transactions JIM*, 33(6):565–570, 1992. 13, 70, 72, 73, 87

[22] K. J. Hemker and M. J. Mills. Measurements of antiphase boundary and complex stacking fault energies in binary and B-doped Ni_3Al using TEM. *Philosophical Magazine A*, 68(2):305–324, 1993. 13, 70, 71, 72, 73

[23] E.C. Guo and F.J. Ma. The strengthening effect of niobium on Ni-Cr-Ti type wrought superalloy. In J.K. Tien, S.T. Wlodek, H. Marrow, M. Gell, G.E. Maurer. eds. *Superalloys 1980*, 4th Internalional Symp on Superalloys, Champion, PA, Sep 21-25, 1992. 13, 55, 73, 94

[24] B. Reppich. Some new aspects concerning particle hardening mechanisms in γ' precipitating ni-base alloysI. theoretical concept. *Acta Metallurgica*, 30(1):87 – 94, 1982. 13, 24, 83

[25] L Vegard. Die röntgenstrahlen im dienste der erforschung der materie. *Z Kistallogr*, 67:239–259, 1928. 14

[26] R.A. Ricks, A.J. Porter, and R.C. Ecob. The growth of γ' precipitates in nickel-base superalloys. *Acta Metallurgica*, 31(1):43 – 53, 1983. 14

[27] A.K. Jena and M.C. Chaturvedi. The role of alloying elements in the design of nickel-base superalloys. *Journal of Materials Science*, 19(10):3121–3139, 1984. 14

[28] L. Xiao, M.C. Chaturvedi, and D.L. Chen. Effect of boron on the low-cycle fatigue behavior and deformation structure of Inconel 718 at 650°C. *Metallurgical and Materials Transactions A*, 35(11):3477–3487, 2004. 14, 15

[29] F.T. Furillo, J.M. Davidson, J.K. Tien, and L.A. Jackman. The effects of grain boundary carbides on the creep and back stress of a nickel-base superalloy. *Materials Science and Engineering*, 39(2):267 – 273, 1979. 14

[30] R.J. Mitchell, C.M.F. Rae, and S. Tin. Grain boundary transformations during isothermal exposure of powder metallurgy nickel base superalloys for turbine disc applications. *Materials science and technology*, 21(1):125–132, 2005. 15

[31] M. G. Benz. Preparation of clean alloys. In C. L. Briant, editor, *Impurities in Engineering Materials: Impact, Reliability and Control*, pages 31–47. Marcel Dekker Inc., New York, 1999. 16, 17

[32] J. C. Williams and E. A. Starke. Progress in structural materials for aerospace systems. *Acta Materialia*, 51(19):5775–5799, 2003. 18, 20

[33] M.P. Jackson and R.C. Reed. Heat treatment of Udimet 720Li: the effect of microstructure on properties. *Materials Science and Engineering: A*, 259(1):85 – 97, 1999. 20

[34] R.W. Kozar, A. Suzuki, W.W. Milligan, J.J. Schirra, M.F. Savage, and T.M. Pollock. Strengthening mechanisms in polycrystalline multimodal nickel-base superalloys. *Metallurgical and Materials Transactions A*, 40:1588–1603, 2009. 21, 23, 55, 56, 96, 128

[35] B. Reppich, P. Schepp, and G. Wehner. Some new aspects concerning particle hardening mechanisms in γ' precipitating nickel-base alloysII. experiments. *Acta Metallurgica*, 30(1):95 – 104, 1982. 24, 83

[36] B. Reppich. *Particle Strengthening*, pages 311–357. Weinham Germany: VCH, 1993. 24, 83

[37] N. Birks, G. H. Meier, and F. S. Pettit. *Introduction to the high temperature oxidation of metals*. Cambridge University Press, 2006. 25, 27

[38] C.S. Tedmon. The effect of oxide volatilization on the oxidation kinetics of Cr and Fe-Cr alloys. *Journal of the Electrochemical Society*, 113(8):766–768, 1966. 27

[39] R. Prescott and M.J. Graham. The formation of aluminum oxide scales on high-temperature alloys. *Oxidation of Metals*, 38(3-4):233–254, 1992. 27

[40] G.C. Wood and F.H. Stott. Oxidation of alloys. *Materials Science and Technology*, 3(7):519–530, 1987. 28, 29

[41] C.S. Giggins and F. S. Pettit. Oxidation of Ni-Cr-Al alloys between 1000c and 1200c. *Journal of Electrochemical Society*, 118:1782 – 1790, 1971. 30, 31, 32, 58

[42] F.I. Wei and F.H. Stott. The influence of aluminium on the oxidation of a Cr_2O_3-forming nickel-chromium alloy. *Reactivity of Solids*, 6(23):129 – 144, 1988. 32

[43] S. Cruchley, H.E. Evans, M.P. Taylor, M.C. Hardy, and S. Stekovic. Chromia layer growth on a ni-based superalloy: Sub-parabolic kinetics and the role of titanium. *Corrosion Science*, 75(0):58 – 66, 2013. 32, 33, 34, 35, 130

[44] N. Hussain, K.A. Shahid, I.H. Khan, and S. Rahman. Oxidation of high-temperature alloys (superalloys) at elevated temperatures in air. II. *Oxidation of Metals*, 43(3-4):363–378, 1995. 33

[45] J. Jones and D.J.C. MacKay. Neural network modelling of the mechanical properties of nickel base superalloys. In R.D. Kissinger, D.J. Deye, D.L. Anton, A.D Cetel, M.V. Nathal, T.M. Pollock D.A. Woodford, eds, *Superalloys 1996*, 417–424. 8th International Symposium on Superalloys, Champion, PA, Sept 22-26, 1996. 34, 44, 56, 105

[46] H. Nagai and M. Okabayashi. Deleterious effect of Ti addition on the oxidation resistance of Ni–20Cr alloy. *Trans. Jpn. Inst. Met.*, 22(10):691–698, 1981. 34, 130

[47] J. Chen, P. Rogers, and J. Little. Oxidation behavior of several chromia-forming commercial nickel-base superalloys. *Oxidation of Metals*, 47:381–410, 1997. 34, 35, 46, 58, 59, 130

[48] H. Buscail, S. Perrier, and C. Josse. Oxidation mechanism of the Inconel 601 alloy at high temperatures. *Materials and Corrosion*, 62(5):416–422, 2011. 34, 35, 130

[49] F.J. Liu, M.C. Zhang, J.X. Dong, and Y.W. Zhang. High-temperature oxidation of FGH96 p/m superalloy. *Acta Metallurgica Sinica (English Letters)*, 20(2):102 – 110, 2007. 34, 35, 130

[50] C.L. Angerman. Long-term oxidation of superalloys. *Oxidation of Metals*, 5(2):149–167, 1972. 34, 35, 130

[51] F. Abe, H. Araki, H. Yoshida, and M. Okada. The role of aluminum and titanium on the oxidation process of a nickel-base superalloy in steam at 800c. *Oxidation of Metals*, 27(1-2):21–36, 1987. 34, 35, 36, 130

[52] C. Ducrocq, A. Lasalmonie, and Y. Honnorat. N18, a new damage tolerant pm superalloy for high temperature. In S. Reichman, D. Duhl, G. Maurer, S. Antolovich, C. Lund. eds., *Superalloys 1988*, 1988. 6th Internalional Symp on Superalloys, Champion, PA, Sep 18-22, 1988. 38

[53] J.Y. Guedou, J.C. Lautridou, and Y. Honnorat. N18, pm superalloy for disks - development and applications. In R.A. MacKay, D.L. Anton, T. Khan, R.D. Kissinger, D.L. Klarstrom, S.D. Antolovich, R.W. Stusrud. eds., *Superalloys 1992*, 267–276, 1992. 7th Internalional Symp on Superalloys, Champion, PA, Sep 20-24, 1992. 38, 44

[54] C.J. Small and N. Saunders. Application of calphad techniques in the development of a new gas-turbine disk alloy. *MRS Bulletin*, page 22, 1999. 40

[55] F. Tancret, H.K.D.H. Bhadeshia, and D.J.C. MacKay. Design of a creep resistant nickel base superalloy for power plant applications - part 1 - mechanical properties modelling. *Materials Science and Technology*, 19(3):283–290, 2003. 40, 56

[56] T. Yokokawa, H. Saeki, Y. Fukuyama, T. Yoshida, and H. Harada. The virtual gas turbine system for alloy assesment. In K.A. Green, T.M. Pollock, H. Harada, T.E. Howson, R.C. Reed, J.J. Schirra, and S. Walston. eds., *Superalloys 2004*, pages 859–866. 10th International Symposium on Superalloys, Champion, PA, SEP 19-23, 2004. 40

[57] *Thermotech Ni-data version 7. Thermotech Ltd./Sente Software Ltd., Surrey Technology Centre, 40 Occam Road, GU2 7YG, Uk.* 42

[58] B. Seiser, R. Drautz, and D.G. Pettifor. TCP phase predictions in Ni-based superalloys: Structure maps revisited. *Acta Materialia*, 59(2):749 – 763, 2011. 42

[59] J.Y. Guedou, I. Augustins-Lecallier, L. Naze, P. Caron, and D. Locq. Development of a new fatigue and creep resistant pm nickel-base superalloy for disk applications. In P. Caron, T.P. Gabb, M.G. Fahrmann, E.S. Huron, R.C. Reed, K.A. Green, eds, *Superalloys 2008*, pages 21–30. 11th International Symposium on Superalloys, Champion, PA, Sept 14-18, 2008. 43, 44, 90

[60] J. Radavich, D. Furrer, T. Carneiro, and J. Lemsky. The microstructure and mechanical properties of EP741NP powder metallurgy disc material. In R.C. Reed, K.A. Green, P. Caron, T.P. Gabb, M.G. Fahrmann, and E.S. Huron, editors, *Superalloys 2008*, pages 63–72. 11th International Symposium on Superalloys, Champion, PA, SEP 14-18, 2008. 43

[61] T.P. Gabb, I. Telesman, and P.T. Kantzos. US6974508 - nickel base superalloy turbine disk, 2005. 43, 44

[62] D. Locq, M. Marty, and P. Caron. Optimisation of the mechanical properties of a new pm superalloy for disk applications. In R.R Bowman, K.A. Green, M. McLean, S.L. Olson, J.J. Schirra, T.M. Pollock, R.D. Kissinger, eds, *Superalloys*

2000, pages 395–403. 9th International Symposium on Superalloys, Champion, PA, Sept 17-21, 2000. 43, 44, 55, 129

[63] S.J. Hessel, W. Voice, A.W. James, S.A. Blackham, C.J. Small, and M.R. Winstone. US 6,132,527 - nickel alloy for turbine engine components, 2000. 43

[64] M. J. Donachie. *Superalloys: A Technical Guide*. ASM, 2002. 43, 44

[65] C.Y. Cui, Y.F. Gu, D.H. Ping, and H. Harada. Microstructural evolution and mechanical properties of a ni-based superalloy, TMW-4. *Metallurgical and Materials Transactions A*, 40:282–291, 2009. 10.1007/s11661-008-9746-4. 43

[66] R.M. Neal. *Software for Flexible Bayesian Modelling and Markov Chain Sampling*. PhD thesis. 43

[67] H.K.D.H. Bhadeshia. Neural networks in materials science. *ISIJ Ineternational*, 39(10):966–979, 1999. 44

[68] E.S. Huron, K.R. Bain, D.P. Mourer, and T. Gabb. Development of high temperature capability p/m disk superalloys. In R.C. Reed, K.A. Green, P. Caron, T.P. Gabb, M.G. Fahrmann, and E.S. Huron, editors, *Superalloys 2008*, pages 181–189. 11th International Symposium on Superalloys, Champion, PA, SEP 14-18, 2008. 44, 90

[69] Y. Gu, H. Harada, C. Cui, D. Ping, A. Sato, and J. Fujioka. New Ni-Co-base disk superalloys with higher strength and creep resistance. *Scripta Materialia*, 55(9):815–818, 2006. 44

[70] Furrer D. Radavich J. Assessment of russian p/m superalloy EP741NP. In H. Harada, T.E. Howson, R.C. Reed, J.J. Schirra, S. Walston, K.A. Green, T.M. Pollock, eds, *Superalloys 2004*, pages 381–390. 10th International Symposium on Superalloys, Champion, PA, SEP 19-23, 2004. 44, 90

[71] Nickel Development Institute Birmingham England. High temperature high strength nickel base alloys. *High Temperature High Strength Nickel Base Alloys*. 44

[72] W.B. Kent. Development of an extra high strength powder metallurgy nickel base superalloy. *Nasa Lewis Research Centre*, 1977. 44, 90

[73] J. Gayda. The effect of tungsten and niobium additions on disk alloy ch98. *Nasa Glenn Research Centre*, 2003. 44

[74] J. Gayda. High temperature fatigue crack growth behaviour of alloy 10. *Nasa Glenn Research Centre*, 2001. 44

[75] D. Ellis, T.P. Gabb, and A. Garg. Microstructural evaluation of KM4 and SR3 samples subjected to various heat treatments. *Nasa Glenn Research Centre*, 2004. 44, 90

[76] T.P. Gabb, P.T. Kantzos, and K. O'Connor. Characterisation of the temperature capabilities of advanced disk alloy ME3. *Nasa Glenn Research Centre*, 2002. 44

[77] J. R. Davis. *Nickel, Cobalt and their Alloys*. ASM International, Handbook Comittee, 2000. 44

[78] A. Encinas-Oropes, G. L. Drew, M. C. Hardy, A. J. Leggett, J. R. Nicholls, and N. J. Simms. Effects of oxidation and hot corrosion in a nickel disc alloy. In R.C. Reed, K.A. Green, P. Caron, T.P. Gabb, M.G. Fahrmann, and E.S. Huron, editors, *Superalloys 2008*, pages 181–189. 11th International Symposium on Superalloys, Champion, PA, SEP 14-18, 2008. 46, 59

[79] L. Zheng, M. Zhang, and J. Dong. Oxidation behavior and mechanism of powder metallurgy Rene95 nickel based superalloy between 800 and 1000c. *Applied Surface Science*, 256(24):7510 – 7515, 2010. 46, 59

[80] K.H. Al-hatab, M. Al-bukhaiti, U Krupp, and M. Kantehm. Cyclic oxidation behavior of IN 718 superalloy in air at high temperatures. *Oxidation of Metals*, 75:209–228, 2011. 10.1007/s11085-010-9230-6. 46, 59

[81] C. Wagner. On the theory of scaling reactions. *Z. Phys. Chem.*, 21:25, 1933. 46

[82] M. S. A. Karunaratne, P. Carter, and R. C. Reed. Interdiffusion in the face-centred cubic phase of the Ni-Re, Ni-Ta and Ni-W systems between 900 and 1300 degrees C. *Material Science and Engineering A*, 281(1-2):229–233, 2000. 48

[83] M. S. A. Karunaratne and R. C. Reed. Interdiffusion of the platinum-group metals in nickel at elevated temperatures. *Acta Materialia*, 51(10):2905–2919, 2003. 48

[84] M. Kramar, C.L. Fu, A. Janotti, and R.C. Reed. Diffusion rates of 3d transition metal solutes in nickel by first-principles calculations. *Acta Materialia*, 53(8):2369 – 2376, 2005. 48

[85] M.C. Hardy, B. Zirbel, G. Shen, and R. Shankar. Developing damage tolerance and creep resistance in a high strength nickel alloy for disc applications. In H. Harada, T.E. Howson, R.C. Reed, J.J. Schirra, S. Walston, K.A. Green, T.M. Pollock, eds, *Superalloys 2004*, pages 83–90. 10th International Symposium on Superalloys, Champion, PA, SEP 19-23, 2004. 52, 60, 102

[86] D. P. Mourer, E.S. Huron, K. R. Bain, E. Montero, P.L. Reynolds, and J.J Schirra. US 6,521,175 B1 - superalloy optimiszedfor high performance in high-pressure tubine disks, 2003. 53, 58

[87] Y. Mishima, S. Ochiai, M. Yodogawa, and T. Suzuki. Mechanical-Properties of Ni_3Al with ternary arritions of transition metal elements. *Transactions of the Japan Insititute of Metals*, 27(1):41–50, 1986. 53

[88] J. Gayda and T.P. Gabb. The effect of tungsten additions on disk alloy ch98. *Nasa Glenn Research Centre*, 2003. 53, 58

[89] W.D. Cao. Us 6,730,264 b2 - nickel-base alloy, 2004. 54

[90] E. Nembach. The high temperature peak of the yield strength of γ' strengthened superalloys. *Materials Science and Engineering: A*, 429(1-2):277–286, 2006. 55

[91] D. Raynor and J. M. Silcock. Strengthening mechanisms in γ' precipitating alloys. *Metal Science*, 4(1):121–130, 1970. 55

[92] I. Di Martino, J. W. Brooks, P. A. S. Reed, P. Holdway, and A. Wisbey. Adaptive numerical modelling of high temperature strength, creep and fatigue behaviour in ni-based superalloys. *Materials Science and Technology*, 23(12):1402–1407, 2007. 56

[93] M. Chandran and S. K. Sondhi. First-principle calculation of apb energy in ni-based binary and ternary alloys. *Modelling and Simulation in Materials Science and Engineering*, 19(2):1 – 7, 2011. 56

[94] A. P. Miodownik and N. Saunders. The calculation of apb energies in $L1_2$ compounds using a thermodynamic database. In *Applications of Thermodynamics in the Synthesis and Processing of Materials, eds. P. Nash and B. Sundman(Warrendale, PA:TMS, 1995)*, 1995. 56

[95] R.R. Unocic, G.B. Viswanathan, P.M. Sarosi, S. Karthikeyan, J. Li, and M.J. Mills. Mechanisms of creep deformation in polycrystalline ni-base disk superalloys. *Materials Science and Engineering: A*, 483:25 – 32, 2008. 58

[96] A. Sato, Y.L. Chiu, and R.C. Reed. Oxidation of nickel-based single-crystal superalloys for industrial gas turbine applications. *Acta Materialia*, 59(1):225 – 240, 2011. 59

[97] Q.Z Chen, N Jones, and D.M Knowles. The microstructures of base/modified rr2072 sx superalloys and their effects on creep properties at elevated temperatures. *Acta Materialia*, 50(5):1095 – 1112, 2002. 63

[98] E.S. Huron, K.R. Bain, D.P. Mourer, J.J. Schirra, P.L. Reynolds, and E.E. Montero. The influence of grain boundary elements on properties and microstructures of p/m nickel base superalloys. In H. Harada, T.E. Howson, R.C. Reed, J.J. Schirra, S. Walston, K.A. Green, T.M. Pollock, eds, *Superalloys 2004*, pages 73–81. 10th International Symposium on Superalloys, Champion, PA, SEP 19-23, 2004. 63, 105

[99] T.J. Garosshen, T.D. Tillman, and G.P. McCarthy. Effects of B, C, and Zr on the structure and properties of a p/m nickel base superalloy. *Metallurgical Transactions A*, 18(1):69–77, 1987. 63

[100] J. Miao, T.M. Pollock, and J. W. Jones. Microstructural extremes and the transition from fatigue crack initiation to small crack growth in a polycrystalline nickel-base superalloy. *Acta Materialia*, 60(67):2840 – 2854, 2012. 66

[101] D.M. Collins, L. Yan, E.A. Marquis, L.D. Connor, J.J. Ciardiello, A.D. Evans, and H.J. Stone. Lattice misfit during ageing of a polycrystalline nickel-base superalloy. *Acta Materialia*, 61(20):7791 – 7804, 2013. 66

[102] S. Keshavarz and S. Ghosh. Multi-scale crystal plasticity finite element model approach to modeling nickel-based superalloys. *Acta Materialia*, 61(17):6549 – 6561, 2013. 66

[103] N. Zhou, D.C. Lv, H.L. Zhang, D. McAllister, F. Zhang, M.J. Mills, and Y. Wang. Computer simulation of phase transformation and plastic deformation in IN718 superalloy: Microstructural evolution during precipitation. *Acta Materialia*, 65(0):270 – 286, 2014. 66

[104] L. Kovarik, R. R. Unocic, J. Li, P. Sarosi, C. Shen, Y. Wang, and M. J. Mills. Microtwinning and other shearing mechanisms at intermediate temperatures in Ni-based superalloys. *Progress in Materials Science*, 54(6):839–873, 2009. 66

[105] P.A. Flinn. Theory of deformation in superlattices. *Trans TMS-AIME*, 218(1):145–154, 1960. 69

[106] C. N. Yang. A generalization of the quasi-chemical method in the statistical theory of superlattices. *The Journal of Chemical Physics*, 13(2):66–76, 1945. 70

[107] R. Peierls. Statistical theory of superlattices with unequal concentrations of the components. *Proceedings of the Royal Society of London. Series A - Mathematical and Physical Sciences*, 154(881):207–222, 1936. 70

[108] J. M. Cowley. An approximate theory of order in alloys. *Phys. Rev.*, 77:669–675, 1950. 70

[109] Y.Q. Sun. *Basic Mechanical Proerties adnd Lattice Defects of Intermetallic Compounds*. John Wiley & Sons Ltd, 1995. 70

[110] H.P. Karnthaler, E.Th. Mhlbacher, and C. Rentenberger. The influence of the fault energies on the anomalous mechanical behaviour of Ni_3Al alloys. *Acta Materialia*, 44(2):547 – 560, 1996. 70, 71, 73

[111] D. M. Dimiduk, A. W. Thompson, and J. C. Williams. The compositional dependence of antiphase-boundary energies and the mechanism of anomalous flow in Ni_3Al alloys. *Philosophical Magazine A*, 67(3):675–698, 1993. 70, 71, 72, 73

[112] T. Kruml, E. Conforto, B. Lo Piccolo, D. Caillard, and J.L. Martin. From dislocation cores to strength and work-hardening: a study of binary Ni_3Al. *Acta Materialia*, 50(20):5091 – 5101, 2002. 70, 71, 73, 93, 95

[113] J. Douin and P. Veyssire. On the effect of deviation from stoichiometry on the deformation microstructure of binary Ni_3Al. *Philosophical Magazine A*, 64(4):807–817, 1991. 70, 71, 73

[114] P. Veyssiere, J. Douin, and P. Beauchamp. On the presence of super lattice intrinsic stacking faults in plastically deformed Ni_3Al. *Philosophical Magazine A*, 51(3):469–483, 1985. 70, 71, 73

[115] J. Douin, P. Veyssire, and P. Beauchamp. Dislocation line stability in Ni_3Al. *Philosophical Magazine A*, 54(3):375–393, 1986. 70, 71, 73

[116] H. Yu and H.P. Karnthaler. The effect of composition on the fault energies of intermetallic alloys Ni_3(Al, B). *Materials & Design*, 14(1):69 – 71, 1993. 70, 72, 73

[117] Bontemps-Neveu C. PhD thesis, Universute Paris Sud (Orsay), France, 1991. 70, 72, 73

[118] S. S. Ezz and P. B. Hirsch. The strain rate sensitivity of the flow stress and the mechanism of deformation of single crystals of Ni_3(Al Hf)B. *Philosophical Magazine A*, 69(1):105–127, 1994. 70, 72, 73

[119] T. Kruml, J. L. Martin, and J. Bonneville. On the strengthening of Ni_3Al by hafnium additions. *Philosophical Magazine A*, 80(7):1545–1566, 2000. 70, 72, 73

[120] J. Sun, C.S. Lee, J.K.L. Lai, and J.S. Wu. Dislocation dissociations and fault energies in Ni_3Al alloys doped with palladium. *Intermetallics*, 7(12):1329 – 1335, 1999. 70, 72, 73

[121] D. Baither, C. Rentenberger, H. P. Karnthaler, and E. Nembach. Three alternative experimental methods to determine the antiphase-boundary energies of the

γ' precipitates in superalloys. *Philosophical Magazine A*, 82(9):1795–1805, 2002. 70, 73, 105

[122] John Price Hirth and Jens Lothe. *Theory of dislocations.* John Wiley and Sons, Inc.,, 1982. 71

[123] D. J. H. Cockayne, I. L. F. Ray, and M. J. Whelan. Investigations of dislocation strain fields using weak beams. *Philosophical Magazine*, 20(168):1265–1270, 1969. 71

[124] S. M. Foiles and M. S. Daw. Application of the embedded atom method to Ni_3Al. *Journal of Materials Research*, 2:5–15, 1 1987. 74

[125] Y. Mishin. Atomistic modeling of the γ and γ'-phases of the nial system. *Acta Materialia*, 52(6):1451 – 1467, 2004. 74

[126] S. P. Chen, D. J. Srolovitz, and A. F. Voter. Computer simulation on surfaces and [001] symmetric tilt grain boundaries in Ni, Al, and Ni_3Al. *Journal of Materials Research*, 4:62–77, 1 1989. 74

[127] M.H. Yoo, C.L. Fu, and J.A. Horton. Crack-tip dislocations and fracture behavior in Ni_3Al and Ni_3Si. *Materials Science and Engineering: A*, 176(12):431 – 437, 1994. 74

[128] N. M. Rosengaard and H. L. Skriver. *Ab initio* study of antiphase boundaries and stacking faults in $L\,1_2$ and DO_{22} compounds. *Phys. Rev. B*, 50:4848–4858, Aug 1994. 74

[129] A.T. Paxton and Y.Q. Sun. The role of planar fault energy in the yield anomaly in $L1_2$ intermetallics. *Philosophical Magazine A*, 78(1):85–104, 1998. 74

[130] O.N. Mryasov, Yu.N. Gornostyrev, M. van Schilfgaarde, and A.J. Freeman. Superdislocation core structure in $L1_2$ Ni_3Al, Ni_3Ge and Fe_3Ge: Peierlsnabarro

analysis starting from ab-initio GSF energetics calculations. *Acta Materialia*, 50(18):4545 – 4554, 2002. 74

[131] G. Schoeck, S. Kohlhammer, and M. Fahnle. Planar dissociations and recombination energy of [110] superdislocations in Ni_3Al: Generalized peierls model in combination with ab initioelectron theory. *Philosophical Magazine Letters*, 79(11):849–857, 1999. 74

[132] A.T. Paxton. *Electron Theroy in Alloy Design.* The institue of Materials, 1992. 74

[133] K. V. Vamsi and S. Karthikeyan. *Effect of Off-Stoichiometry and Ternary Additions on Planar Fault Energies in Ni_3Al*, pages 521–530. John Wiley & Sons, Inc., 2012. 74, 75, 76

[134] M. Chandran and S. Sondhi. First-principle calculation of apb energy in ni-based binary and ternary alloys. *Modelling and Simulations in Materials Science and Engineering*, 19:025008, 2011. 74, 76

[135] G. Inden. Determination of interchange energies from thermodynamic and structural data. *Le Journal de Physique Colloques*, 38(C7):7–7, 1977. 77

[136] A. Bieber and F. Gautier. Are multiatom interactions relevant for the determination of stability of ordered structures and short range order in binary transition metal alloys? *Journal of the Physical Society of Japan*, 53(0):206l–2074, 1984. 77

[137] A. Bieber and F. Gautier. Multiatom interactions, order and stability in binary transition metal alloys. *Zeitschrift für Physik B Condensed Matter*, 57(4):335–343, 1984. 77

[138] G. Inden, S. Bruns, and H. Ackermann. Antiphase boundary energies in ordered f.c.c. alloys. *Philosophical Magazine A*, 53:87–100, 1986. 77

[139] N.J. Saunders A.P. Miodownik. The calculation of apb energies in $L1_2$ compounds using a thermodynamic database. In *TMS Fall Meeting 1994*, 1994. 78, 81

[140] M. Sluiter, P. Turchi, F. Pinski, and G. Stocks. Theoretical study of phase stability in Ni-Al and Ni-Ti alloys. *Journal of Phase Equilibria*, 13:605–611, 1992. 78

[141] F. Cardellini, F. Cleri, G. Mazzone, A. Montone, and V. Rosato. Experimental and theoretical investigation of the order-disorder transformation in Ni_3Al. *Journal of Materials Research*, 8:2504–2509, 9 1993. 81

[142] S.R. Harris, D.H. Pearson, C.M. Garland, and B. Fultz. Chemically disordered Ni_3Al synthesized by high vacuum evaporation. *Journal of Materials Research*, 6:2019–2021, 9 1991. 81

[143] C. Colinet, P. Hicter, and A. Pasturel. Tight-binding calculations of the Ni-Al phase diagram. *Phys. Rev. B*, 45:1571–1580, 1992. 81

[144] A. Zunger, S. H. Wei, L. G. Ferreira, and J. E. Bernard. Special quasirandom structures. *Physical Review Letters*, 65(3):353–356, 1990. 82

[145] S.-H. Wei, L. G. Ferreira, J. E. Bernard, and A. Zunger. Electronic properties of random alloys: Special quasirandom structures. *Physical Review B*, 42(15):9622–9649, 1990. 82

[146] A. van de Walle and G. Ceder. Automating First-Principles Phase Diagram Calculations. *Journal of Phase Equilibria*, 23:348–359, 2002. 82

[147] G. Kresse and J. Furthmuller. Efficient iterative schemes for ab initio total-energy calculations using a plane-wave basis set. *Physical Review B*, 54(16):11169–11186, 1996. 82

[148] J. Hafner. Materials simulations using VASP - a quantum perspective to materials science. *Computer Physics Communications*, 177(1-2):6–13, 2007. 82

[149] P. E. Blochl. Projector augmented-wave method. *Physical Review B*, 50(24):17953–17979, 1994. 82

[150] G. Kresse and D. Joubert. From ultrasoft pseudopotentials to the projector augmented-wave method. *Physical Review B*, 59(3):1758–1775, 1999. 82

[151] J. P. Perdew, K. Burke, and M. Ernzerhof. Generalized gradient approximation made simple. *Physical Review Letters*, 77(18):3865–3868, 1996. 82

[152] D.J. Crudden, B. Raeisinia, N. Warnken, and R.C. Reed. Analysis of the chemistry of nickel based turbine disk superalloys using an alloys-by-design modelling approach. *Metallurgical and Materials Transactions A*, 44:2418–2430, 2013. 91, 102

[153] C.Y. Cui, A. Sato, Y.F. Gu, D.H. Ping, and H. Harada. Phase stability and yield stress of ni-base superalloys containing high Co and Ti. *Metallurgical and Materials Transactions A*, 37(11):3183–3190, 2006. 105

[154] W.S. Rasband. *ImageJ, U. S. National Institutes of Health, Bethesda, Maryland, USA, http://imagej.nih.gov/ij/, 1997-2014.* 109

7

Appendix

7.1 Appendix A - Patent for ABD Alloys

ABSTRACT

A Nickel Based Alloy Composition

A nickel based alloy composition comprising, by atomic per cent, between 12 and 15% of elements from the group consisting of aluminium, titanium, tantalum and niobium, between 0.8 and 1.8% tungsten, between 5 and 8% aluminium, at least 28% of elements from the group consisting of molybdenum, tungsten, chromium and cobalt, wherein the atomic ratio of the sum of titanium, tantalum and niobium to aluminium is between 0.6 and 1.1, and wherein the composition comprises less than 1% molybdenum, the balance being nickel save for incidental impurities.

(Table 2)

A Nickel Based Alloy Composition

Field of the Invention

The present invention relates to a nickel based alloy composition, as well as a method of forming an article from a nickel based alloy, a heat treatment method for producing forgings of a nickel based alloy, a turbine disc comprising a nickel based alloy, and a gas turbine engine comprising a turbine disc.

Background to the Invention

Table 1 defines prior nickel based compositions suitable for use in rotor discs for gas turbine engines, such as high pressure compressor and turbine discs. These include the following compositions described in the corresponding documents: Udimet™ 720Li (described in US 4,093,476); RR1000™ (described in US 6,132,527); ME3, also known as René 104™ (described in US 6,521,175); LSHR (described in US 6,974,508); Alloy 10 (described in US 6,468,368); Maurer et al (described in US 4,629,521) and Allvac 718 Plus™ (described in US 6,730,264).

Nickel based alloys for use in gas turbine engine components such as high pressure rotor discs have a number of requirements. They must be resistant to environmental degradation such as hot corrosion and oxidation, have a high yield strength at high temperatures, be resistant to creep strain accumulation and dwell fatigue, have a low density, and a good surface stability. In the art, the “stability” of an alloy is normally understood to refer to the alloy’s propensity to precipitate detrimental phases (i.e. an alloy having a high stability will have a low propensity to precipitate detrimental phases). An example of a detrimental phase is the sigma (σ) phase, which can occur when the alloy is subjected to high temperatures for extended time periods (known as “dwell”). One aim of the invention is therefore to minimise the volume fraction of the σ phase after a given time at a given anticipated operating temperature (generally between around 700° C and 800° C).

It is also desirable for the alloy composition to have a low cost, and be suitable for low cost production methods such as forging and powder metallurgy. Alloys having the above properties, and therefore being suitable for use in gas turbine engine components such as turbine blades and rotors discs, are generally known in the art as "superalloys", and are sometimes also referred to as "high performance alloys".

Of these above requirements, the yield strength of the composition at high temperatures (i.e. between around 700 to 800°C) is considered to be most important. The prior nickel based alloys listed in Table 1 have an operational temperature range between 700 and 750°C. Above this temperature, the yield strength of these alloys has been found to be insufficient for some applications, such as for rotor discs in gas turbine engines.

Increasingly, nickel based alloys used for disc rotor applications in modern gas turbine engines for civil aircraft are expected to operate for longer periods of time at temperatures above 700 °C, and in some cases up to 800°C. Rotor discs capable of operating at these temperatures are desirable in order to increase compressor discharge temperatures and rotational speeds, particularly for high pressure compressor and turbine rotors, as both of these factors will lead to increased turbine inlet temperatures, and therefore improved overall thermal and fuel efficiency of the gas turbine engine employing these discs.

Figure 2 shows a cross sectional side view of part of a typical rotor disc 40 having an attached blade 41. The disc 40 comprises a radially outer rim 42, and diaphragm 44 extending from an inner annulus 45 (also known as a bore) of the disc 40 to the rim 42. Both the rim42 and diaphragm 44 of disc rotors 40 can be exposed in use to dwell or sustained load-fatigue cycles at these high temperatures. Under these conditions, stress-assisted oxidation and time dependent deformation can produce intergranular crack growth and therefore high rates of crack growth in discs made of prior alloys. Similar discs 40 are used for both the compressor and turbine sections of the engine.

As a result, resistance to dwell crack growth, and damage tolerance, is a priority for new superalloys for turbine discs. Secondly, many of the prior alloys described in Table 1 have compromised resistance to surface degradation caused by environmental conditions (such as oxidation and type II hot corrosion damage) for improved high temperature strength, resistance to creep strain accumulation and for stable bulk material microstructures (to prevent the precipitation of detrimental topological close packed (TCP) phases). As discs are being exposed to increasingly high temperatures, exceeding 700 ºC, oxidation and hot corrosion damage has become a significant limiting factor for component life. There is now a need to prioritise resistance to hot corrosion and oxidation damage, ahead of other properties when defining alloy chemistries, while maintaining sufficient yield strength at these high temperatures, at an acceptable cost. If prior alloys are used at such high temperatures, environmental protection will need to be applied to disc rotors (e.g. surface coatings), which is technically very difficult and undesirable due to the increased weight and complexity of such discs and the additional manufacturing steps required to form such discs.

The present invention seeks to provide an improved alloy composition, an improved rotor disc, an improved gas turbine engine, and an improved method of forming an article which solves some or all of the above problems.

Summary of the Invention

According to a first aspect of the present invention there is provided a nickel based alloy composition comprising, by atomic per cent, between 12 and 15% of elements from the group consisting of aluminium, titanium, tantalum and niobium, between 0.8 and 1.8% tungsten, between 5 and 8% aluminium, at least 28% of elements from the group consisting of molybdenum, tungsten, chromium and cobalt, wherein the atomic ratio of the sum of titanium, tantalum and niobium to aluminium is between 0.6 and 1.1, the balance being nickel save for incidental impurities.

It has been found that the nickel based alloy composition of the present invention has a high strength at temperatures above around 800°C, and is also relatively lightweight,

resistant to environmental degradation, inexpensive and suitable for conventional forming and machining processes. These properties make the alloy particularly suitable for use in the manufacture of rotor discs for gas turbine engines.

According to a second aspect of the invention, there is provided a rotor disk for a gas turbine engine formed of an alloy in accordance with the first aspect of the invention.

The alloy of the first aspect of the invention has been found to be particularly suitable for forming rotor disks for gas turbine engines, as the alloy has suitable properties for such use. In particular, rotor disks comprising from the alloy have been found to have a yield strength greater than 1000MPa at a temperature of approximately 800°C, while having the required low weight, high corrosion resistance and acceptable cost. The composition has also been found to be amenable to conventional manufacturing and forming methods, without the requirement for additional surface treatments.

According to a third aspect of the invention there is provided a gas turbine engine comprising a rotor disk according to the second aspect of the invention.

Accordingly, the invention provides a gas turbine engine having one or more rotors having a high yield strength at high temperatures. Consequently, the gas turbine engine can operate at a higher thermal efficiency, and hence lower specific fuel consumption, or may have a longer service life between overhauls, resulting in a lower operating cost.

According to a fourth aspect of the invention there is provided a method of forming an article, comprising providing an alloy powder having a composition according to the first aspect of the invention, and consolidating the powder under isostatic conditions.

The alloy of the present invention has been found to be suitable to relatively low cost manufacturing techniques, such as isostatic pressing. Isostatic pressing can be used to form near net shape components, resulting in low processing time and waste, and hence a low “buy to fly” ratio. Consequently, the method provides a relatively inexpensive method for producing gas turbine rotor discs.

Further features of the invention are described in the attached claims.

Brief Description of the Drawings

Embodiments of the invention are described and shown in the following drawings, in which:

Table 1 describes prior nickel based alloys and their elemental compositions;

Table 2 describes the ranges of elemental compositions in terms of atomic per cent and weight per cent of a nickel based alloy in accordance with the present invention;

Table 3 describes property restraints and associated compositional restraints required on alloy chemistry, where RR1000, described in Table 1 is the benchmark condition;

Table 4 describes example compositions T1 to T5 in accordance with the present invention;

Table 5 describes preferred example compositions D1 to D6 in accordance with the present invention;

Figure 1 shows a cross sectional view of a gas turbine engine;

Figure 2 shows a cross sectional view of part of a rotor disc of the engine of Figure 1;

Figure 3 shows the compositional-property relationship for γ' solvus temperature;

Figure 4 shows the compositional-property relationship for specific yield strength - contours represent the specific yield strength normalised to calculated specific yield strength for RR1000;

Figure 5 is a scatter graph showing the correlation between Cr content (in atomic percent) and oxidation resistance for a number of chromia forming alloys, including the alloys described in Table 4 which were used to determine optimal alloy chemistry for oxidation resistance for the present invention;

Figure 6 shows the correlation between Md_{γ} and volume fraction of γ' for the alloy design space, where (a) Cr ≥ 12 at%, (b) Cr > 16 at% - grey data points denote alloys which are free from σ phase and black data points represent alloys which contain the σ phase;

Figure 7 is a scatter graph showing correlation between Cr/Ti ratio (in atomic percent) and the oxidation resistance for a number of chromia forming alloys, including the alloys described in Table 5 which were used to determine optimal alloy chemistry for oxidation resistance for the present invention;

Figure 8 is a graph showing the yield strength at various temperatures for alloys T1 –T3 which are described in Table 4.

Detailed description of the Invention

Figure 1 shows a gas turbine engine 10. The engine 10 comprises, in axial flow series, an air intake duct 11, an intake fan 12, a bypass duct 13, an intermediate pressure compressor 14, a high pressure compressor 16, a combustor 18, a high pressure turbine 20, an intermediate pressure turbine 22, a low pressure turbine 24 and an exhaust nozzle 25. The fan 12, compressors 14, 16 and turbines 20, 22, 24 all rotate about the major axis of the gas turbine engine 10 and so define the axial direction of gas turbine engine.

Air is drawn through the air intake duct 11 by the intake fan 12 where it is accelerated. A significant portion of the airflow is discharged through the bypass duct 13 generating a corresponding portion of the engine 10 thrust. The remainder is drawn through the intermediate pressure compressor 14 into what is termed the core of the engine 10

where the air is compressed. A further stage of compression takes place in the high pressure compressor 16 before the air is mixed with fuel and burned in the combustor 18. The resulting hot working fluid is discharged through the high pressure turbine 20, the intermediate pressure turbine 22 and the low pressure turbine 24 in series where work is extracted from the working fluid. The work extracted drives the intake fan 12, the intermediate pressure compressor 14 and the high pressure compressor 16 via shafts 26, 28, 30. The working fluid, which has reduced in pressure and temperature, is then expelled through the exhaust nozzle 25 and generates the remaining portion of the engine 10 thrust.

Figure 2 shows a rotor disc 40 for one of the compressors 14, 16 or turbines 20, 22, 24 of the gas turbine engine 10. The disc 40 comprises a radially outer rim 42, and a diaphragm 44 extending from a bore 45 of the disc 40 to the rim 42. A blade in the form of a compressor blade 41 is attached to the outer rim 42 of the disc, and is generally formed of a different material to the disc 40. The disc 40 comprises a nickel based superalloy composition in accordance with the present invention, and is formed by a powder metallurgy process followed by a forging process. Though a compressor blade 41 is attached to the disc shown in the Fig. 2, the disc 40 may also be suitable for attachment of a turbine blade.

Table 2 describes a compositional range for a nickel based alloy in accordance with the invention. In conjunction with the specific ranges selected for each alloying element, particular combinations/ratios of alloying elements necessary to produce a high performance disc rotor alloy have been identified. The required performance parameters, and the resultant ratios for the newly developed disc rotor alloy are summarised in Table 3.

The nickel based superalloy composition comprises nickel, which forms a continuous matrix comprising a face centered cubic (FCC) nickel based austenitic phase containing solid solution elements. The nickel based continuous matrix is known within the art as the “gamma (γ)” phase. Some of these alloying elements form a primary strengthening phase known as a “gamma prime (γ’)” phase in an amount such that the volume

fraction of the γ' is between 50% and 60%. The γ' phase has the general formula Ni_3x, where x comprises elements selected from titanium (Ti), aluminium (Al), tantalum (Ta) and niobium (Nb), and usually comprises an ordered intermetallic L_{12} crystal structure. Formation of the γ' phase occurs in the solid state as the supersaturated solid solution of γ-nickel is cooled below its solvus temperature.

The γ' solvus temperature limits the maximum allowable concentration of Al in the alloy. Excessively high γ' solvus temperatures complicate the processing of Ni-based alloys for rotor disc applications, increasing the likelihood of quench cracking during the cooling phase of heat treatments conducted above the γ' solvus temperature. It has been reported that alloys with a γ' solvus temperature below 1180°C are less susceptible to quench cracking. Modelling work – using phase equilibrium calculations - shows a strong correlation between the maximum Al concentration in the alloy and increasing γ' solvus temperature, Figure 3. The (Ti+Ta+Nb)/Al ratio also had the effect of increasing the γ' solvus temperature, however, this effect was much less pronounced. It was determined that the Al level should be restricted to at most 8 at% to maintain a γ' solvus temperature below 1,200°C and preferably below 1,180°C in the newly developed alloy.

Based on hardening theory the specific yield strength was determined using the following equation:

$$\sigma_{ys} = \frac{\bar{M}}{2}\frac{\gamma_{APB} f^{1/2}}{\rho}$$

where σ_{ys} is the specific yield strength and $\bar{M}$ is the taylor factor, f is the volume fraction of γ', γ_{APB} is the anti-phase boundary (APB) energy and ρ *is* the density. The APB energy (in mJ/m^2) was calculated using the following equation,

$$\gamma_{APB} = 195 - 1.7x_{Cr} - 1.7x_{Mo} + 4.6x_W + 27.1x_{Ta} + 21.4x_{Nb} + 15x_{Ti}$$

where, x_{Cr}, x_{Mo}, x_W, x_{Ta}, x_{Nb} and x_{Ti} is the atomic percentage of chromium (Cr), molybdenum (Mo), tungsten (W), Ta, Nb and Ti in the γ' phase. Calculation of the

specific yield strength produces a composition-property relationship outlined in Figure 4.

Although the use of Ta and Nb was seen to be advantageous when designing an alloy with increased specific yield strength, the maximum allowable concentration for each of these alloying elements was limited by cost (particularly in the case of Ta) and microstructural stability (for Nb). It was determined from phase equilibrium calculations that Nb additions must remain below 2 at% to avoid precipitation of the δ phase. Additions of Ta were found to significantly influence the raw material cost for the alloy. Consequently, it was concluded that the Ta level must be limited to 1.2 at% to limit the increase in material cost to within 15% of the current state of the art (RR1000).

Experiments on alloys T1-T3 listed in Table 4 show that a minimum of 50% γ' volume fraction is necessary for adequate yield strength at 800°C – this strength increase was attributed to the higher volume fraction of γ' in the alloy at 800°C. It was also observed that W played an important role in increasing the yield strength, with modifications from 0.3 at% to 1.6 at% increasing the yield strength by approximately 70 MPa. From these experiments a number of conclusions essential to selecting the final alloy composition could be made:

1. (Ti+Ta+Nb)/Al should be greater than 0.6, preferably greater than 0.78, in order produce a γ' phase with APB energy sufficiently high enough to increase tensile strength;
2. Volume fraction of γ' must be greater than 50% in order to produce alloys with an operational temperature up to 800°C; and
3. W levels should be greater than or equal to 0.8 at% for suitable tensile strength at 800°C.

In conjunction with increasing the specific yield strength of the newly designed alloy there was the requirement to improve creep and corrosion resistance, particularly as these damage mechanisms are accelerated by increased temperature. The effect additions of Cr, Co, Mo and W - which partition to the γ phase – have on creep and corrosion resistance was considered as part of the design process. Microstructural stability restricted the maximum concentration of these alloying elements. The

microstructural stability of the alloy, defined by the propensity to form deleterious topologically close packed (TCP) phases such as σ, was considered using 2 methods, phase equilibrium calculations (5 phase equilibrium considered (γ/γ'/σ/δ/η)) and calculation of the metal-d levels for the γ phase, Md_{γ}. For the composition range defined in Table 2 good correlation between both these methods was observed, see Figure 5a - 5b. By examining the results from both these calculations it was concluded that the maximum allowable value for Md_{γ} was approximately 0.88, where Md_{γ} can be calculated in accordance with the following equation:

$$\mathrm{Md}_{\gamma} = \sum_{i=1}^{n} x_i \, (Md)_i$$

Where x_i is the atomic fraction of element *i* in the γ matrix, Md_i is the parameter representing an average energy level of d orbitals of the alloying element *i*, and *n* is the number of elements in the γ matrix.

Additions of Cr, Co, Mo and W increase the value of Md_{γ}. Additions of these elements improves both creep and corrosion resistance whilst reducing microstructural stability in the alloy. The alloys, T1-T6 described in Table 4 - with Md_{γ} values ranging between 0.91 – 0.93 – validated these modelling predictions, as microstructural instability was observed experimentally.

An evident trade-off between the minimum requirements for corrosion resistance, creep resistance, and specific yield strength was apparent. The alloy of the present invention however delivers all the material property requirements desired. The alloys described within this disclosure resists corrosion – considered to be predominantly from oxidation damage - by forming a continuous layer of protective chromia (Cr_2O_3) scale at the interface between the material and the surrounding environment. To examine the effect of alloy chemistry on oxidation resistance a series of oxidation experiments were conducted on a number of chromia forming Ni-based superalloys. The results showed that the minimum Cr content required to produce a protective scale was 12 at%, Figure 5. Creep resistance was considered using the creep merit index. The creep merit index,

M_{creep}, is calculated as a function of the atomic fraction of each alloying element x_i and the inter-diffusion coefficient of that alloy D_i:

$$M_{creep} = \sum_i \frac{x_i}{D_i}$$

The inter-diffusional coefficient D_i is calculated by ($D_{i=}D_{0i}.exp\{-Q/RT\}$) where, D_{0i} is a pre-exponential term, Q_i is the activation energy for diffusion, R is the universal gas constant and T is the absolute temperature.

It was calculated that the sum of the forming elements Cr, Co, Mo and W must be at least 28 at% in order to achieve adequate creep resistance.

The combination of minimum requirements for specific yield strength, corrosion resistance and creep resistance resulted in the discovery of an optimal range for γ' volume fraction.

The criterion necessary to deliver optimal alloy performance are given in Table 3. From these requirements it was determined that the volume fraction of γ' must be greater than or equal to 50% and less than 60%. From phase equilibrium calculations it was determined that the sum of Al+Ti+Ta+Nb must be at least equal to 12 at% and no greater than 15 at% in order to produce the desired volume fraction of γ'. Furthermore, with the Al content fixed between 5 and 8 at%, it is necessary that the ratio of (Ti+Ta+Nb)/Al must be greater than 0.6 but must not exceed 1.1. Given these requirements, it is necessary that the sum of Ti+Ta+Nb must be greater than 5 at% and less than equal to 7.5 at%. Therefore, the minimum allowable concentration of Ti must be equal to 2 at% and the maximum allowable Ti concentration must be equal to 6 at%.

It has been determined by the inventors that the newly developed alloy should be substantially free from additions of Mo. Currently there are no Mo free rotor disc alloys commercially produced. The present invention therefore represents a significantly innovative step. Excluding or greatly reducing Mo content enabled the creep resistance

(measured in terms of the creep merit index) and corrosion resistance (in terms of the Cr content) to be maximised for a microstructurally stable alloy (i.e Md_{γ} was less than or equal to 0.88). Typically, Mo and W are added for creep resistance (see the prior alloys listed in Table 1). These elements have a similar value for *Md*. However, W has a much stronger effect on creep resistance; therefore lower concentrations of W are needed to obtain adequate creep resistance. Using W in preference to Mo allows for increased levels of Cr in a high strength, creep resistant nickel based alloy that is microstructurally stable.

To meet the minimum requirement for creep resistance, it has been determined that the sum of Cr, Co, Mo and W must be greater than 28 at%. However, for optimal creep strength it was calculated that the sum of Cr, Co Mo and W must be between 33 and 35 at%. The upper limit for Cr, Co, Mo and W was determined to be 35 at% to produce a microstructurally stable alloy that met the minimum specific yield strength and oxidation resistance requirements. To enable optimal creep resistance it was determined that the Co levels must be between 15 and 18 at%. Experimental work on alloys T1, T2 and T3, defined in Table 4, identified that additions of W had a strong influence on creep resistance, increases from 0.31at% to 1.56 at% improved creep resistance by 1LMP (Larson Miller Parameter). For this reason a minimum W content of 0.8 at% was selected, the W content was limited to 1.8 at% due to the significant increases to density produced by higher W content.

In order to achieve exceptional oxidation resistance, experimental results showed high concentrations of Cr were required. Given that the minimum requirement for specific strength dictates that at least 50% volume fraction of γ' is required, it has been found that the maximum allowable Cr concentration for a microstructurally stable alloy is 16 at%, as demonstrated by Figure 6a.

The experimental alloys T1-T6 described in Table 4 allowed for a systematic study of compositional-property relationships for oxidation resistance. The results for these alloys – combined with the other industrial alloys studied - provided experimental evidence of a strong correlation between oxidation resistance and the Cr/Ti ratio in

atomic percent in the alloy, as demonstrated by Figure 7. The effect of Cr/Ti ratio on oxidation resistance is particularly evident in alloys T4, T5 and T6. In these alloys, in which only the Ti level was modified for a fixed Cr level, it was found that Nb could be substituted for Ti additions on a 1:1 ratio with no loss in performance whilst improving oxidation resistance. It was concluded on the basis of these experiments that an alloy with a Cr/Ti ratio greater than 4 was preferred, allowing for oxidation resistance better than the current state of the art.

The alloys described herein are suitable for powder metallurgy processing. Consequently, carbon is added to the alloy compositions to pin grain boundaries for grain growth control and to inhibit grain boundary sliding during high temperature deformation during powder metallurgy processing, and particularly during heat treatment. The main grain boundary strength in the described alloys is provided by boron and zirconium through formation of oxides and borides. The preferred ranges for carbon, boron and zirconium are listed in Table 2.

The limiting factor when aiming to maximise the (Ti+Ta+Nb)/Al is microstructural stability. Phase equilibrium calculations show a correlation between increasing (Ti+Ta+Nb)/Al and the propensity to form deleterious phases such as η (Ni_3Ti) or δ (Ni_3Nb) – the upper limit for the (Ti+Ta+Nb)/Al ratio was found to be 1.1. If the upper limit for the (Ti+Ta+Nb)/Al ratio is applied, the concentration of Al in the alloy must be greater than or equal to 6 at% to achieve a yield strength of at least 1000MPa at 800^0C.

The alloy may also comprise small amounts of hafnium in amounts up to 0.5 at%, (corresponding to up to 1.5 wt%). Preferably, the composition contains less than 0.32 at% hafnium (corresponding to up to 1 wt%). Hafnium in these quantities has been found to improve dwell crack growth resistance, thereby increasing component life of a component made of the alloy.

The described alloy compositions can be produced using powder metallurgy methods. Powder metallurgy methods are particularly suitable for the production of the composition where the alloy is to be used for the formation of gas turbine rotor discs.

In a preferred process, small powder particles (< 53 µm in size) produced by, for example, inert gas atomisation, are consolidated in a stainless steel container using hot isostatic pressing to form a sintered article. The sintered article is then extruded to produce a fine grain size billet. Increments are then cut from these billets and forged, preferably, at low strain rates under isothermal conditions. The forging temperature and strain rates are chosen to achieve a required average grain size. In a preferred embodiment, the required average grain size for forming gas turbine rotor discs is ASTM 7 to 6 (32-45 µm). In some cases, the grain size may be as large as ASTM 1 (180 µm).

Other billet and forging technology could alternatively be used to produce raw material for disc rotors. The applicability of alternative techniques, such as cast and wrought processing, i.e. conversion of triple melted ingot, and conventional press forging would depend on the level of success in achieving (i) a consistently homogeneous ingot chemistry with acceptable amounts of melt anomalies, (ii) a sufficiently large forging window and crack-free forgings, and (iii) control of grain growth to produce a narrow grain size distribution in heat treated forgings.

To generate a forging having the required balance of properties, it is necessary to subject the forging to a heat treatment process. This process comprises the following process steps, conducted in the following order:

1. Solution heat treating the forging above the γ' solvus temperature for a sufficient duration to grow the grain size to the required average grain size of ASTM 7 to 6 (32-45 µm) throughout. The required time for a given alloy composition and initial powder size could be determined by trial and error, and determined by microscopy of samples of the resulting heat treated forging. If higher levels of yield stress at all temperatures and low cycle fatigue performance below 650°C are required in the bore and diaphragm regions 44 of the disc rotor 40, then a dual microstructure solution heat treatment can be applied to forgings to produce a fine (5-10 µm) average grain size in these regions.

2. Quenching the forging from the solution heat treatment temperature to room temperature using forced/fan air cooling, polymer or oil quenching.

3. Undertaking stabilisation / stress relief and precipitation heat treatments of the forging at a temperature of between 830 °C and 870 ºC for 4-16 hours, followed by air cooling. This heat treatment is required to (a) relieve residual stresses from quenching and (b) grow tertiary γ' particles.

It is thought that the high temperature stabilisation / stress relief heat treatment will promote reduced rates of crack growth from dwell cycles by precipitating limited amounts of $M_{23}C_6$ carbides at grain boundaries and by increasing the range of tertiary γ' particles, which will reduce the local creep strain resistance at the crack tip. The heat treatment will also dissolve some tertiary γ'. This will precipitate into smaller tertiary γ' particles during the lower temperature precipitation heat treatment, particularly in intra-granular locations, which will improve the resistance to primary creep and creep damage such as slip and grain boundary sliding.

Once the heat treatment process has been conducted, the disc rotor 40 can be formed from the heat treated billet / forging. Due in particular to the relatively low γ' solvus temperature of the forged alloy, the disc rotor 40 can be formed using conventional forging / machining methods.

The following examples are illustrative of several aspects of the disclosure:

Example Alloy D1

Alloy D1 represents a baseline composition for the alloy described within this disclosure. The alloy consists essentially of, in weight percent, 13.3 to 13.9% chromium, 16.2 to 16.8% cobalt, 2.9 to 3.5% tungsten, 3.1 to 3.5% aluminium, 2.9 to 3.3% titanium, 1.4 to 1.8% tantalum, 1.9 to 2.3% niobium, 0.01 to 0.05% carbon, 0.01

to 0.04% boron, 0.05 to 0.07% zirconium, with the balance being nickel and incidental impurities.

Alloy D1 has been designed with an equal weighting considered for all material properties. The sum of γ' forming elements (Al+Ti+Ta+Nb) equal to 12.5 at% producing an alloy with 54% volume fraction of γ', the ratio of (Ti+Ta+Nb)/Al is 0.79. The alloy has at least a 14% improvement in specific yield strength when compared to RR1000 in a coarse grained microstructure at all temperatures. The sum of Co+Cr+Mo+W is equal to 32 at% for creep resistance. The Cr level is 15 at% with the ratio of Cr/Ti in atomic percent fixed at 4 to attain an adequate level of oxidation resistance.

Alongside alloy D1, further alloys were developed. For these further alloys, a bias toward specific properties was considered. The alloys described in the following section will be described in comparison to alloy D1.

Example Alloy D2

Alloy D2 has been designed with a bias toward low density and increased oxidation resistance. The alloy consists essentially of, in weight percent, 14.4 to 15% chromium, 14.3 to 14.9% cobalt, 2.3 to 2.9% tungsten, 3.6 to 4.0% aluminium, 3.2 to 3.6% titanium, 1.4 to 1.8% tantalum, 1.4 to 1.8% niobium, 0.01 to 0.05% carbon, 0.01 to 0.04% boron, 0.05 to 0.07% zirconium, with the balance being nickel and incidental impurities.

The improved oxidation resistance was achieved by increasing the Cr level and Cr/Ti ratio in the alloy. This oxidation resistance was improved at the expense of creep resistance with levels of Co and W being reduced to maintain microstructural stability. Lower density alloys are desirable for aerospace applications; density was reduced by decreasing the W content and increasing the Al content. The reduction in APB energy due to a lower (Ti+Ta+Nb)/Al ratio to 0.69 was offset by an increase in Al+Ti+Nb+Ta equal to 13.5 at%, increasing the γ' volume fraction to 56% to maintain a desirable specific yield strength.

Example Alloy D3

Alloy D3 has been designed with a bias towards creep resistance. The alloy consists essentially of, in weight percent, 10.4 to 11.0% chromium, 16.9 to 17.5% cobalt, 4.3 to 5.0% tungsten, 3.5 to 3.9% aluminium, 3.1 to 3.5% titanium, 2.9 to 3.3% tantalum, 1.4 to 1.8% niobium, 0.01 to 0.05% carbon, 0.01 to 0.04% boron, 0.05 to 0.07% zirconium, the balance being nickel and incidental impurities.

The improvements in creep resistance have been achieved by increasing the level of W and Co in the alloy. The increase in creep resistance has been achieved at the expense of oxidation resistance and density. The Cr content and the Cr/Ti ratio have been reduced, Cr was reduced in order to maintain alloy stability. Higher levels of γ' have also been utilised in order to improve creep strength, the γ' level has been increased by using additions of Al in order to offset the increases in density attained from high levels of W. This alloy has improved mechanical properties at the expense of environmental resistance.

Example Alloy D4

Alloy D4 has been designed for superior strength combined with increased oxidation resistance, achieved at the expense of reduced creep resistance and increased density. The alloy consists essentially of, in weight percent, 14.1 to 14.5% chromium, 15.9 to 16.5% cobalt, 2.2 to 2.8% tungsten, 2.6 to 3.0% aluminium, 2.3 to 2.7% titanium, 2.9 to 3.3% tantalum, 3.0 to 3.4% niobium, 0.01 to 0.05% carbon, 0.01 to 0.04% boron, 0.05 to 0.07% zirconium, the balance being nickel and incidental impurities.

Increased Nb levels have been used to provide mechanical strength. This alloy has a high Cr content and Cr/Ti level for exceptional environmental resistance. Reducing the W content was necessary in order to control alloy density and stability. The γ' volume fraction has been reduced, Al+Ti+Nb+Ta equal to 12 at%, and the (Ti+Ta+Nb)/Al ratio

has been increase to 1. This produces a high strength alloy with a low γ' volume fraction of 48%, allowing for high Cr levels maximising oxidation resistance.

Example Alloy D5

Alloy D5 has been designed for low cost and reduced density; this is at the expense of oxidation resistance. The consists essentially of, in weight percent, 14.3 to 14.9% chromium, 14.2 to 14.8% cobalt, 2.9 to 3.5% tungsten, 2.6 to 3.0% aluminium, 4.4 to 4.8% titanium, 1.4 to 1.8% tantalum, 0.6 to 1.0% niobium, 0.01 to 0.05% carbon, 0.01 to 0.04% boron, 0.05 to 0.07% zirconium, and wherein the balance comprises nickel and incidental impurities.

By substituting Nb with additions of Ti it was possible to reduce the density of the alloy. The Cr level has been increased to try and maintain a suitably high Cr/Ti ratio. The sum of Al+Ti+Ta+Nb was set at 12.4 at% to produce a γ' volume fraction of 52%. The APB energy was increased by producing an alloy where the (Ti+Ta+Nb)/Al ratio is 1.06 meaning that a high specific strength is attained. The use of low Ta concentrations combined with the low Nb levels creates a low cost alloy.

Example Alloy D6

Alloy D6 has been designed for superior creep resistance. The consists essentially of, in weight percent, 12.1 to 12.7% chromium, 13.8 to 14.4% cobalt, 4.1 to 4.7% tungsten, 2.5 to 2.9% aluminium, 4.4 to 4.8% titanium, 3.5 to 3.9% tantalum, 1.2 to 1.4% niobium, 0.01 to 0.05% carbon, 0.01 to 0.04% boron, 0.05 to 0.07% zirconium, and wherein the balance comprises nickel and incidental impurities.

High levels of Ta have been used in substitution for Ti additions. This results a high strength alloy with a high Cr/Ti ratio, allowing for superior oxidation resistance in a relatively low Cr alloy. Small levels of Mo have been utilised to maximise creep resistance whilst maintaining a microstructurally stable alloy.

The alloy composition and forging / heat treatment methods described above provide an alloy composition suitable for forming rotor discs of gas turbine engines having a number of advantages of prior alloy compositions.

The described alloys compositions, once heat treated, show a balance of material properties that will enable them to be used to form gas turbine rotor discs capable of operation at temperatures up to 800ºC for prolonged periods. Whilst improvements in strength and resistance to creep strain accumulation are expected from these alloys, the major benefit is considered to be in the resistance to hot corrosion and oxidation damage and dwell crack growth, as well as dwell fatigue endurance.

Figure 8 shows the yield strength for example alloys T1, T2 and T3 at various temperatures. As can be seen, each of the alloys maintains yield strengths greater than 825 MPa at temperatures up to 800°C, with alloy T3 having a yield strength greater than 900 MPa at 800°C. This demonstrates how increased volume fractions of γ‘, can increase the yield strength at high temperatures in comparison to the prior art. The alloys T1-T3 had (Ti+Ta+Nb)/Al ratios of 0.55 producing alloys with low APB energy. The increase in APB energy - attained by having a (Ti+Ta+Nb)/Al ratio of at least 0.6 – enables a yield strength of 1000MPa at temperatures of 800^0C when the volume fraction of γ’ is greater than 50%.

Figure 5 shows experimental results after 100 hours of cyclic oxidation testing at 800°C (5 cycles in total) showing the effect of Cr content (at%) on the oxidation resistance of a number of chromia forming disc alloys. As can be seen, example alloys T1 to T6 have a high oxidation resistance. The Cr and Ti levels have been optimised for alloys D1-D5 to ensure that these levels of oxidation resistance are achieved.

Unlike the prior art, it is proposed that the disclosed alloys achieve a balance between resistance to environmental degradation and high temperature properties such as proof strength, resistance to creep strain accumulation, dwell fatigue and damage tolerance. Use of components made from the prior art alloys is limited to temperatures between

700-750 ºC, whereas the disclosed alloys can be used to increase the operating temperatures of the rotor discs of a gas turbine engine up to 800ºC.

Although the description refers to the described alloys as being particularly useful for forming rotor discs for gas turbine, the alloys could also be used to form other components. For example, the alloys could be used for hot static parts of a gas turbine engine, such as combustor and turbine casings. These applications would benefit from all of the envisaged improvements in material properties, notably the improved high temperature proof strength and resistance to creep strain accumulation. As compressor discharge temperatures and turbine entry temperatures are progressively raised to produce improvements in thermal efficiency and thus fuel consumption, the temperature of static parts in the combustor and turbine also increase during operation.

Such casings could be produced using conventional cast and wrought technology, i.e. from forgings, or via powder metallurgy, though the consolidation of inert gas atomised powder using hot isostatic pressure. The latter route is preferred given the highly alloyed compositions and ability to produce compacts that are close to the component geometry, which reduces the amount of material required and the time required to machine the component.

Although the alloy is described as being formed by powder metallurgy and subjected by heat treatment, other material processing methods could be used to generate articles from the alloy compositions having the required properties.

CLAIMS

1 A nickel based alloy composition comprising, by atomic per cent, between 12 and 15% of elements from the group consisting of aluminium, titanium, tantalum and niobium, between 0.8 and 1.8% tungsten, between 5 and 8% aluminium, at least 28% of elements from the group consisting of molybdenum, tungsten, chromium and cobalt, wherein the atomic ratio of the sum of titanium, tantalum and niobium to aluminium is between 0.6 and 1.1, the balance being nickel save for incidental impurities.

2 An alloy according to claim 1, wherein the composition comprises, by atomic per cent, less than 1% molybdenum.

3 An alloy composition according to claim 1 or claim 2, wherein the composition further comprises one or more of, in atomic per cent, between 0.05 and 0.3% carbon, between 0.05% and 0.25% boron, between 0.02 and 0.06% zirconium and less than 0.5% hafnium.

4 An alloy composition according to any of the preceding claims consisting essentially of, in atomic percent, between 12 and 17.3% chromium, between 14 and 18.3% cobalt, between 0.8 and 1.8% tungsten, between 5.8 and 8.2% aluminium, between 2.7 and 6.2% titanium, between 0.4 and 1.2% tantalum, between 0.05 and 0.3% carbon, between 0.05% and 0.25% boron, , between 0.02-0.06 zirconium, less than 1.0% molybdenum and less than 0.5% hafnium, the balance being nickel save for incidental impurities.

5 An alloy composition according to any of the preceding claims comprising, in atomic percent, substantially 15% chromium, substantially 16% cobalt, substantially 7% aluminium, substantially 3.7% titanium, substantially 0.5% tantalum, substantially 1% tungsten, substantially 1.3% niobium, substantially

0.08% boron, substantially 0.13% carbon, substantially 0.04% zirconium, the balance being nickel save for incidental impurities.

6 An alloy composition according to any of the preceding claims comprising, in atomic percent, substantially 16% chromium, substantially 14% cobalt, substantially 8% aluminium, substantially 3.7% titanium, substantially 0.5% tantalum, substantially 0.8% tungsten, substantially 1.3% niobium, substantially 0.08% boron, substantially 0.13% carbon, substantially 0.04% zirconium, the balance being nickel save for incidental impurities.

7 An alloy composition according to any of the preceding claims comprising, in atomic percent, substantially 12% chromium, substantially 17% cobalt, substantially 8% aluminium, substantially 4% titanium, substantially 1% tantalum, substantially 1.5% tungsten, substantially 1% niobium, substantially 0.08% boron, substantially 0.13% carbon, substantially 0.04% zirconium, the balance being nickel save for incidental impurities.

8 An alloy composition according to any of the preceding claims comprising, in atomic percent, substantially 16% chromium, substantially 16% cobalt, substantially 6% aluminium, substantially 3% titanium, substantially 1% tantalum, substantially 0.8% tungsten, substantially 2% niobium, substantially 0.08% boron, substantially 0.13% carbon, substantially 0.04% zirconium, the balance being nickel save for incidental impurities.

9 An alloy composition according to any of the preceding claims comprising, in atomic percent, substantially 16% chromium, substantially 14% cobalt, substantially 6% aluminium, substantially 5.5% titanium, substantially 0.5% tantalum, substantially 1% tungsten, substantially 0.5% niobium, substantially 0.08% boron, substantially 0.13% carbon, substantially 0.04% zirconium, the balance being nickel save for incidental impurities.

10 An alloy composition according to any of the preceding claims comprising, in atomic percent, substantially 14% chromium, substantially 14% cobalt, substantially 7.4% aluminium, substantially 3.25% titanium, substantially 1.2% tantalum, substantially 0.85% molybdenum, substantially 1.4% tungsten, substantially 0.9% niobium, substantially 0.135% boron, substantially 0.245% carbon, substantially 0.036% zirconium, the balance being nickel save for incidental impurities.

11 An alloy composition according to any of the preceding claims, wherein the alloy has a yield strength greater than 1000MPa at a temperature of approximately 800°C.

12 An alloy composition according to any of the preceding claims, wherein the alloy has a γ' fraction of between about 50% and about 60%.

13 An alloy composition according to any of the preceding claims having a γ' solvus temperature below 1200°C.

14 An alloy composition according to any of the preceding claims having an Md_γ value less than 0.88, where

$$\mathrm{Md}_\gamma = \sum_{i=1}^{n} x_i \, (Md)_i$$

and where x_i is the atomic fraction of element *i* in the gamma matrix; Md_i is the parameter representing an average energy level of d orbitals of the alloying element *i*; and *n* is the number of elements in the gamma matrix.

15 A rotor disk for a gas turbine engine formed of an alloy according to any of the preceding claims.

16 A gas turbine engine comprising the rotor disk of claim 15.

17 A method of forming an article, comprising providing an alloy powder having a composition according to any of claims 1 to 15, and consolidating the powder under isostatic conditions.

18 A method according to claim 17, wherein the powder comprises particles having a diameter less than 53µm.

19 A method according to claim 17 or claim 18, wherein the powder particles are formed by inert gas atomisation.

20 A method according to any of claims 17 to 19, wherein the consolidated powder is extruded to form a billet.

21 A method according to claim 20, wherein the billet is forged to form a component.

22 A method according to claim 21, wherein the billet is forged such that the average grain size of the component is between 5 and 10 µm.

23 A method according to claim 22 or claim 23, wherein the component is solution heat treated above the γ' solvus temperature of the alloy such that the average grain size of the component is between 32 and 45 µm.

24 A method according to any of the preceding claims, wherein the grain size of the billet or component is less than or equal to ASTM 1 (180 µm).

	Element Concentration Weight Percent (wt%)														
Alloy	**Cr**	**Co**	**Fe**	**Mo**	**Al**	**Ti**	**Ta**	**W**	**Nb**	**Hf**	**Zr**	**B**	**C**	**Ni**
Inconel 718	19.00	0.50	18.00	2.90	0.45	1.00	0.00	0.00	5.40	0.00	0.05	0.000	0.030	Bal
Udimet 720Li	16.00	15.00	0.00	3.00	2.50	5.00	0.00	1.25	0.00	0.00	0.035	0.020	0.020	Bal
RR1000	15.00	18.50	0.00	5.00	3.00	3.60	2.00	0.00	0.00	0.50	0.06	0.030	0.030	Bal
ME3	13.00	20.50	0.00	3.70	3.40	3.60	2.40	2.00	0.90	0.00	0.05	0.030	0.040	Bal
LSHR	13.00	21.00	0.00	2.70	3.50	3.50	1.60	4.30	1.50	0.00	0.05	0.030	0.030	Bal
Alloy 10	11.00	18.50	0.00	2.60	3.55	3.75	1.50	4.60	1.00	0.00	0.075	0.030	0.030	Bal
Maurer et al	14-18	3-7	<2	0.3-3.0	3.5-5.5	1-4	<0.05	4-8	<0.05	0	<0.1	<0.1	0.05	Bal
Allvac 718 Plus	19.0	9.0	10.0	2.8	1.5	0.7	0.0	1.0	5.5	0.0	0.000	0.010	0.030	Bal

Table 1

	Element Concentration (wt%)											
	Cr	Co	W	Al	Ti	Ta	Nb	C	B	Zr	Hf	Mo
Upper	14.9	19.4	5.2	4.3	5.5	3.5	3.4	0.05	0.44	0.1	1.5	1.5
Lower	10.7	15	2.7	2.4	2.1	1.5	0	0.01	0.01	0.03	0	0
	Element Concentration (at%)											
Upper	17.3	18.3	1.8	8.2	6.2	1.2	2.1	0.30	0.25	0.06	0.5	1.0
Lower	12	14	0.8	5.8	2.7	0.4	0	0.05	0.05	0.02	0	0

Table 2

Material Property	Target	Compositional Restrictions
Specific Yield Strength	10% increase	Al+Ti+Ta+Nb ≥ 12 at% (Ti+Ta+Nb)/Al ≥ 0.6 (at%)
Creep Merit Index	Equivalent or Better	Cr+Co+Mo+W ≥ 28 at%
Material Costs	No more than 15% increase	Ta ≤ 1.2 at%
γ' solvus Temperature	Less than 1200°C	Al ≤ 8 at%
Free from deleterious phases (e.g. σ, η, δ**)**		Mo < 1 at% Al+Ti+Ta+Nb ≤ 15 at% Cr+Co+Mo+W ≤ 35 at% Md γ ≤ 0.88 (Ti+Ta+Nb)/Al ≤ 1.1 Nb ≤ 2at%
Oxidation Resistant	Equivalent or Better	Cr ≥ 12 at% Cr/Ti (at%) ≥ 3

Table 3

	Element Concentration (wt%)										
Alloy	Cr	Co	W	Al	Ti	Ta	Nb	C	B	Zr	
T1	20.25	19.00	1.00	3.94	3.45	2.00	0.00	0.027	0.015	0.060	
T2	17.25	19.00	3.00	3.81	3.45	2.00	0.00	0.027	0.015	0.060	
T3	15.25	19.00	5.00	3.69	3.45	2.00	0.00	0.027	0.015	0.060	
T4	17.19	19.00	3.00	3.80	3.09	2.00	0.67	0.027	0.015	0.060	
T5	17.14	19.00	3.00	3.79	2.74	2.00	1.33	0.027	0.015	0.060	
T6	17.08	19.00	3.00	3.77	2.39	2.00	1.99	0.027	0.015	0.060	
	Element Concentration (at%)										
T1	19.43	18.23	0.31	8.22	4.06	0.62	0.00	0.127	0.078	0.037	
T2	18.69	18.17	0.92	7.96	4.06	0.62	0.00	0.127	0.078	0.037	
T3	16.81	18.48	1.56	7.84	4.13	0.63	0.00	0.129	0.080	0.038	
T4	18.69	18.17	0.92	7.96	3.65	0.62	0.41	0.127	0.078	0.037	
T5	18.69	18.17	0.92	7.97	3.25	0.62	0.81	0.127	0.079	0.037	
T6	18.69	18.17	0.92	7.95	2.84	0.62	1.22	0.128	0.079	0.037	

Table 4

	Element Concentration (wt%)											
	Cr	Co	Al	Ti	Ta	Mo	W	Nb	B	C	Zr
D1	13.6	16.5	3.3	3.1	1.6	0.0	3.2	2.1	0.015	0.027	0.059
D2	14.7	14.6	3.8	3.4	1.6	0.0	2.6	1.6	0.015	0.027	0.060
D3	10.7	17.2	3.7	3.3	3.1	0.0	4.7	1.6	0.015	0.026	0.058
D4	14.3	16.2	2.8	2.5	3.1	0.0	2.5	3.2	0.015	0.026	0.058
D5	14.6	14.5	2.8	4.6	1.6	0.0	3.2	0.8	0.015	0.027	0.059
D6	12.4	14.1	3.4	2.7	3.7	1.4	4.4	1.4	0.025	0.050	0.056
	Element Concentration (at%)										
D1	15	16	7	3.7	0.5	0	1	1.3	0.079	0.127	0.037
D2	16	14	8	3.7	0.5	0	0.8	1.3	0.079	0.127	0.037
D3	12	17	8	4	1	0	1.5	1	0.079	0.127	0.037
D4	16	16	6	3	1	0	0.8	2	0.079	0.127	0.037
D5	16	14	6	5.5	0.5	0	1	0.5	0.079	0.127	0.037
D6	14	14	7.4	3.25	1.2	0.85	1.4	0.9	0.135	0.245	0.036

Table 5

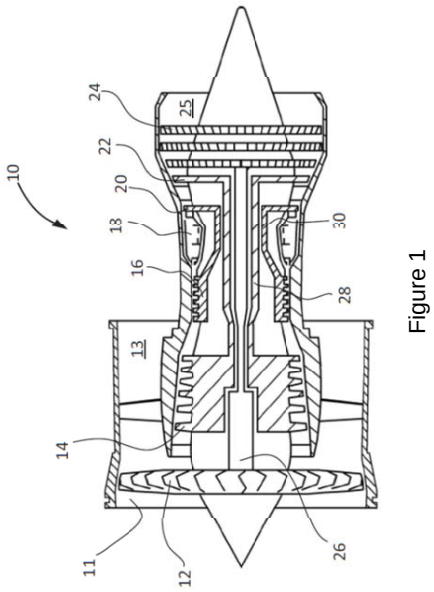


Figure 1

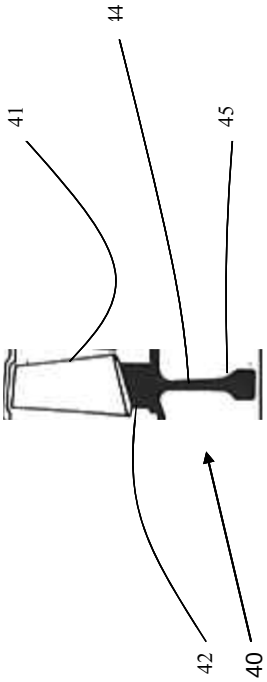


Figure 2

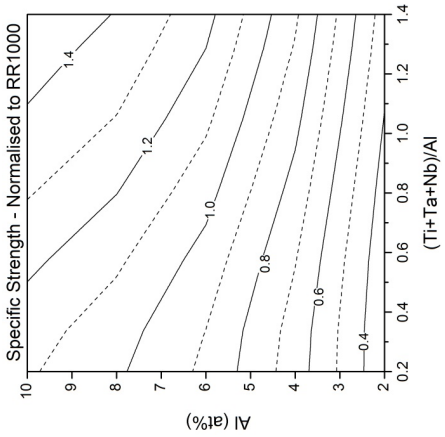


Figure 4

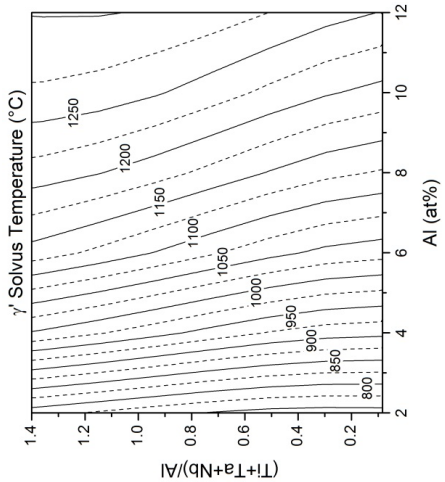


Figure 3

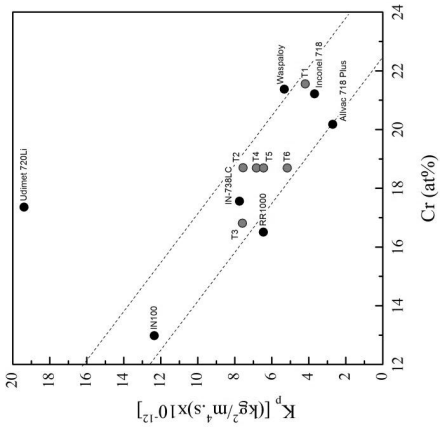
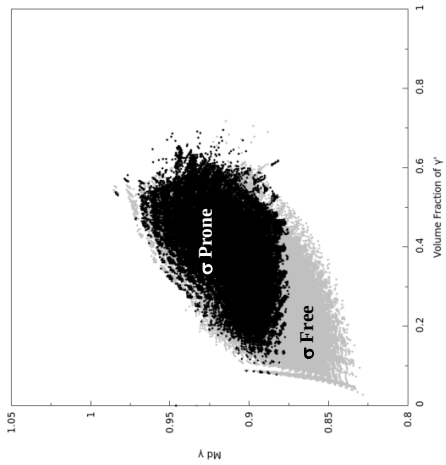
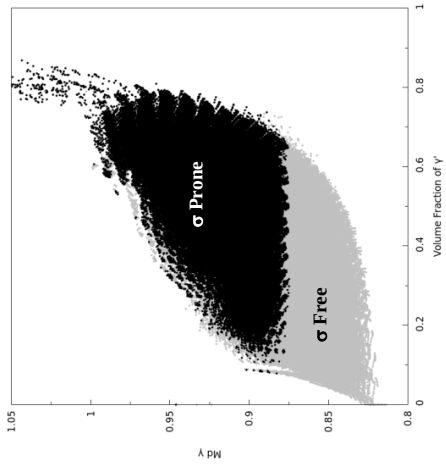

Udimet 720Li
IN100
IN-738LC
T2
T4
T5
T6
T3
RR1000
Waspaloy
T1
Inconel 718
Allvac 718 Plus
Cr (at%)
K_p [(kg²/m⁴.s)x10⁻¹²]

Figure 5


σ Prone
σ Free
Md γ
Volume Fraction of γ'
1.05
1
0.95
0.9
0.85
0.8
0
0.2
0.4
0.6
0.8
1

(b)


σ Prone
σ Free
Md γ
Volume Fraction of γ'
1.05
1
0.95
0.9
0.85
0.8
0
0.2
0.4
0.6
0.8
1

(a)

Figure 6

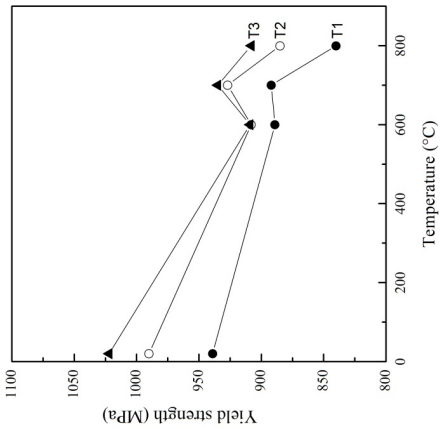


Figure 8

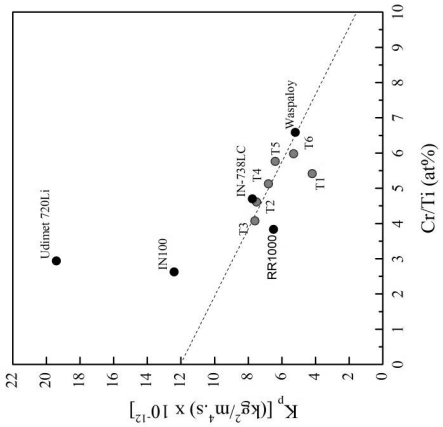


Figure 7